LEVEL-SET RANS METHOD
FOR SLOSHING AND GREEN WATER SIMULATIONS

A Dissertation

by

KAI YU

Submitted to the Office of Graduate Studies of
Texas A&M University
in partial fulfillment of the requirements for the degree of

DOCTOR OF PHILOSOPHY

December 2007

Major Subject: Ocean Engineering

LEVEL-SET RANS METHOD FOR SLOSHING AND GREEN WATER SIMULATIONS

A Dissertation

by

KAI YU

Submitted to the Office of Graduate Studies of
Texas A&M University
in partial fulfillment of the requirements for the degree of

DOCTOR OF PHILOSOPHY

Approved by:

Chair of Committee,	Hamn-Ching Chen
Committee Members,	Moo-Hyun Kim
	Jun Zhang
	Alan B. Palazzolo
Head of Department,	David V. Rosowsky

December 2007

Major Subject: Ocean Engineering

ABSTRACT

Level-Set RANS Method
for Sloshing and Green Water Simulations. (December 2007)
Kai Yu, B.S., University of Science and Technology of China;
M.S., Chinese Academy of Sciences
Chair of Advisory Committee: Dr. Hamn-Ching Chen

An interface-preserving level set method is incorporated into the Reynolds-Averaged Navier-Stokes (RANS) numerical method for the time-domain simulation of green water effects. This generalized method can be used to evaluate two- and three-dimensional, laminar and turbulent, free surface flows in moving non-orthogonal grids.

In the method, free surface flows are modeled as immiscible two-phase (air and water) flows. A level set function is used to mark the individual fluids and the free surface itself is represented by the zero level set function. The level set evolution equation is coupled with the conservation equations for mass and momentum, and solved in the transformed plane. Chimera domain decomposition technique is employed to handle embedding, overlapping, or matching grids.

To demonstrate the feasibility of the method, calculations are performed in several bench mark free surface flows including dam break flows, free jets, solitary wave propagations and the impingement of dam break flow on a fixed structure. The comparisons between the simulations and the experimental data provide a thorough validation of the present method. The results also show the potential capability of level-set RANS method in much more complicated free surface flow simulations.

After validations, the method is applied to simulate sloshing flows in LNG tank and green water over the platform. In sloshing flows, the level-set RANS method captures the large impact pressure accurately on LNG tank walls. It also generates a plunging breaker successfully in front of a platform in the numerical wave tank. The good agreements between numerical and experimental results prove the level set RANS method is a powerful and accurate CFD methodology in free surface flow simulations.

To my parents and sister

ACKNOWLEDGEMENTS

I would like to express my deepest gratitude to my advisor and chair, Dr. Hamn-Ching Chen, for his instruction, patience and continuous support throughout my doctoral study. Without his guidance, I would never have reached this stage. I also highly appreciate his contributions to my intellectual and personal development in the past four years.

I would like to extend my gratefulness to my committee, Dr. Jun Zhang, Dr. Moo-Hyun Kim and Dr. Alan Palazzolo, for their valuable time, suggestions and personal encouragements.

A special thank goes to Dr. Zhang for his contributions to the nonlinear wave generation in the numerical wave tank. He helped me pave a path through bushes during my early stage of research.

I would also like to thank my parents and sister for their boundless love and support.

TABLE OF CONTENTS

Page

ABSTRACT iii

DEDICATION v

ACKNOWLEGEMENTS vi

TABLE OF CONTENTS vii

LIST OF TABLES ix

LIST OF FIGURES x

CHAPTER

I INTRODUCTION 1

1.1. Background 1
1.2. Literature Review 2
  1.2.1. Surface Tracking 3
  1.2.2. Surface Capturing 4
1.3. Method of Present Study 10
1.4. Organization 12

II MATHEMATICAL MODEL 14

2.1. Introduction 14
2.2. Level Set Equation 14
2.3. RANS Equations 16

III NUMERICAL MODEL 20

3.1. Introduction 20
3.2. Level Set Equation 20
3.3. RANS Equations 24
3.4. General Solution Procedure 25

IV TEST CASES AND VALIDATIONS 27

4.1. Re-distancing Procedure 27
4.2. Zalesak's Problem 29
4.3. Fluid Element Stretching 30
4.4. Fluid Element Stretching and Restoration 32

CHAPTER Page

4.5. Propagation of a Solitary Wave ... 33
4.6. Dam Breaking ... 36
4.7. Dam Breaking with an Obstacle ... 44
4.8. Free Jet Simulation ... 46

V SLOSHING SIMULATIONS ... 50

5.1. Introduction ... 50
5.2. Geometry and Motions ... 52
5.3. Time Step Size and Grid Refinement ... 56
5.4. Scale Effects ... 58
5.5. Results and Discussions ... 59
  5.5.1. Case 1 - Transverse & 16.3% FLVL ... 63
  5.5.2. Case 2 - Transverse & 30% FLVL ... 72
  5.5.3. Case 3 - Transverse & 50% FLVL ... 81
  5.5.4. Case 4 - Longitudinal & 50% FLVL ... 91
  5.5.5. Case 5 - Longitudinal & 80% FLVL ... 98
  5.5.6. Case 6 - Longitudinal & 92.5% FLVL ... 106
5.6. Conclusion ... 115

VI GREEN WATER SIMULATIONS ... 117

6.1. Introduction ... 117
6.2. Wave Runup on 2D Platform ... 118
6.3. Green Water on 2D Platform ... 125
6.4. Green Water on 3D Platform ... 135

VII CONCLUSIONS ... 139

7.1. Sloshing Simulations ... 139
7.2. Green Water over Offshore Structure ... 139

REFERENCES ... 141

VITA ... 149

LIST OF TABLES

TABLE Page

5.1 LNG tank motion periods 55

5.2 LNG tank motion amplitudes 55

LIST OF FIGURES

FIGURE Page

1.1 A typical breaking wave near shore . . . 2

1.2 Chimera grids around vertical cylinders . . . 4

1.3 MAC method . . . 5

1.4 The definition of volume fraction . . . 7

1.5 The interface reconstruction in VOF methods . . . 8

4.1 Grid and initial ϕ in re-distancing procedure . . . 27

4.2 The ϕ evolution in re-distancing procedure . . . 28

4.3 Zalesak's problem . . . 30

4.4 Stretching of a circular fluid element in swirling flow . . . 31

4.5 Mass change in a circular fluid element stretching . . . 32

4.6 The level-set evolution during stretching and shrinking . . . 34

4.7 Mass change in stretching and shrinking . . . 35

4.8 Propagation of solitary wave; $A_0 = 0.4$ . . . 35

4.9 Typical velocity field of a solitary wave . . . 35

4.10 Comparison in solitary wave propagation . . . 36

4.11 Free surface and velocity vectors in dam-breaking . . . 37

4.12 2D dam-breaking problem . . . 38

4.13 Chimera grids for dam-breaking problems . . . 39

4.14 Dam-breaking with two different embedding grids . . . 41

FIGURE Page

4.15 Velocity comparison for three different grids 42

4.16 Free surface profiles for 3D dam breaking 43

4.17 Experiment setup of dam-breaking with an obstacle 43

4.18 Numerical model of dam-breaking with an obstacle 44

4.19 Free surface comparison 45

4.20 Free surface profiles and velocities, 2D free jet 48

4.21 Free surface profiles, 3D free jet 49

5.1 Membrane-type LNG tank geometry 52

5.2 Sensor positions on LNG model tank 53

5.3 2D grids for transverse and longitudinal motions 54

5.4 Influence of time increment, Ch.11 in Case 3 57

5.5 Grid refinement study, Ch.11 in Case 3 57

5.6 Scale effects, Ch.11 in Case 3 58

5.7 Grid and sensor locations for 2D simulations 59

5.8 Grid and sensor locations for 3D simulations 61

5.9 Nine-point stencils around pressure sensor 62

5.10 Tank motion trajectory, Case 1 63

5.11 2D pressure history, Ch.15, Case 1 64

5.12 2D impact pressure, Ch.15 (right sensor), Case 1 64

5.13 3D impact pressure, Ch.15 (S40), Case 1 65

5.14 Impact pressures, the vicinity of Ch.15 (S40), Case 1 66

5.15 2D free surface, $\vec{V}, p$, Case 1 68

FIGURE Page

5.16 3D free surface and pressure contours, Case 1 70
5.17 Tank motion trajectory, Case 2 72
5.18 2D pressure history, Ch.15, Case 2 72
5.19 2D impact pressure, Ch.15 (right sensor), Case 2 73
5.20 3D impact pressure, Ch.15 (S38), Case 2 74
5.21 Impact pressures, the vicinity of Ch.15 (S38), Case 2 74
5.22 2D free surface, $\vec{V}, p$, Case 2 76
5.23 3D free surface and pressure contours, Case 2 78
5.24 Tank motion trajectory, Case 3 81
5.25 2D pressure history, Ch.11, Case 3 82
5.26 2D impact pressure, Ch.11 (right sensor), Case 3 82
5.27 3D impact pressure, Ch.11 (S04), Case 3 83
5.28 Impact pressures, the vicinity of Ch.11 (S04), Case 3 83
5.29 2D free surface, $\vec{V}, p$, Case 3 85
5.30 3D free surface and pressure contours, Case 3 87
5.31 The swirling flow, Case 3 90
5.32 Tank motion trajectory, Case 4 91
5.33 2D pressure history, Ch.3, Case 4 92
5.34 3D impact pressure, Ch.1 (S04), Case 4 92
5.35 Impact pressures, the vicinity of Ch.1 (S04), Case 4 93
5.36 2D free surface, $\vec{V}, p$, Case 4 94
5.37 3D free surface and pressure contours, Case 4 96

FIGURE Page

5.38 Tank motion trajectory, Case 5 99

5.39 2D pressure history, Ch.7, Case 5 99

5.40 3D impact pressure, Ch.7 (S11), Case 5 100

5.41 Impact pressures, the vicinity of Ch.7 (S11), Case 5 100

5.42 2D free surface, $\vec{V}, p$, Case 5 102

5.43 3D free surface and pressure contours, Case 5 104

5.44 Tank motion trajectory, Case 6 106

5.45 2D pressure histories, Ch.3, Case 6 107

5.46 2D impact pressure, Ch.3, Case 6 108

5.47 3D impact pressure, Ch.3 (S12), Case 6 108

5.48 Impact pressures, the vicinity of Ch.3 (S12), Case 6 109

5.49 2D free surface, $\vec{V}, p$, Case 6 110

5.50 3D free surface and pressure contours, Case 6 112

5.51 Pressure and velocity in the ullage space 114

6.1 Chimera grid for wave runup simulation 119

6.2 Wave elevation and pressure contours 121

6.3 Time history of wave elevation 122

6.4 Velocity and vorticity around the platform 123

6.5 Chimera grids around vertical cylinders 124

6.6 Free surface pressure contours around cylinders 126

6.7 The model structure and numerical grids 127

6.8 Snapshots of a plunging breaker 129

FIGURE Page

6.9 Comparison of green water effect on 2D platform 132
6.10 Green water around a platform deck 134
6.11 3D grid for green water simulation 135
6.12 Green water on a 3D platform 137

CHAPTER I

INTRODUCTION

1.1. Background

The objective of this study is to develop a general, accurate and robust computational fluid dynamics (CFD) methodology which is capable of predicting the large deforming free surface flows such as green water over an offshore structure and sloshing flow in a Liquified Natural Gas (LNG) tank.

Engineering applications often involve multi-phase flows. Liquid-gas interfaces occur in a wide variety of natural phenomena and technical processes. In the most common cases, the free surface is an air-water boundary. Free surface flows feature most prominently in the marine environment, and are characterized by air-water interactions and unsteady waves. Figure 1.1 shows the classic curl of a breaking wave as a wave approaches shore. The interaction between the extreme waves and floating structures is a primary concern in the design of offshore structure. Impact pressure due to sloshing flow is also a critical concern for the ship owners, designers and builders of the LNG carriers.

This study mainly focuses on the immiscible fluids flow, typically air-water flows. The numerical simulations of free surface flows are difficult due to moving boundaries. The position of the boundary is known only at the initial time; its location at later times has to be determined as part of the solution. The requirements for a good numerical multi-phase prediction method include generality, high accuracy,

---

This dissertation follows the style and format of *IEEE Transactions on Very Large Scale Integration (VLSI) Systems.*

Figure 1.1. A typical breaking wave near shore

minimal memory usage and CPU time.

Prior work on CFD methodology which are capable of predicting free surface flow can be tracked as far back as the early 1960s. Since then there have been numerous developments in the field, but there are still limitations for each of them. The next section gives an overview of these developments, their advantages and disadvantages. It is then followed by a section which outlines the contribution of this dissertation. The chapter is closed with the structure of the dissertation.

1.2. Literature Review

Green water loads on an offshore platform occurs when an incoming wave significantly exceeds the free board and water runs onto the deck. The main problem in the numerical simulation is the accuracy in tracking the air-water interface. Many methods have been proposed to predict the interface between two different fluids. They could be classified into two different categories: the interface-tracking methods and the interface-capturing methods (Ferziger and Peric, 1999). The interface-tracking methods follow the free surface motions and use boundary-fitted grids which are re-adjusted in each time step whenever the free surface moves. The interface-capturing methods do not define a sharp free surface boundary. Instead, the computation is performed on a fixed grid, which is extended beyond the free surface. The geometry of the free surface is determined by a certain numerical variable, which is one of the numerical solutions. A variety of methods in this interface-capturing approach have been developed over the past several decades. Three typical methods from this category, Marker and Cell (MAC) scheme (Harlow and Welch, 1965), volume of fluid (VOF) scheme (Nichols et al., 1980; Hirt and Nichols, 1981) and level set method (Osher and Sethian, 1988) are summarized in the following section.

1.2.1. Surface Tracking

The surface tracking methods are expressed in Lagrangian view point which describe fluid motions as we follow a fluid particle along its trajectory. The surface tracking methods are characterized by an explicit representation of the surface. The Lagrangian method treats the free surface as a sharp interface whose motion is exactly followed. This is normally done by adapting boundary-fitted grids to the free surface and updating grids at each time step to track the new location of the free surface by using a height function to describe the vertical height of the free surface location.

Chen, Liu, Chang and Huang (2002) used a Chimera Reynolds-Averaged Navier-Stokes method, which is a kind of Lagrangian approach, for time-domain simulation of turbulent flows around a rectangular barge under large amplitude waves. A flexible chimera grid system was developed to handle partial hull submergence with green water on the barge deck. The grid is adjusted every time step to follow the free surface motion. The same method was applied in Chen, Liu and Huang (2001). The surface tracking methods were also found in time-domain simulation of floating pier and multiple-vessel interactions, Chen and Huang (2004).

The surface tracking methods can describe the free surface flow accurately especially when small deformation occurs. Figure 1.2 describes chimera grids in the simulation of wave runup around multiple cylinders. The wake flows behind cylinders were captured accurately. The drawback of the surface tracking methods is the inability to handle complex surface geometries, such as breaking wave, bubbles in water and droplets in air. This makes the surface tracking methods unable to model sloshing flows in LNG tank and green water effects on the offshore structures, in which overturning or breaking waves are expected to happen frequently.

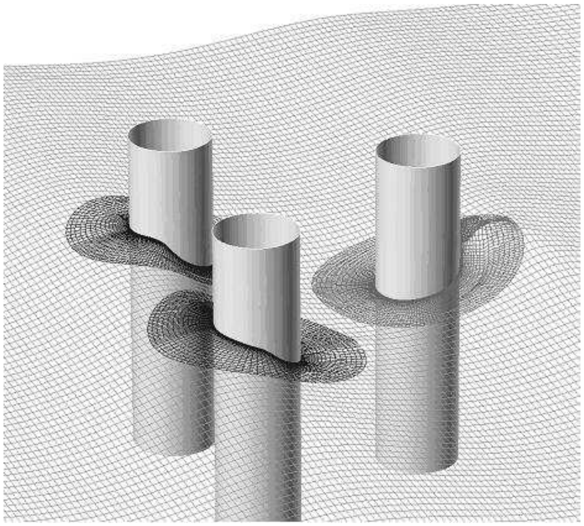

Figure 1.2. Chimera grids around vertical cylinders

1.2.2. Surface Capturing

The surface capturing methods use a different approach so-called Eulerian view point which describes the fluid motion at a fixed point. The computation is performed on a fixed grid, which extends beyond the free surface. In stead of being defined as a sharp boundary, the free surface is determined only after the solutions in the whole domain are finished. A number of schemes are available, and all of them use an implicit representation of the interface which is then captured as part of the solution. The most common schemes for surface capturing are the Marker-And-Cell method (MAC) which is proposed first by Harlow and Welch in 1965, the Volume-Of-Fluid method (VOF) which is originally developed by Hirt and Nichols in 1981 and the Level-Set method which is first studied by Osher and Sethian in 1988. For the last two schemes, the shape of the free surface is determined by computing the fraction of each near-interface cell that is partially filled. The details about these schemes are discussed in the following part.

In the MAC scheme, the free surface is captured by introducing massless particles at the free surface at the initial time and following their motion. Figure 1.3 shows an example of the surface marker applications. These markers capture the detail of interface motions on scales much smaller than the grid spacing. The free surface geometry is then achieved by all the segments which are connections between adjacent markers.

MAC methods have been used extensively by many groups. Chan and Street

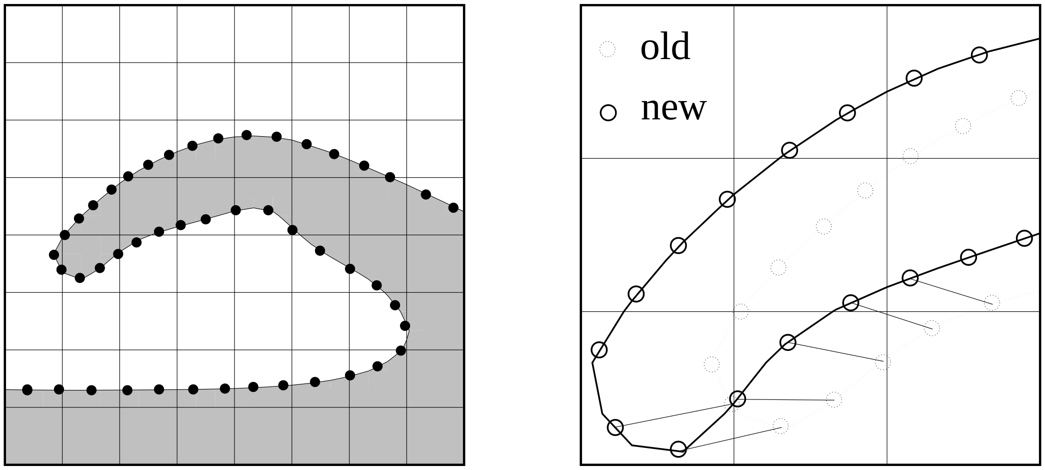

Figure 1.3. MAC method

(1969) introduced the Stanford University Modified MAC (SUMMAC) code which was shown to be a valid tool for analyzing incompressible flows with a free surface under transient conditions. Miyata group (1986) developed TUMMAC method (Tokyo University Modified Marker And Cell method) for particular engineering problems related to water wave dynamics. A modified MAC method (SIMAC; semi-implicit marker and cell) is proposed by Armenio (1997) which accurately treats unsteady high-Reynolds free surface problems. The MAC methods are favored because they can treat complex free surface phenomena, including wave breaking. The higher degree of accuracy may be achieved by representing the interface through higher order interpolation polynomials. However, intensive computational effort is needed for these methods especially in three-dimensional problems with violent free surface motions. In addition to solving the equations governing the fluid flow, one has to follow the motion of a large number of particles. This leads to high computation time and cost.

The VOF method introduces a scalar, which is usually named the volume fraction or color function, which defines the filling degree of each cell. Figure 1.4 shows the definition of VOF function. A cell with a volume fraction value of 0 is empty, and a volume fraction value of 1 means a full cell. For those partially filled cells, f is the volume fraction of the fluid in the cell. Here, in addition to the conservation equations for mass and momentum, one has to introduce and solve an equation for the filled fraction of each control volume.

$$\frac{\partial f}{\partial t} + \vec{V} \cdot \nabla f = 0 \tag{1.1}$$

The VOF method has been known for several decades and has been developed and improved continuously by many research groups. Kothe and Rider (1995) and Scardovelli and Zaleski (1999) gave good reviews for the development of the VOF method in past decades. Now the VOF method has been proven as a popular, useful

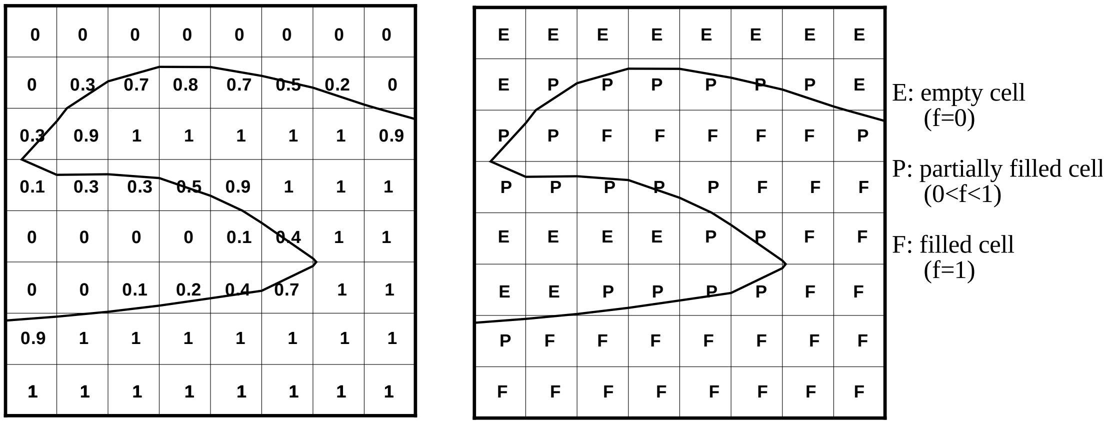

0	0	0	0	0	0	0	0
0	0.3	0.7	0.8	0.7	0.5	0.2	0
0.3	0.9	1	1	1	1	1	0.9
0.1	0.3	0.3	0.5	0.9	1	1	1
0	0	0	0	0.1	0.4	1	1
0	0	0.1	0.2	0.4	0.7	1	1
0.9	1	1	1	1	1	1	1
1	1	1	1	1	1	1	1

E	E	E	E	E	E	E	E
E	P	P	P	P	P	P	E
P	P	F	F	F	F	F	P
P	P	P	P	P	F	F	F
E	E	E	E	P	P	F	F
E	E	P	P	P	P	F	F
P	F	F	F	F	F	F	F
F	F	F	F	F	F	F	F

Figure 1.4. The definition of volume fraction

and robust tool for interface tracking. There are many commercial codes which use this method to represent interfaces, SOLA-VOF (Nichols et al., 1980), NASA-VOF3D (Torrey et al., 1987), RIPPLE (Kothe and Mjolsness, 1992) and FLOW3D (Hirt and Nichols, 1988). The widespread applications of VOF method is based on its essential advantages. The algorithm is based on a discrete representation of the conservation law. For this reason, the VOF method preserves mass in a natural way and it conserves mass well in calculations. Another advantage is the VOF method can be relatively simply extended from two-dimensional domain to three-dimensional domain. However, there is an obvious shortcoming for the VOF method. It must locate the interface in order to advect volume fraction in Equation 1.1. Low order reconstruction scheme may cause lots of errors in simulation. A lot of work had been done to develop different interface reconstruction procedures. The most typical schemes are known as simple line interface calculation (SLIC) and piecewise linear interface construction (PLIC). The SLIC is used widely in 80s' (Hirt and Nichols, 1981) and early 90s' (Lafauries et al., 1994) in the last century. This is the first order approach, O(h), which forces the reconstruction to align with one of the mesh coordinates. Figure 1.5(a) shows the actual interface and that constructed by SLIC which is much coarser. PLIC is much more accurate to fit the interface through piecewise linear segments. The interface in Figure 1.5(b) is much close to the actual surface. The VOF scheme is widely used to simulate breaking wave (Biausser et al., 2004), vigorous sloshing in tanks (Yang and Lohner, 2005), and flows around ships and submerged bodies (Huijsmans and van Groesen, 2004). Nevertheless, most of them have problems in order to build an accurate and smooth free surface for complex three-dimensional free surface problems.

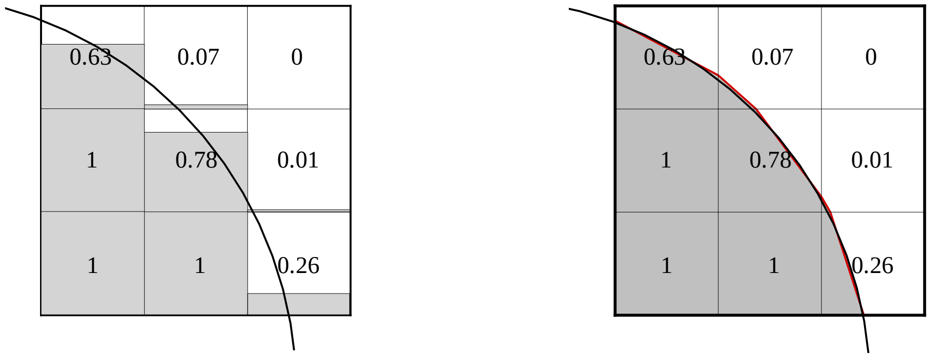

(a) SLIC

(b) PLIC

Figure 1.5. The interface reconstruction in VOF methods

Another class of interface capturing methods is based on the level set function which is introduced by Osher and Sethian (1988). The level set function ϕ which is defined in the whole domain is typically initialized as the signed distance from the interface i.e. its value at any point is the physical distance from the nearest point on the interface and its sign is positive on one side and negative on the other side. The interface is located at the one on which a level-set function $\phi = 0$ while other values of this function have no significance. The level set function varies smoothly across the interface and is advected by the local velocity field using the advection equation

$$\frac{\partial \phi}{\partial t} + \vec{V} \cdot \nabla \phi = 0 \tag{1.2}$$

As a solution of calculation, the interface can be captured at any time by locating the zero level set. In general, the computed ϕ may not remain the signed distance from the interface due to accumulated numerical errors and needs to be reinitialized for every time step. Sussman et al. (1994) proposed that this can be done by solving the following equation until the steady state is reached.

$$\frac{\partial \phi}{\partial \tau} = \mathrm{sign}(\phi_0) \cdot (1 - |\nabla \phi|) \tag{1.3}$$

Equation 1.3 guarantees that ϕ has the same sign and zero level as ϕ_0 and satisfies the condition that $|\nabla \phi| = 1$.

Sethian and Smereka (2003) provided an overview of the level set method for computing the solution to fluid-interface problems. Osher and Fedkiw (2001) discussed not only recent variants and extensions of the level set method but also a user's guide to the level set dictionary and technology. Compared to VOF methods, the level set method seems to be an extremely promising method. Because it is not necessary to do the reconstruction procedure, the level set method handles the complex interface geometries in a simple way. And surface tension effects can be incorporated easily in this method. The biggest concern of the level set method is mass loss issue. In order to improve mass conservation, many research groups expanded the original level set method. Sussman et al. (1998) first introduced a new constraint term in the redistancing scheme to improve accuracy and efficiency. A coupled level set and VOF method is developed recently by Sussman and Puckett (2000). It seems to conserve mass as well as VOF methods. A similar method, which is known as the mass conserving level set method (MCLS), is presented by Van der Pijl et al. (2005). Takahira et al. (2004) improved the reinitialization procedure of the level set function by adding a multiplier of the order of one to the constraint term in order to recover the mass. Enright et al. (2002) proposed a new numerical method to improve the mass conservation by using Lagrangian marker particles to rebuild the level set function in regions which are under-resolved. The particle level set method has been proved to be an effective way in handling topological merging, breaking and even self-intersecting of interfaces problems. Predictable improvement in mass conservation is also obtained. The level set method is widely used in many areas other than incompressible fluid flows. Gibou et al. (2003) presented a level set approach for the modeling of dendritic solidification. Pitsch and Lageneste (2002) employed the level set formulation to treat the instantaneous flame front as an interface. Asethian and Adalsteinsson (1996) used the level set method for etching, deposition, lithography development. More details of the level set methods can be found in Sethian (1996).

1.3. Method of Present Study

In the present study, we used both the interface-tracking and interface-capturing methods in conjunction with a Chimera Reynolds-Averaged Navier-Stokes (RANS) method for time-domain simulation of nonlinear waves around offshore structures. For the interface-tracking method, it is convenient to use separate body-fitted numerical grids for the structures and the ambient wave field. In the chimera domain decomposition approach, the numerical grids around the offshore structures remain fixed while the free surface grids are adjusted every time step to conform to the exact free surface. Since the submerged portion of the structures change continuously at different time instants, the interpolation between different chimera grid blocks were updated every time step to enforce conservation of mass and momentum across block boundaries over the entire simulation. In addition, an effective damping beach approach proposed by Chen and Huang (2004) was implemented on the wave maker boundary to prevent the reflected waves from reaching the wave maker boundary. This enables us to perform long-duration simulations without significantly increasing the size of the computational domain. In the present study, the chimera RANS method of Chen et al. (2000, 2001, 2002) has been generalized for time-domain simulation of fully nonlinear wave runup around two- and three-dimensional offshore structures.

The present interface-tracking method was used with considerable success by Chen et al. (2002) for time-domain simulation of barge capsizing. However, the interface-tracking method is not suitable for the simulation of more complex green water problems with the presence of water spray and air bubbles. In view of these limitations, we have also developed an interface-capturing method based on the level set method. The level set method has been incorporated into the chimera RANS method of Chen and Chen (1998) for the predictions of sloshing flows in LNG tanks and green water on offshore platforms. The governing equations are formulated in curvilinear coordinate system and discretized using the finite-analytic method of Chen et al. (1990) on a non-staggered grid. For the additional level set equations of evolution and reinitialization, we use the 3$^{\text{rd}}$ order TVD (total variation diminishing) Runge-Kutta scheme (Yu et al, 2003b) for time derivative, and the 3$^{\text{rd}}$ order ENO (essentially non-oscillatory) scheme for spatial derivatives. The present interface-capturing method is validated first for several benchmark cases including a stationary circle, the Zalesak's problem, and the stretching of a circular fluid element under prescribed free motion. The level set method was then incorporated into the chimera RANS method of Chen and Chen (1998) for complex free surface flow simulations. Calculations were performed first for dam breaking and free jet problems in single-block rectangular grids. The feasibility of using the chimera domain decomposition approach in level set method was also evaluated for the dam breaking problem using two different embedding grid systems. Finally, the new chimera RANS method was used for the simulation of a traveling solitary wave and green water on offshore platforms. These test cases clearly demonstrated that the level set method is capable of simulating violent free surface flows encountered in the wave run up on offshore platforms.

1.4. Organization

In this dissertation, A numerical method coupling level set method and chimera RANS method together is presented. After validated by some benchmark cases, such as dam breaking, solitary wave propagation and dam breaking with an obstacle, this new method is applied in some typical free surface flows. The predictions of green water over an offshore structure and impact pressure in sloshing flow show the advantages of this method.

Chapter II describes the mathematical model of Level-Set RANS method. The general equation of level set function and Reynolds-Averaged Navier-Stokes (RANS) equations are given in both physical plane and transformed plane. A large eddy approximation is used for the modeling of turbulent flows.

Chapter III presents the finite different scheme for both level set equation and RANS equations. The third order ENO scheme and TVD scheme are used to discretize the level set equation.

Chapter IV gives several validations of Level-Set RANS method. The comparison between numerical simulations and experimental results shows Level-Set RANS method can capture the free surface accurately.

Chapter V presents the predictions of impact pressure which is acting on the wall of LNG tank during sloshing flow. Six cases in both transverse and longitudinal motions are described in details. The comparison of different sensors is also shown in this chapter. All the results prove Level-Set RANS method can capture impact pressure accurately.

Chapter VI presents the green water simulation over an offshore structure. Both two-dimensional and three-dimensional simulations are shown in this chapter. The comparison between numerical and experimental results is good.

Chapter VII presents summary and conclusions.

CHAPTER II

MATHEMATICAL MODEL

2.1. Introduction

This chapter describes the mathematical model of Level-Set RANS method. The general equation of level set function and Reynolds-Averaged Navier-Stokes (RANS) equations are given in both physical plane and transformed plane. A large eddy approximation is used for the modeling of turbulent flows.

2.2. Level Set Equation

As the discussion in Chapter I, the level set function ϕ is typically defined as the signed distance from the interface. In the present algorithm, the interface is the zero level set of ϕ:

$$\Gamma = \{\vec{x} \mid \phi(\vec{x}, t) = 0\} \tag{2.1}$$

By defining $\phi < 0$ for air region and $\phi > 0$ for water region:

$$\phi(\vec{x}, t) \begin{cases} > 0 & \text{if } \vec{x} \in \text{water} \\ = 0 & \text{if } \vec{x} \in \Gamma \\ < 0 & \text{if } \vec{x} \in \text{air} \end{cases} \tag{2.2}$$

The evolution of ϕ is given by the advection equation as follows:

$$\frac{\partial \phi}{\partial t} + \vec{V} \cdot \nabla \phi = 0 \tag{2.3}$$

The transition zone is defined by $|\phi| < \varepsilon$, where is the half thickness of the interface. In the transition zone, the fluid properties are smoothed by Heaviside function $H(\phi)$:

$$H(\phi) = \begin{cases} 0 & \text{if } \phi < -\varepsilon \\ \frac{1}{2}\left[1 + \frac{\phi}{\varepsilon} + \frac{1}{\pi}\sin(\frac{\pi\phi}{\varepsilon})\right] & \text{if } -\varepsilon \leqslant \phi \leqslant \varepsilon \\ 1 & \text{if } \phi > \varepsilon \end{cases} \tag{2.4}$$

More specifically, the density and viscosity are calculated in the following way.

$$\begin{cases} \rho(\phi) = \rho_a + (\rho_w - \rho_a) \cdot H(\phi) \\ \mu(\phi) = \mu_a + (\mu_w - \mu_a) \cdot H(\phi) \end{cases} \tag{2.5}$$

where the subscripts 'a' and 'w' represent air and water, respectively. After a new level set value ϕ_0 is obtained in each time step, it is necessary to solve the re-distancing Equation 2.6 in order to ensure that the level set value remains as a real distance.

$$\frac{\partial\phi}{\partial\tau} = \text{sign}(\phi_0) \cdot (1 - |\nabla\phi|) \tag{2.6}$$

However, it is well known that numerical errors may accumulate due to repeated re-distance operations on a level set function. In order to prevent the straying of the zero level set from initial position even after many iterations, a mass constraint term proposed by Sussman and Fatemi (1999) is added to Equation 2.6 as follows:

$$\frac{\partial\phi}{\partial\tau} = L(\phi_0, \phi) + \lambda_{ij} f(\phi) \tag{2.7}$$

where,

$$\begin{cases} L(\phi_0, \phi) = \text{sign}(\phi_0)(1 - |\nabla\phi|) \\ f(\phi) \equiv H'(\phi)\,|\nabla\phi| \end{cases} \tag{2.8}$$

The coefficient λ is determined by

$$\lambda_{ij} = -\frac{\displaystyle\int_{\Omega_{ij}} H'(\phi)L(\phi_0, \phi)}{\displaystyle\int_{\Omega_{ij}} H'(\phi)f(\phi)} \tag{2.9}$$

for every grid cell $\Omega_{ij} = (x, y)\Big| \, x_{i-\frac{1}{2}} < x < x_{i+\frac{1}{2}}$ and $y_{j-\frac{1}{2}} < y < y_{j+\frac{1}{2}}$. A more detailed description of the mass constraint term is given in Sussman and Fatemi (1999).

2.3. RANS Equations

The Navier-Stokes equations are rewritten in the level set formulation. Both the density and viscosity at air-water interfaces depend on the level set function being a distance function. The fluid properties are assumed to vary smoothly across a narrow transition zone around the free surface. This enables us to obtain accurate and stable numerical results for violent free surface motions encountered in the simulations of green water on offshore platforms.

It is assumed that both water and air are governed by the incompressible Navier-Stokes equations:

$$\begin{cases} \rho_w \left(\dfrac{\partial \vec{V'}}{\partial t'} + \vec{V'} \cdot \nabla \vec{V'} \right) = \rho_w \vec{g} + \mu_w \nabla^2 \vec{V'} - \nabla p' \\ \rho_a \left(\dfrac{\partial \vec{V'}}{\partial t'} + \vec{V'} \cdot \nabla \vec{V'} \right) = \rho_a \vec{g} + \mu_a \nabla^2 \vec{V'} - \nabla p' \end{cases} \tag{2.10}$$

The above equations are normalized using the following three dimensionless variables:

$$\vec{V} = \frac{\vec{V'}}{U_0}, \quad t = \frac{t'}{t_0} = \frac{U_0}{L}\,t', \quad p = \frac{p'}{\rho_w U_0^2}$$

After dividing by $\rho_w U_0^2 / L$ and combine those two equations together by using non-dimensional density $\rho(\phi)$ and non-dimensional viscosity $\nu(\phi) = \mu(\phi)/\rho(\phi)$ as the following equation which is similar to Equation 2.5:

$$\begin{cases} \rho(\phi) = \dfrac{\rho}{\rho_w} + (1 - \dfrac{\rho}{\rho_w}) \cdot H(\phi) \\ \mu(\phi) = \dfrac{\mu}{\mu_w} + (1 - \dfrac{\mu}{\mu_w}) \cdot H(\phi) \end{cases} \tag{2.11}$$

Equations 2.10 will be:

$$\frac{\partial \vec{V}}{\partial t} + \vec{V} \cdot \nabla \vec{V} = -\frac{\delta_{i,3}}{Fr^2} + \frac{\nu(\phi)}{Re} \nabla^2 \vec{V} - \frac{1}{\rho(\phi)} \nabla p \tag{2.12}$$

where Froude number $Fr^2 = \dfrac{U_0^2}{gL}$ and Reynolds number $Re = \dfrac{\rho_w U_0 L}{\mu_w}$.

Then transform the continuity and momentum equations in the curvilinear coordinate system

$$\sum_{i=1}^{3} \frac{\partial U_i}{\partial x^i} = 0 \tag{2.13}$$

$$\frac{\partial U_i}{\partial t} + \sum_{j=1}^{3} \left(U_j \frac{\partial U_i}{\partial x^j} + \frac{\partial \overline{u_i u_j}}{\partial x^j} \right) + \frac{1}{\rho(\phi)} \frac{\partial p}{\partial x^i} - \frac{\nu(\phi)}{Re} \nabla^2 U_i + \frac{\delta_{i,3}}{Fr^2} = 0 \tag{2.14}$$

with $\nabla^2 = \sum\limits_{j=1}^{3} \dfrac{\partial^2}{\partial x^j \partial x^j}$

The Reynolds stresses $\overline{u_i u_j}$ are related to the corresponding mean rate of strain through an isotropic eddy viscosity ν_t:

$$-\overline{u_i u_j} = \nu_t \left(\frac{\partial U_i}{\partial x^j} + \frac{\partial U_j}{\partial x^i} \right) - \frac{2}{3} \delta_{ij} k \tag{2.15}$$

where $k = (\overline{uu} + \overline{vv} + \overline{ww})/2$ is the turbulent kinetic energy and δ_{ij} is the Kronecker delta. The substitution of Reynolds stresses into the momentum equations yields:

$$\begin{aligned} \frac{\partial U_i}{\partial t} + \sum_{j=1}^{3} \left[\left(U_i - \frac{\partial \nu_t}{\partial x^j} \right) \frac{\partial U_i}{\partial x^j} - \frac{\partial \nu_t}{\partial x^j} \frac{\partial U_j}{\partial x^i} \right] = -\frac{\delta_{i,3}}{Fr^2} + \left(\frac{\nu(\phi)}{Re} + \nu_t \right) \nabla^2 U_i \\ - \left(\frac{1}{\rho(\phi)} \frac{\partial p}{\partial x^i} + \frac{\partial(\frac{2}{3}k)}{\partial x^i} \right) \end{aligned} \tag{2.16}$$

Let $\varphi = U_i$ and rearrange the momentum equations as follows:

$$\nabla^2 \varphi = R_\varphi \cdot \left[\sum_{j=1}^{3} \left(U_j - \frac{\partial \nu_t}{\partial x^j} \right) \frac{\partial \varphi}{\partial x^j} + \frac{\partial \varphi}{\partial t} \right] + s_\varphi \tag{2.17}$$

where the effective viscosity is $R_\varphi = \left(\dfrac{\nu(\phi)}{Re} + \nu_t \right)^{-1}$ and the source terms are given by:

$$s_\varphi = R_\varphi \left[\frac{1}{\rho(\phi)} \frac{\partial p}{\partial x^i} + \frac{\partial (\frac{2}{3} k)}{\partial x^i} - \sum_{j=1}^{3} \frac{\partial \nu_t}{\partial x^j} \frac{\partial U_j}{\partial x^i} + \frac{\delta_{i,3}}{Fr^2} \right] \tag{2.18}$$

In curvilinear coordinate system, those terms in Equation 2.17 can be rewritten in the transformed plane as follows:

$$\begin{cases} \nabla^2 \varphi = \sum\limits_i \sum\limits_j g^{ij} \dfrac{\partial^2 \varphi}{\partial \xi^i \partial \xi^j} + \sum\limits_j f^j \dfrac{\partial \varphi}{\partial \xi^j} \\[2ex] \dfrac{\partial \varphi}{\partial t} = \dfrac{\partial \varphi}{\partial \tau} - \dfrac{1}{J} \sum\limits_i \sum\limits_j b_i^j \dfrac{\partial x^i}{\partial \tau} \dfrac{\partial \varphi}{\partial \xi^j} \\[2ex] \sum\limits_j U_j \dfrac{\partial \varphi}{\partial x^j} = \sum\limits_i U_i \left(\dfrac{1}{J} \sum\limits_j b_i^j \dfrac{\partial \varphi}{\partial \xi_j} \right) \\[2ex] -\dfrac{\partial \nu_t}{\partial x^j} \dfrac{\partial \varphi}{\partial x^j} = -\sum\limits_n \left[\dfrac{1}{J} \sum\limits_m b_n^m \dfrac{\partial \nu_t}{\partial \xi^m} \cdot \dfrac{1}{J} \sum\limits_j b_n^j \dfrac{\partial \varphi}{\partial \xi^j} \right] \end{cases} \tag{2.19}$$

here, b_i^j, g^{ij}, f^j and the Jacobian J are geometric coefficients in curvilinear coordinate system whose values can be readily evaluated in the transformed plane. Plug these terms into Equation 2.17, we will get:

$$\sum_i \sum_j g^{ij} \frac{\partial^2 \varphi}{\partial \xi^i \partial \xi^j} - \sum_j 2a_\varphi^j \frac{\partial \varphi}{\partial \xi^j} = R_\varphi \frac{\partial \varphi}{\partial \tau} + s_\varphi \tag{2.20}$$

where,

$$2a_\varphi^j = \frac{R_\varphi}{J} \sum_n b_n^j \left[U_n - \frac{\partial x_i}{\partial \tau} - \sum_m \frac{1}{J} b_n^m \frac{\partial \nu_t}{\partial \xi^m} \right] - f^i \tag{2.21}$$

note that:

$$\begin{aligned}\sum_i \sum_j g^{ij} \frac{\partial^2 \varphi}{\partial \xi^i \partial \xi^j} &= g^{11} \frac{\partial^2 \varphi}{\partial \xi^1 \partial \xi^1} + g^{22} \frac{\partial^2 \varphi}{\partial \xi^2 \partial \xi^2} + g^{33} \frac{\partial^2 \varphi}{\partial \xi^3 \partial \xi^3} \\ &\quad + 2 \left(g^{12} \frac{\partial^2 \varphi}{\partial \xi^1 \partial \xi^2} + g^{23} \frac{\partial^2 \varphi}{\partial \xi^2 \partial \xi^3} + g^{31} \frac{\partial^2 \varphi}{\partial \xi^3 \partial \xi^1} \right) \qquad (2.22)\end{aligned}$$

plug into Equation 2.20, we will get:

$$\sum_j \left(g^{jj} \frac{\partial^2 \varphi}{\partial \xi^j \partial \xi^j} - 2 a_\varphi^j \frac{\partial \varphi}{\partial \xi^j} \right) = R_\varphi \frac{\partial \varphi}{\partial \tau} + S_\varphi \qquad (2.23)$$

$$S_\varphi = s_\varphi - 2 \left(g^{12} \frac{\partial^2 \varphi}{\partial \xi^1 \partial \xi^2} + g^{23} \frac{\partial^2 \varphi}{\partial \xi^2 \partial \xi^3} + g^{31} \frac{\partial^2 \varphi}{\partial \xi^3 \partial \xi^1} \right) \qquad (2.24)$$

The momentum equations (Equation 2.23) and the continuity equation (Equation 2.13) are the Reynolds-Averaged Navier-Stokes (RANS) equations for unsteady, three-dimensional turbulent flows.

CHAPTER III

NUMERICAL MODEL

3.1. Introduction

This chapter presents the finite different scheme for both level set equation and RANS equations. The third order essentially non-oscillatory (ENO) scheme and total variation diminishing (TVD) Runge-Kutta scheme are used to discretize the level set equation. The finite analytic solution is applied for RANS equations.

3.2. Level Set Equation

We further introduce the contravariant velocity components (Chen and Patel, 1989)

$$U^i = JV^i = \sum_{j=1}^{3} b^i_j U_j \tag{3.1}$$

The level set evolution equation is written in the transformed coordinates (ξ^i, τ)

$$\frac{\partial \phi}{\partial \tau} + \sum_{i=1}^{3} \frac{\partial \left(U^i \phi\right)}{\partial \xi^i} = 0 \tag{3.2}$$

Shu and Osher (1989) discussed the rth order TVD Runger-Kutta time discretization in details. In the present study, Equation 3.2 is advanced using the 3$^{\text{rd}}$-order TVD Runge-Kutta scheme which is total variation stable:

$$\begin{cases} \phi^{(1)} = \phi^{(n)} - \Delta\tau \cdot R\left(\phi^{(n)}\right) \\ \phi^{(2)} = \dfrac{3}{4}\,\phi^{(n)} + \dfrac{1}{4}\,\phi^{(1)} - \dfrac{\Delta\tau}{4} \cdot R\left(\phi^{(1)}\right) \\ \phi^{(3)} = \dfrac{1}{3}\,\phi^{(n)} + \dfrac{2}{3}\,\phi^{(2)} - \dfrac{2\Delta\tau}{3} \cdot R\left(\phi^{(2)}\right) \end{cases} \tag{3.3}$$

where $R(\phi) = \dfrac{\partial\left(U^i\phi\right)}{\partial\xi^i}$.

There are two ways to discretize the spatial operator R, ENO scheme (Shu 1997) and Hamilito-Jacobi ENO scheme (Osher and Fedkiw, 2003). The former evaluates ϕ values at cell faces, while the later evaluates the flux values directly at grid points.

For ENO scheme, the spatial operator R is discretized in the transformed plane (ξ, η, ζ) in a conservative manner.

$$\begin{aligned} \frac{\partial\left(U^i\phi\right)}{\partial\xi^i} = {} & \left(U^1\phi\right)_{i+\frac{1}{2},j,k} - \left(U^1\phi\right)_{i-\frac{1}{2},j,k} + \left(U^2\phi\right)_{i,j+\frac{1}{2},k} - \left(U^2\phi\right)_{i,j-\frac{1}{2},k} \\ & + \left(U^3\phi\right)_{i,j,k+\frac{1}{2}} - \left(U^3\phi\right)_{i,j,k-\frac{1}{2}} \end{aligned} \tag{3.4}$$

The cell-face values of ϕ are constructed based on the left-shift parameter r_1, r_2, r_3 which are representing different orders. The first order ENO scheme is same as the first order upwind scheme which is described as follows:

$$\phi_{i+\frac{1}{2}} = \begin{cases} \phi_{i+1} & \text{if } r_1 = 0 \\ \phi_i & \text{if } r_1 = 1 \end{cases} \tag{3.5}$$

with r_1 defined as follows:

$$r_1 = \begin{cases} 1 & \text{if } U^1_{i+\frac{1}{2}} \geqslant 0 \\ 0 & \text{if } U^1_{i+\frac{1}{2}} < 0 \end{cases} \tag{3.6}$$

The 2^{nd} order ENO scheme is introduced as follows:

$$\phi_{i+\frac{1}{2}} = \begin{cases} \frac{3}{2}\,\phi_{i+1} - \frac{1}{2}\,\phi_{i+2} & \text{if } r_2 = -1 \\ \frac{1}{2}\,\phi_i + \frac{1}{2}\,\phi_{i+1} & \text{if } r_2 = 0 \\ -\frac{1}{2}\,\phi_{i-1} + \frac{3}{2}\,\phi_i & \text{if } r_2 = 1 \end{cases} \tag{3.7}$$

with r_2 defined in terms of r_1 as follows:

$$r_2 = \begin{cases} r_1 & \text{if } \left|\delta\phi_i^{-r_1+1}\right| \geqslant \left|\delta\phi_i^{-r_1}\right| \\ r_1 - 1 & \text{if } \left|\delta\phi_i^{-r_1+1}\right| < \left|\delta\phi_i^{-r_1}\right| \end{cases} \tag{3.8}$$

The 3^{rd} order ENO scheme is introduced as follows:

$$\phi_{i+\frac{1}{2}} = \begin{cases} \frac{11}{6}\,\phi_{i+1} - \frac{7}{6}\,\phi_{i+2} + \frac{1}{3}\,\phi_{i+3} & \text{if } r_3 = -1 \\ \frac{1}{3}\,\phi_i + \frac{5}{6}\,\phi_{i+1} - \frac{1}{6}\,\phi_{i+2} & \text{if } r_3 = 0 \\ -\frac{1}{6}\,\phi_{i-1} + \frac{5}{6}\,\phi_i + \frac{1}{3}\,\phi_{i+1} & \text{if } r_3 = 1 \\ \frac{1}{3}\,\phi_{i-2} - \frac{7}{6}\,\phi_{i-1} + \frac{11}{6}\,\phi_i & \text{if } r_3 = 2 \end{cases} \tag{3.9}$$

with r_3 defined in terms of r_2 as follows:

$$r_3 = \begin{cases} r_2 & \text{if } \left|\delta^2\phi_i^{-r_2+1}\right| \geqslant \left|\delta^2\phi_i^{-r_2}\right| \\ r_2 + 1 & \text{if } \left|\delta^2\phi_i^{-r_2+1}\right| < \left|\delta^2\phi_i^{-r_2}\right| \end{cases} \tag{3.10}$$

Denoting:

$$\begin{cases} \delta\phi_i^{-1} = \phi_i - \phi_{i-1} \\ \delta\phi_i^{0} \;\;= \phi_{i+1} - \phi_i \\ \delta\phi_i^{1} \;\;= \phi_{i+2} - \phi_{i+1} \end{cases} \qquad \begin{cases} \delta^2\phi_i^{-1} = \phi_{i-2} - 2\phi_{i-1} + \phi_i \\ \delta^2\phi_i^{0} \;\;= \phi_{i-1} - 2\phi_i + \phi_{i+1} \\ \delta^2\phi_i^{1} \;\;= \phi_i - 2\phi_{i+1} + \phi_{i+2} \\ \delta^2\phi_i^{2} \;\;= \phi_{i+1} - 2\phi_{i+2} + \phi_{i+3} \end{cases}$$

and we use the same definitions for subscripts (j, k) in the (η, ζ) directions.

In order to avoid the logical structures to distinguish whether a given stencil is completely inside the computational domain, one could set all the ghost values outside the computational domain to be very large with large variations. This way the ENO choosing procedure will automatically avoid choosing any stencil containing ghost points.

For Hamilton-Jacobi ENO scheme, the flux values $\frac{\partial \phi}{\partial \xi^i}$ is constructed directly at each grid point (i, j, k) in the transformed plane (ξ, η, ζ). Here, we still demonstrate the discretizations in ξ direction as an example. Note that $\Delta\xi = \Delta\eta = \Delta\zeta = 1$. The algorithm is described as follows:

1. Construct the divided difference tables D^0, D^1, D^2, D^3 as follows:

$$\begin{cases} D_k^0 &= \phi_k \\ D_{k+\frac{1}{2}}^1 &= D_{k+1}^0 - D_k^0 \\ D_k^2 &= \dfrac{D_{k+\frac{1}{2}}^1 - D_{k-\frac{1}{2}}^1}{2} \\ D_{k+\frac{1}{2}}^3 &= \dfrac{D_{k+1}^2 - D_k^2}{3} \end{cases}$$

2. To find $\left(\frac{\partial \phi}{\partial \xi}\Big|_i\right)^-$, start with $k = i - 1$, and to find $\left(\frac{\partial \phi}{\partial \xi}\Big|_i\right)^+$, start with $k = i$.

3. Define $\frac{\partial \phi}{\partial \xi}\Big|_i = D_{k+\frac{1}{2}}^1$

4. If $|D_k^2| < \left|D_{k+1}^2\right|$ then set $c = D_k^2$ and $k^* = k - 1$ else set $c = D_{k+1}^2$ and $k^* = k$.

   And $\frac{\partial \phi}{\partial \xi}\Big|_i = c(2(i-k) - 1)$

5. If $\left|D_{k^*+\frac{1}{2}}^3\right| < \left|D_{k^*+\frac{3}{2}}^3\right|$ then set $c^* = D_{k^*+\frac{1}{2}}^3$ else set $c^* = D_{k+\frac{3}{2}}^3$.

   And $\frac{\partial \phi}{\partial \xi}\Big|_i = c^*(3(i-k^*)^2 - 6(i-k^*) + 2)$

6. If $U_i^1 \geqslant 0$ discretize $\frac{\partial \phi}{\partial \xi}\Big|_i$ by $\left(\frac{\partial \phi}{\partial \xi}\Big|_i\right)^-$. If $U_i^1 < 0$ discretize $\frac{\partial \phi}{\partial \xi}\Big|_i$ by $\left(\frac{\partial \phi}{\partial \xi}\Big|_i\right)^+$.

There are the same procedures for $\left.\frac{\partial \phi}{\partial \eta}\right|_j$ and $\left.\frac{\partial \phi}{\partial \zeta}\right|_k$.

3.3. RANS Equations

The momentum equations are solved by the 12-point finite analytic scheme of Chen et al. (1990). In the finite analytic approach, Equation 2.23 are locally linearized in each rectangular numerical element. After that, a 12-point finite analytic formula for unsteady, three-dimensional, elliptic equations can be obtained in the form:

$$\begin{aligned}\varphi_P = {} & \frac{1}{1 + C_P\left(C_U + C_D + \frac{R}{\Delta\tau}\right)} \cdot \\ & \left[\sum_1^8 C_{nb}\varphi_{nb} + C_P\left(C_U\varphi_U + C_D\varphi_D + \frac{R}{\Delta\tau}\varphi_P^{n-1}\right) - C_P(S_\varphi)_P\right]\end{aligned} \tag{3.11}$$

The subscripts 'U' and 'D' represent points in the stencil, upstream and downstream of 'P' and the subscript 'nb' denotes neighboring nodes. The finite-analytic coefficients (C_P, C_U, C_D, C_{nb}) can be found in Chen et al.(1990).

The velocities U_i in Equation 3.11 was solved by the PISO/SIMPLER algorithm. The velocities and pressure are defined at the grid nodes while the contravariant pseudovelocities are at staggered locations. The velocities U_i were decomposed into a pseudovelocity field $\hat{U}_i$ plus the pressure-gradient terms contained in the source function and can be found as follows:

$$U_{i,P} = \hat{U}_i - \frac{\frac{1}{J}C_P R}{1 + C_P\left(C_U + C_D + \frac{R}{\Delta\tau}\right)} \frac{1}{\rho(\phi)} \sum_j b_i^j \frac{\partial p}{\partial \xi^j} \tag{3.12}$$

where the pseudo-velocities are defined by:

$$\hat{U}_i = \frac{1}{1 + C_P\left(C_U + C_D + \dfrac{R}{\Delta\tau}\right)} \cdot \tag{3.13}$$
$$\left[\sum_1^8 C_{nb}U_{i,\,nb} + C_P\left(C_U U_{i,\,U} + C_D U_{i,\,D} + \frac{R}{\Delta\tau}U_{i,\,P}^{n-1}\right) - C_P R\left(S_{U_i} + \frac{1}{Fr^2}\right)\right]$$

A resulting equation for pressure is derived by requiring the contravariant velocity field U^i to satisfy the equation of continuity.

$$\begin{aligned}(E_d^{11} + E_u^{11} + E_n^{22} + E_s^{22} + E_e^{33} + E_w^{33})p_P = {} & E_d^{11}p_D + E_u^{11}p_U + E_n^{22}p_{NC} \\ & + E_s^{22}p_{SC} + E_e^{33}p_{EC} + E_w^{33}p_{WC} - \hat{D}\end{aligned} \tag{3.14}$$

where,

$$\begin{aligned}\hat{D} &= \hat{D}_d^1 - \hat{D}_u^1 + \hat{D}_n^2 - \hat{D}_s^2 + \hat{D}_e^3 - \hat{D}_w^3 \\ &= \frac{1}{2}\left(\hat{D}_D^1 - \hat{D}_U^1 + \hat{D}_{NC}^2 - \hat{D}_{SC}^2 + \hat{D}_{EC}^3 - \hat{D}_{WC}^3\right)\end{aligned} \tag{3.15}$$

3.4. General Solution Procedure

In the current Level-Set RANS method, the fixed numerical grid is used to cover both air and water. The grid can be decomposed into a number of computational blocks. The grid near the structure can be refined in order to get accurate solutions. The PEGSUS program (Suhs and Tramel 1991) is employed to determine the interpolation information for linking grids before calculations.

The overall solution procedure consists of one loop for pressure, velocity and turbulence quantities and another loop for level set function ϕ. The former loop solves a system of tridiagonal matrices by using an iterative ADI scheme while the later solves ϕ by using ENO and TVD schemes.

For the simulations of LNG tank sloshing flow and green water prediction, the solution procedure can be summarized as follows:

1. Construct the grids for each component in the simulation.
2. Determine interpolation information for linking grids using the PEGSUS program.
3. Construct a boundary condition table for velocity, pressure, turbulence quantities and level set function ϕ on each face of the blocks.
4. Specify the initial conditions for $u, v, w, p, k, \varepsilon, \phi$.
5. Calculate the geometric coefficients b_i^j, g^{ij}, etc.
6. Calculate the source function s_φ and solve the finite analytic coefficients C_U, C_D, C_P etc.
7. Solve the discretization formula of RANS equations to obtain the velocity and turbulence quantities using the iterative ADI scheme.
8. Calculate the pseudovelocities $\hat{U}_i$, $\hat{U}^i$, and pressure p using the iterative ADI scheme.
9. Repeat steps 7 and 8
10. Calculate the level set function ϕ, using ENO and TVD schemes.
11. Do the redistancing procedure to ensure that ϕ is the physical distance from the interface.
12. Repeat steps 10 and 11.
13. Return to step 5 for the next time step.

CHAPTER IV

TEST CASES AND VALIDATIONS

4.1. Re-distancing Procedure

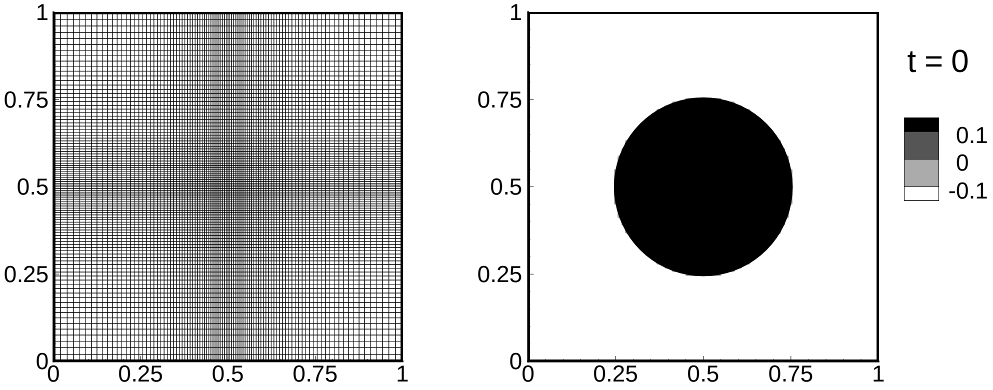

Figure 4.1. Grid and initial ϕ in re-distancing procedure

In order to test the re-distancing procedure in level set method, we initialize a discontinuous level set function in a non-uniform rectangular grid with 101×101 grid points. The domain size is 1.0×1.0 and the interface is a circle centered at $(0.5, 0.5)$ with a radius of 0.25. The level set function is initially assigned a value of 0.1 outside the circle and $+0.1$ inside the circle as shown in Figure 4.1. We choose the artificial time increment to be the smallest grid size, i.e., $\Delta t = 0.005$. It can be shown in this test case that we need only to recalculate the level set ϕ for $L/\Delta t$ time steps to obtain the correct distance up to L.

Figure 4.2 shows the contours of ϕ at different artificial time $t = 0.1, 0.2, 0.3, 0.4$. It is seen that the devolution of ϕ starts from the interface where the zero level set is, and propagate on both sides of the interface. Theoretically, ϕ is the physical distance

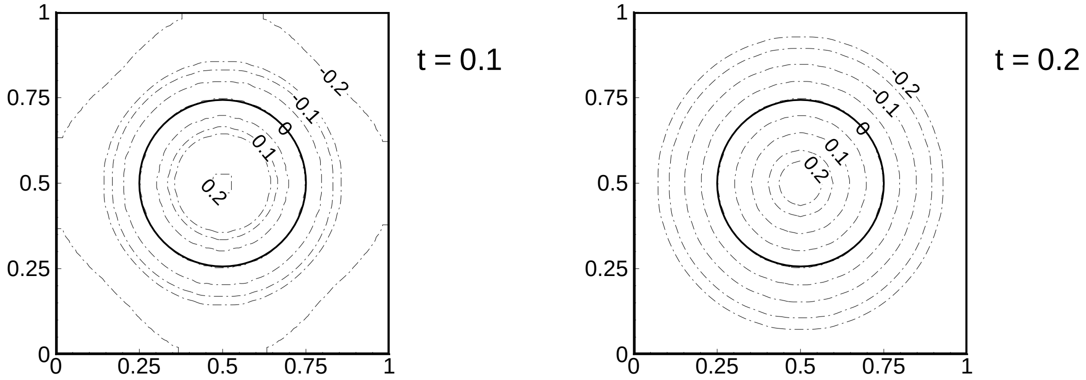

(a) t=0.1 (b) t=0.2

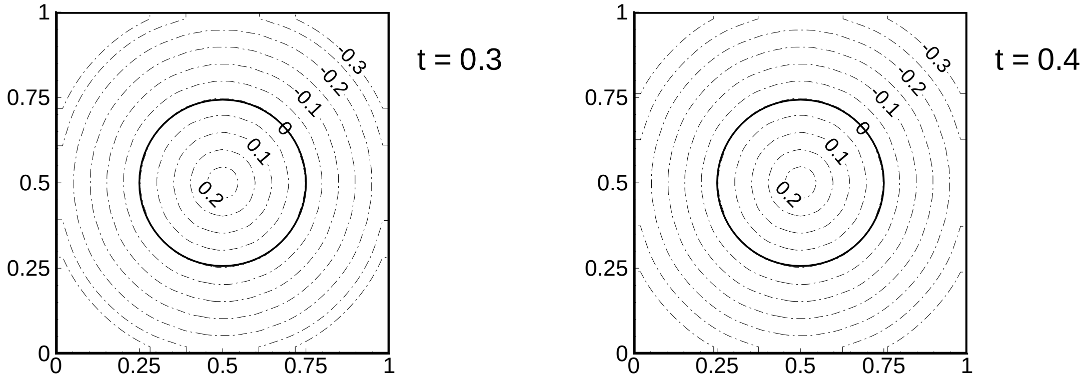

(c) t=0.3 (d) t=0.4

Figure 4.2. The ϕ evolution in re-distancing procedure

(i.e., $|\nabla\phi| = 1$) from the zero level set in the circle whose radius is equal to the artificial time t. It is clearly seen from Figure 4.2 that the zero level set does not change during the calculation. If we continue the calculations for more time steps until the steady state is reached, then will represent the physical distance from the interface over the entire domain as shown in the last image at $t = 0.4$. We also repeated the same calculation with uniform grid spacing and obtained exactly the same result. This test case provided a good indication on the number of time steps needed for the re-distance procedure. In our numerical simulations, the initial level set is typically very close to the physical distance. Therefore, very few time steps are needed to obtain the steady state solution in the re-distance procedure. More specifically, we have chosen a transition zone width of two times of grid size and a time increment of one grid size. Therefore, only two iterations are needed in the present simulations for re-distancing of the level set function.

4.2. Zalesak's Problem

The Zalesak's problem of a rotating slotted disk is a benchmark case for testing an advection scheme. A slotted solid disk rotates around a center with a constant angular velocity. The slotted disk has a radius of 15 and a lot width of 6. It is initially located at (50,75) in the domain of size (100,100). The angular velocity Ω is set to 0.01 so that the disk returns to its original position at every 200π (≈ 628) time units. Figure 4.3 shows the rotation process obtained at $t = 0, 157, 314, 471$ and 628. The dotted line is the initial geometry of disk. The dash line is the final result without mass constraint in the re-distance procedure. It can be seen that the slotted disk matches its original shape well after a circle rotation except the sharp corners. And compared with the rotation without mass constraint, it has good mass conservation during the rotation. This test proves that it is necessary to add the mass constraint term in re-distancing scheme.

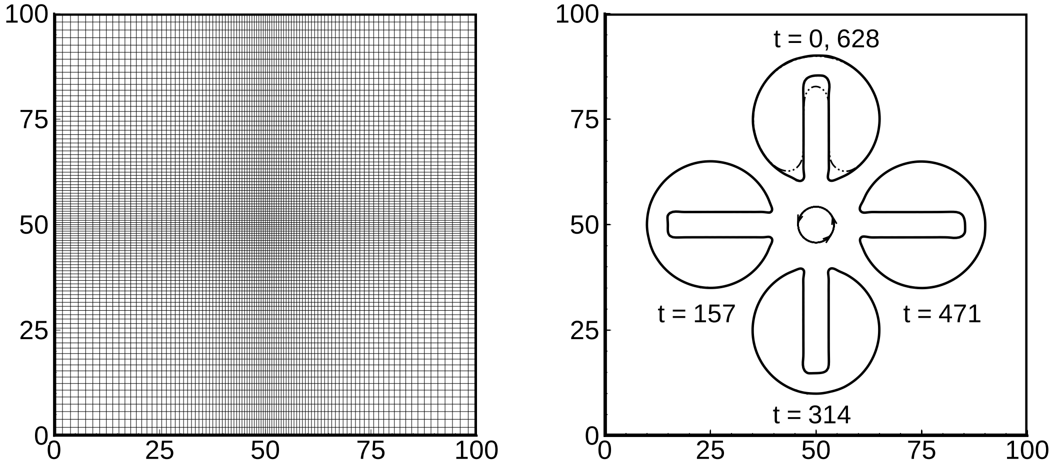

(a) numerical grid (b) predicted interfaces

Figure 4.3. Zalesak's problem

4.3. Fluid Element Stretching

In the third test case, a circular fluid element is placed in a swirling shear flow field within a unit square. The flow field is prescribed in term of a two-dimensional stream function φ:

$$\varphi = \frac{1}{\pi} \sin^2(\pi y)\, \sin^2(\pi z)$$

This corresponds to a solenoidal velocity field with the following velocity components:

$$v = -\sin^2(\frac{\pi y}{100})\, \sin(\frac{\pi z}{50})$$

$$w = \sin^2(\frac{\pi z}{100})\, \sin(\frac{\pi y}{50})$$

The circular fluid element is stretched into a thin filament by the shearing velocity field as shown in Figure 4.4. This case provides a challenging test for surface-tracking and surface-capturing methods. The circle is initially centered at (50,75) with a radius of 15. The total mass $M(t)=\int_{\Omega} H(\phi)d(\Omega)$ is evaluated at every time step to monitor the performance of the mass constraint term. As shown in Figure 4.5, the total mass decreases slightly from 706.858 to 704.694 (i.e., 0.3%). Therefore, the mass constraint term is very effective in maintaining global mass conservation during the advection of interfaces.

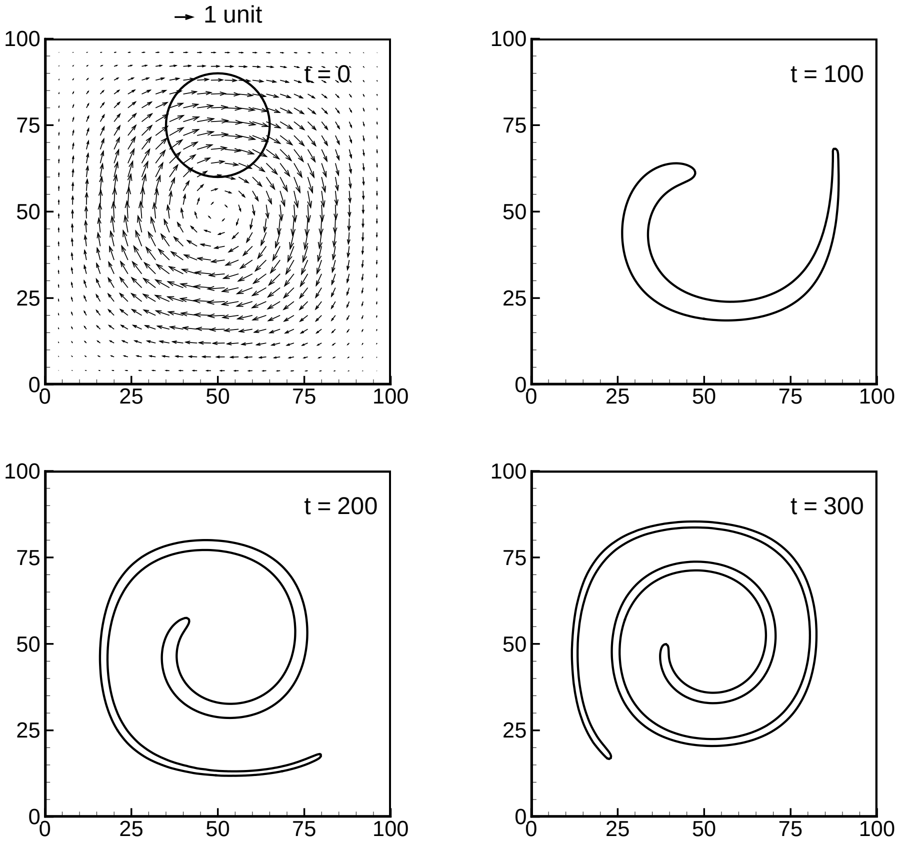

Figure 4.4. Stretching of a circular fluid element in swirling flow

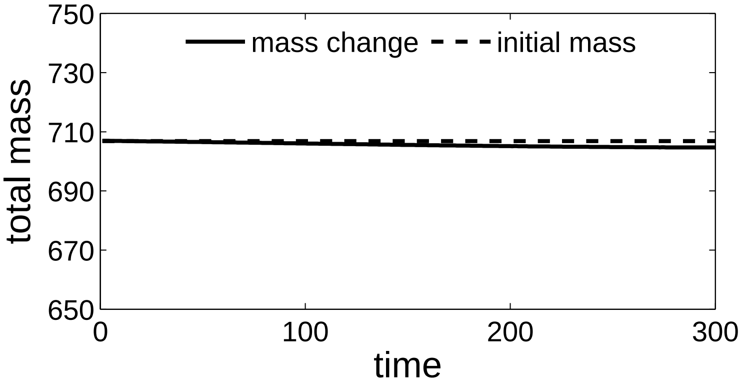

Figure 4.5. Mass change in a circular fluid element stretching

4.4. Fluid Element Stretching and Restoration

The last test case of the interface-capturing and re-distancing procedures involves the stretching and restoration (shrinking) of a circular fluid element. In this case, the circular fluid element is subjected to a swirling flow with oscillatory velocity components given by:

$$v = -\sin^2(\frac{\pi y}{100})\ \sin(\frac{\pi z}{50})\ \cos(\frac{\pi t}{T})$$
$$w = \sin^2(\frac{\pi z}{100})\ \sin(\frac{\pi y}{50})\ \cos(\frac{\pi t}{T})$$

It is worthwhile to note that the initial velocity field for the present swirling flow is identical to that considered in the previous test case. However, the swirling velocity decreases gradually as the circular fluid element is stretched out during $0<t<T/2$. At $T/2$, the flow came to a complete stop and begins to reverse its direction. During $T/2<t<T$, the stretched fluid element shrinks back gradually due to the reversal of the swirling flow direction. The fluid element is expected to recover its initial circular shape at $t=T$ for a perfect interface-capturing scheme. It is seen from Figure 4.6 that the present interface-capturing technique successfully restored the original shape

of the circular fluid element. As noted in Figure 4.7 there is a very slight reduction of the total mass $M(t)=\int_\Omega H(\phi)d(\Omega)$ from 706.858 to 701.845 (i.e., 0.7%) after one complete cycle.

4.5. Propagation of a Solitary Wave

Propagation of a solitary wave is a simple and practical free surface problem that has been studied experimentally and numerically. To generate a solitary wave, one can make use of the Laitone's analytical approximation. Here we release an initially still water surface with a Boussinesq profile from the left vertical wall which is in hydrostatic balance.

$$A(y,0) = A_0 \Big/ \cosh^2\left(\frac{\sqrt{3A_0}\cdot y}{2}\right)$$

Figure 4.8 shows the wave profile at different time for the case. The corresponding velocity profile at $t=10\,\mathrm{s}$ is shown in Figure 4.9. It is seen that the wave amplitude decay slightly during propagation as a result of the viscous effects.

To quantify the viscous damping characteristics of the wave, we compute three waves with different initial amplitude, and compare the results with those predicted by the perturbation theory of Mei (1989):

$$A^{-1/4} = A_0^{-1/4} + 0.08356\left(\frac{\nu}{(gh)^{1/2}h^{3/2}}\right)^{1/2}\cdot\left(\frac{Ct}{h}\right)$$

where Ct is essentially the distance traveled by the solitary wave. This formula has been verified against the measurements of Russell. In this study, we set the theoretical wave velocity $C=\sqrt{gh}=1\mathrm{m/s}$ and the water dynamic viscosity $\nu=2.0\times10^{-6}\mathrm{m}^2/\mathrm{s}$. This gives a Reynolds number $Re=Ch/\nu=5\times10^4$. It is seen from Figure 4.10 that the present simulation result is in close agreement with the perturbation theory in the middle section of the tank. The discrepancies on the right hand side of the tank

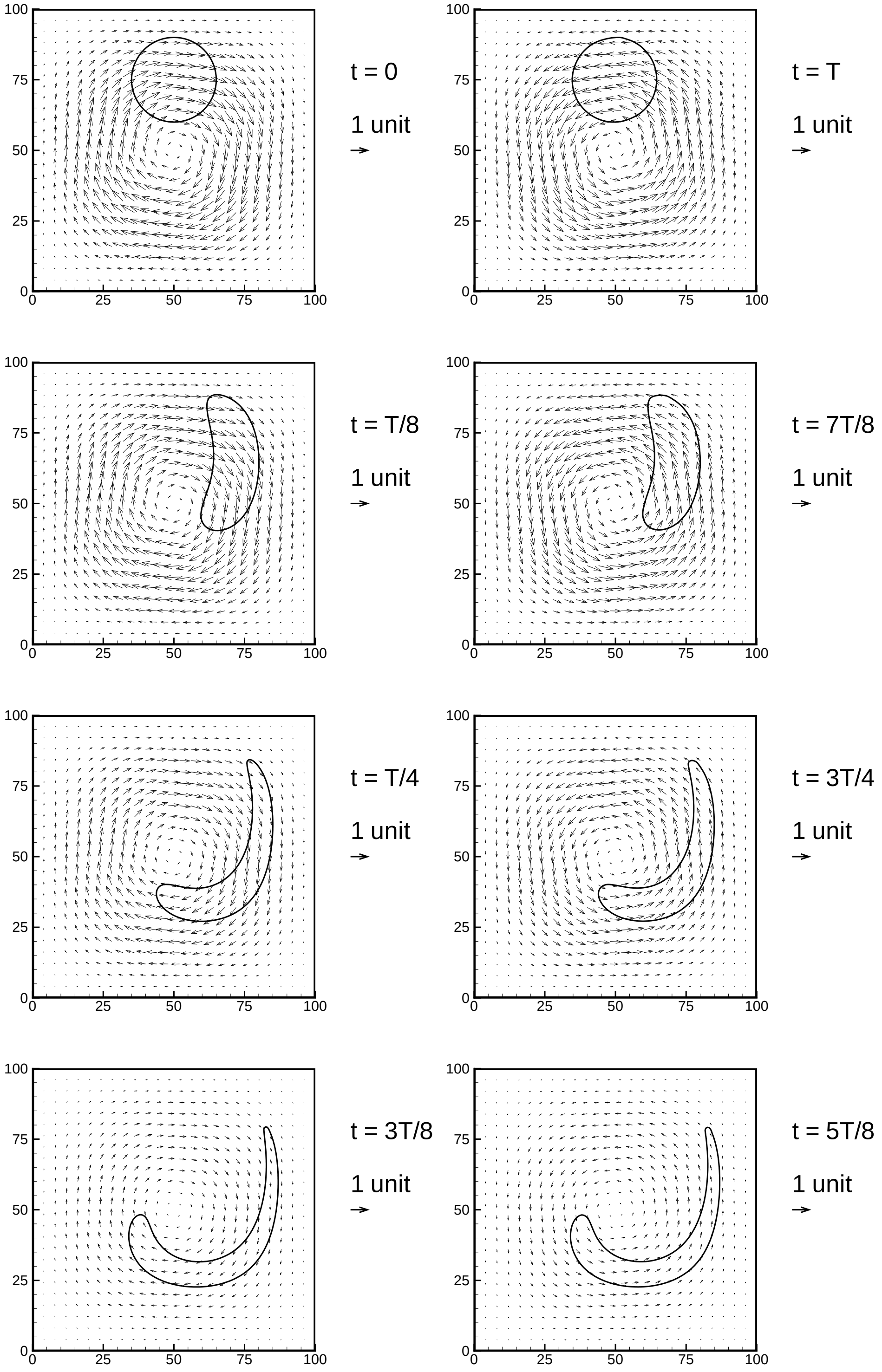

Figure 4.6. The level-set evolution during stretching and shrinking

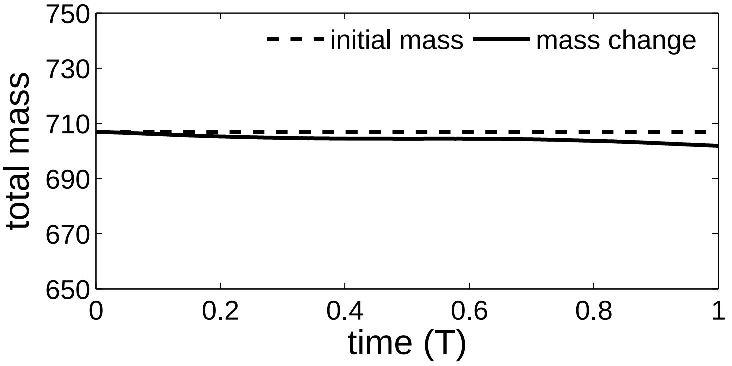

Figure 4.7. Mass change in stretching and shrinking

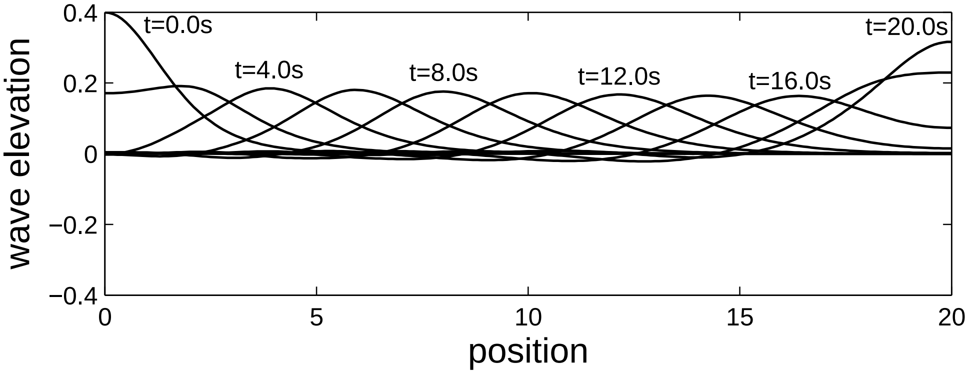

Figure 4.8. Propagation of solitary wave; $A_0 = 0.4$

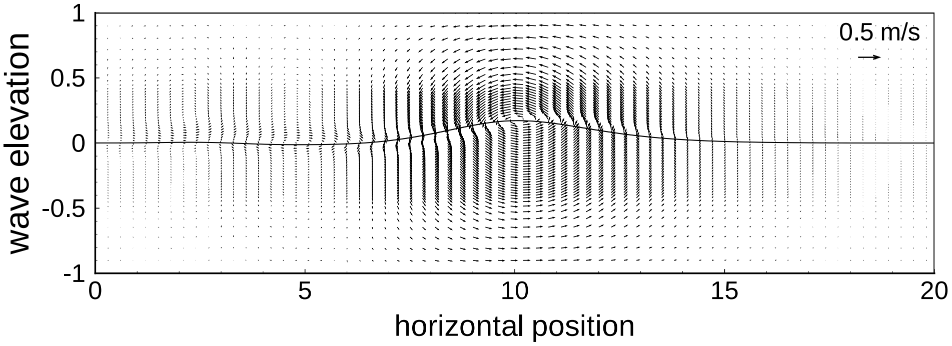

Figure 4.9. Typical velocity field of a solitary wave

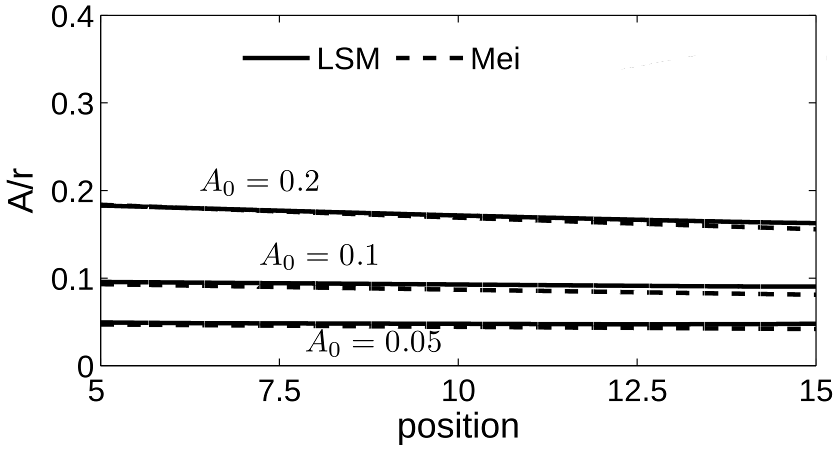

Figure 4.10. Comparison in solitary wave propagation

are due to the reflection of the solitary wave by the tank wall.

4.6. Dam Breaking

The collapse of a water column on a rigid horizontal plane is also called a broken-dam problem. It is used to simulate the abrupt failure of a dam, in which an initially blocked still water column starts to spread out after the barrier is removed. The dam-breaking problem has been the subject of many previous numerical and experimental investigations. In our simulation, the computational domain size is 2.0m × 5.0m, and the parameters used in this study are the same as those used earlier in solitary wave simulation. The half-thickness of the air-water interface is fixed at two times of grid spacing, and the time step size used in the re-distancing procedure is equal to one grid spacing.

Figure 4.11 shows snapshots of water surface profiles and the associated velocity fields for air and water in the entire computational domain at selected time instants. Initially, the water column is in hydrostatic balance with pressure linearly proportional to the water depth. When the vertical barrier is removed at $t = 0$, the water

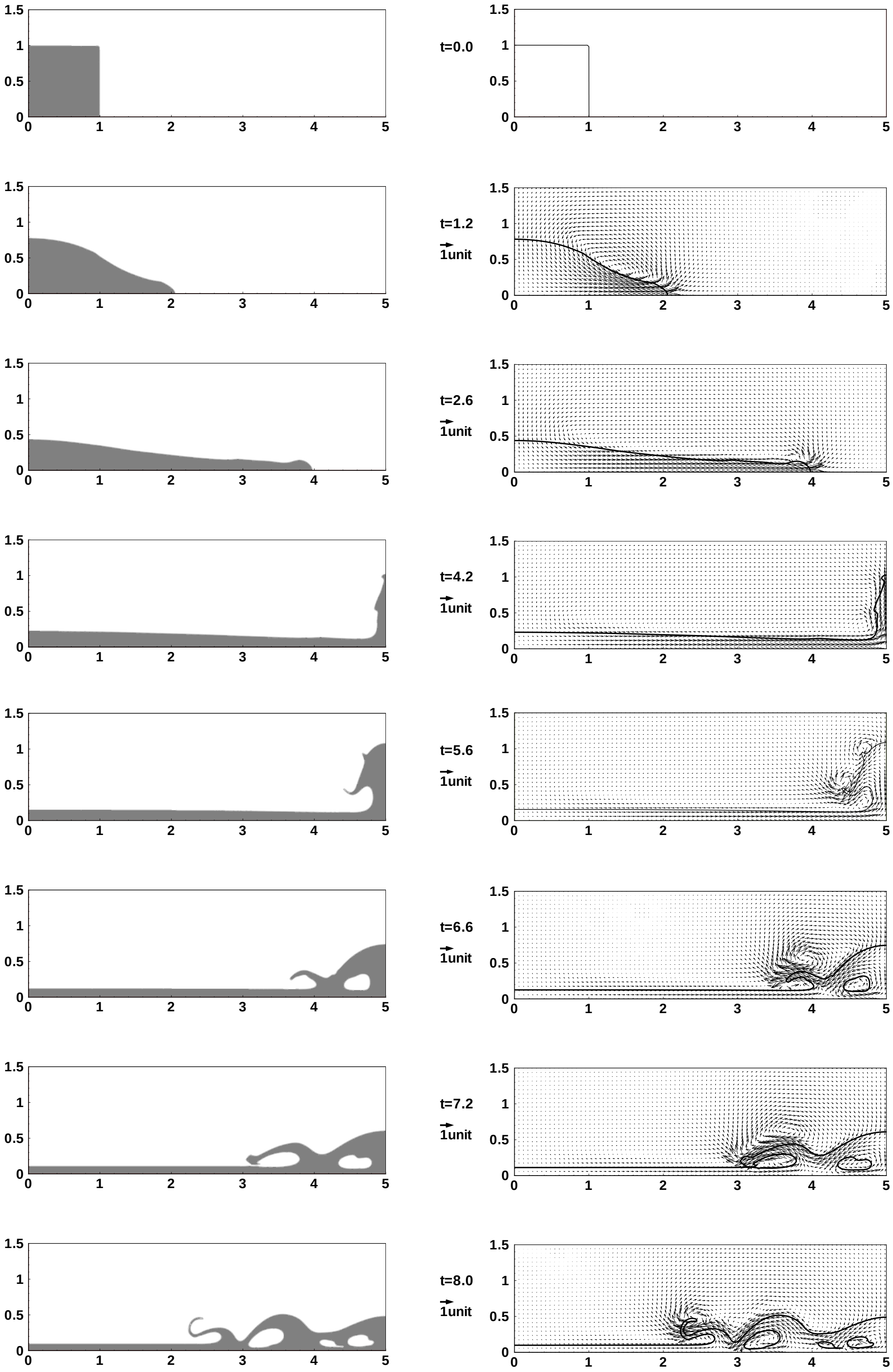

Figure 4.11. Free surface and velocity vectors in dam-breaking

column collapses and flushes to the right due to the large pressure difference between the water and air at the interface. When the front of the water column hits the tank wall, it was pushed upward against the wall by the momentum of the water flow. As the water climbs up the tank wall, the front velocity decreases gradually as the fluid momentum is being converted to potential energy. After the water front comes to a complete stop on the tank wall, it begins to fall back into the bottom water pool due to the gravitational force. The collision of falling water mass with the water in the pool produces a splash wave traveling to the left with a thin and elongated surge front. Several air pockets were observed when the simulation was terminated at $t = 8.0$. It is also clearly seen from the velocity vector plots that the violent free surface motions also induce very strong vortices at the surge front.

Figure 4.12 shows the comparison between the numerical simulation and experiment results (Martin and Jouce, 1952). The water column is 1×1 initially. So the surge front position and remaining water columns height at $t = 0$ all equal to 1. The maximum surge front position is 5 which is the tank length. The water front already hit the right side wall at the moment when the surge front position equals to 5. After the surge front hit the wall and bounce back, there is still some water remaining at

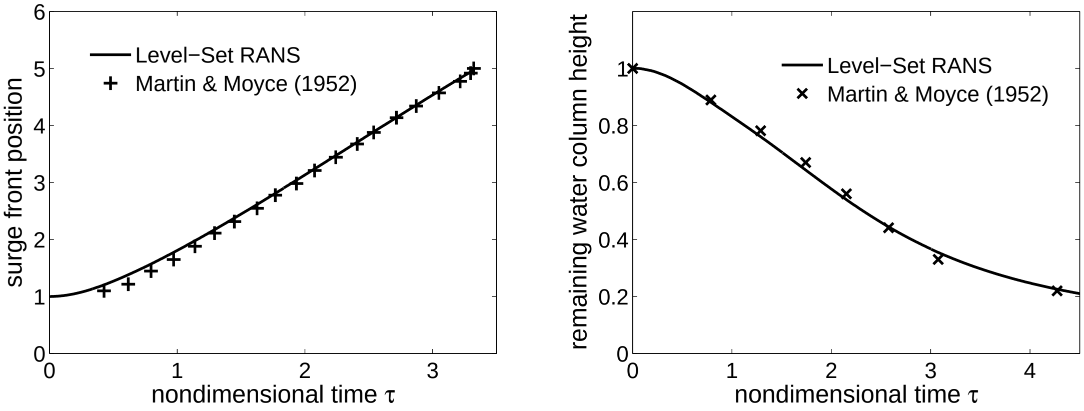

Figure 4.12. 2D dam-breaking problem

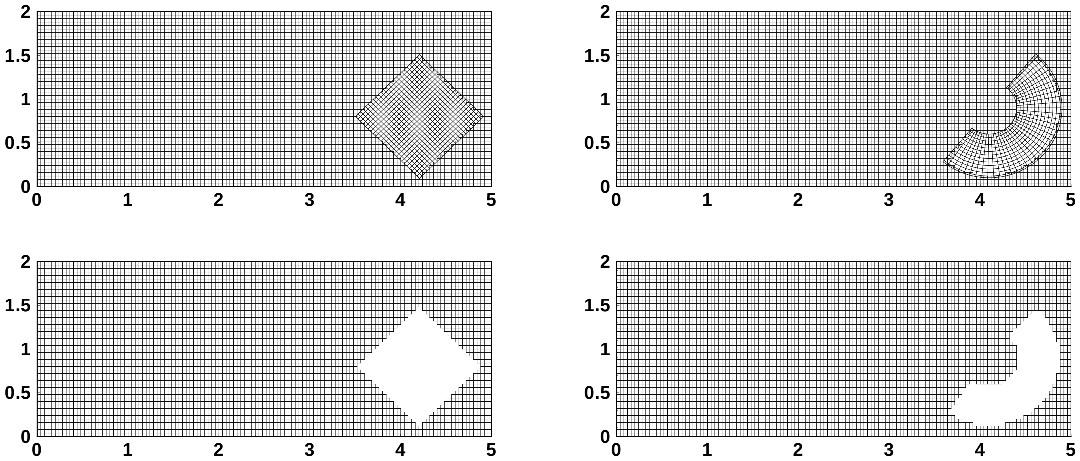

Figure 4.13. Chimera grids for dam-breaking problems

left side wall. Both comparisons are in excellent agreements. This tells us that Level Set RANS method could be used to capture free surface flow accurately.

It has been demonstrated in previous studies by Chen (2005) that the chimera domain decomposition approach provides an effective means to deal with complex geometry and flow conditions by allowing the judicial use of grid overlapping or embedding techniques to simplify the grid generation process. The chimera grid system also allows for selective refinement of the numerical grids in areas of high gradient without significant increase on the overall computing cost. In the present study, the feasibility of using chimera domain decomposition approach in conjunction with level set function was demonstrated for the dam-breaking problem using two composite grid systems shown in Figure 4.13. In both cases, we made a hole in our computational domain first, and then patched the hole with two different grids, a rectangular grid and a semi-circular grid. In the chimera domain decomposition approach, the PEGSUS program of Suhs and Tramel (1991) was employed to identify the hole points and provide interpolation information for the hole fringe points as well as the outer boundary points for the embedded grid blocks.

Figure 4.14 shows the simulation results for two different grid embedding systems. It is clearly seen that the air-water interface remains smooth across the overlap region between different computational blocks. This indicates that the interpolation of velocity, pressure, turbulence quantities, and level-set function, is robust and accurate for arbitrary grid systems. A detailed comparison of the water surfaces and velocity vector plots in Figures 4.13 and 4.14, however, indicates that the air-water interface is somewhat affected by different implementation of the grid-capturing technique in different computational blocks. More specifically, the half thickness of the interface was chosen to be equal to two grid spacing in all three cases. Since the grid sizes are significantly different for two different grid patches, the predicted water surface profiles and air bubble sizes was found to change slightly at later stages of the simulation beyond $t > 6$s. There is a slight phase lag of the surge front for the semi-circular grid case. Nevertheless, the velocity fields induced by the violent free surface motion are quite similar for all three test grids as seen in Figure 4.15.

Calculations were also performed for the dam breaking problem in a three-dimensional rectangular tank as shown in Figure 4.16. During the initial stage of the simulation, the flow remains two-dimensional when running up the opposite wall and falling back to the water pool. However, the splash wave produced by the falling water mass quickly developed into a complex 3D breaking wave pattern with the presence of small water droplets and trapped air bubbles. It is quite clear that the level-set method is capable of resolving violent free surface flow with complex three-dimensional air-water interfaces.

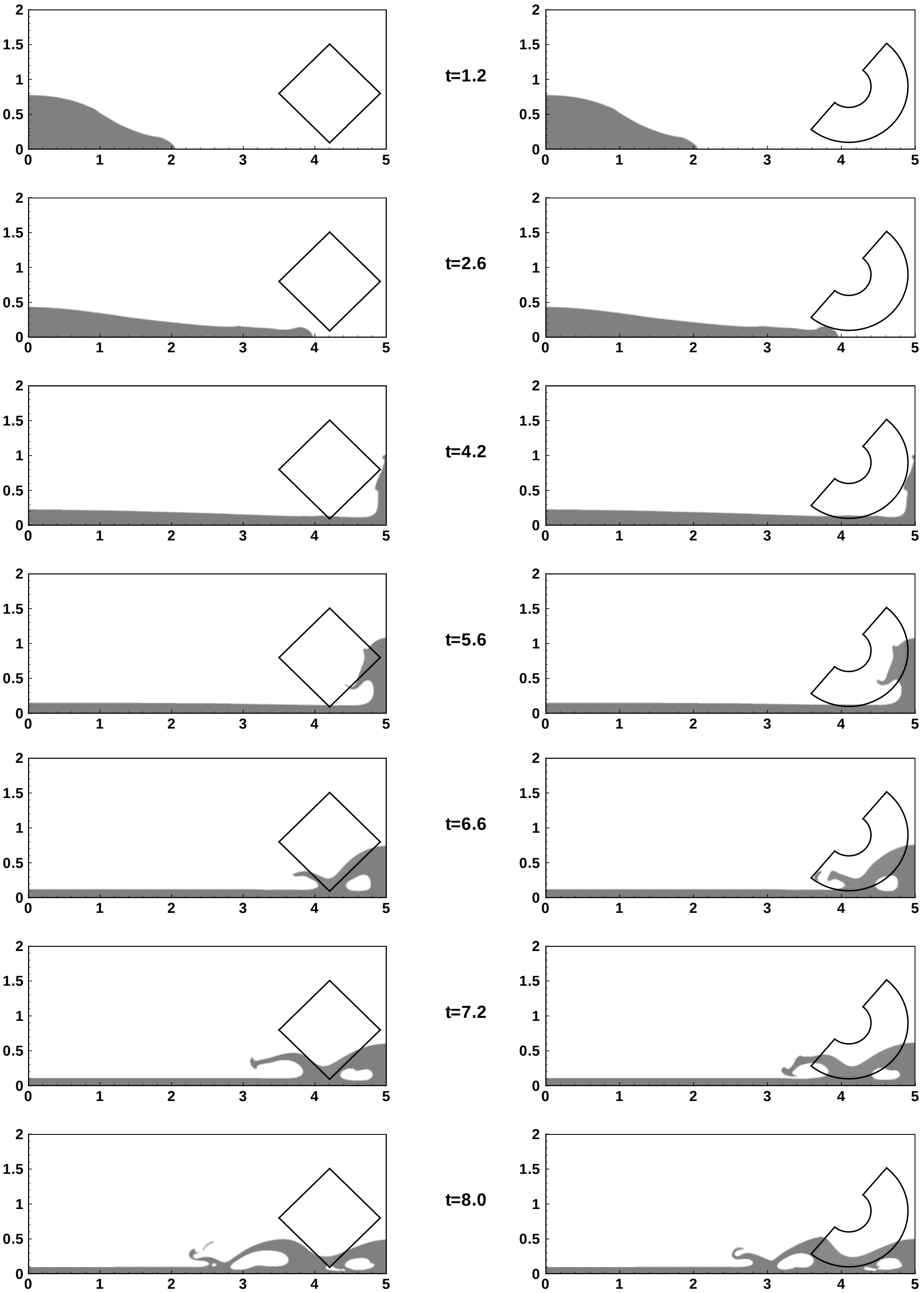

Figure 4.14. Dam-breaking with two different embedding grids

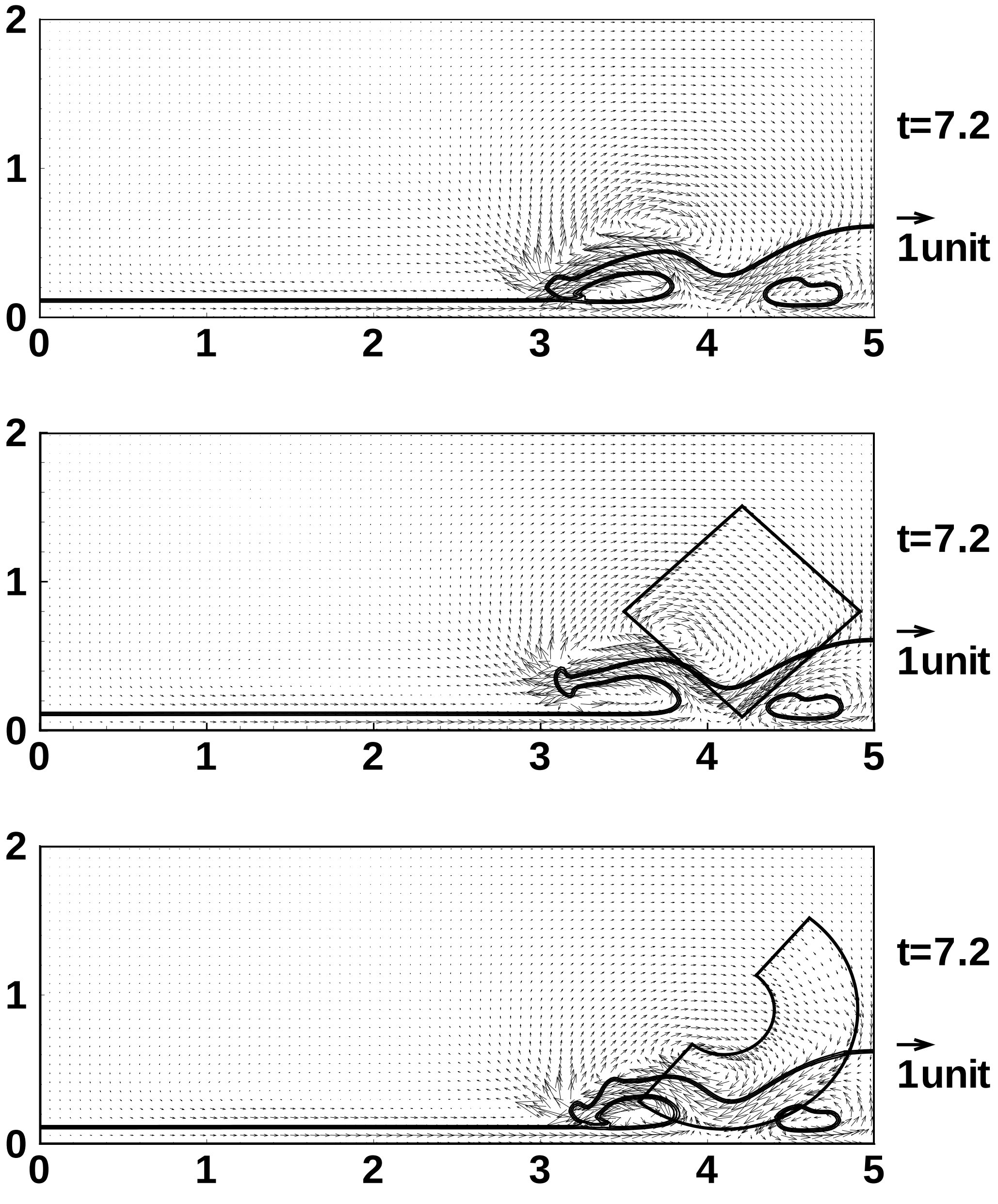

Figure 4.15. Velocity comparison for three different grids

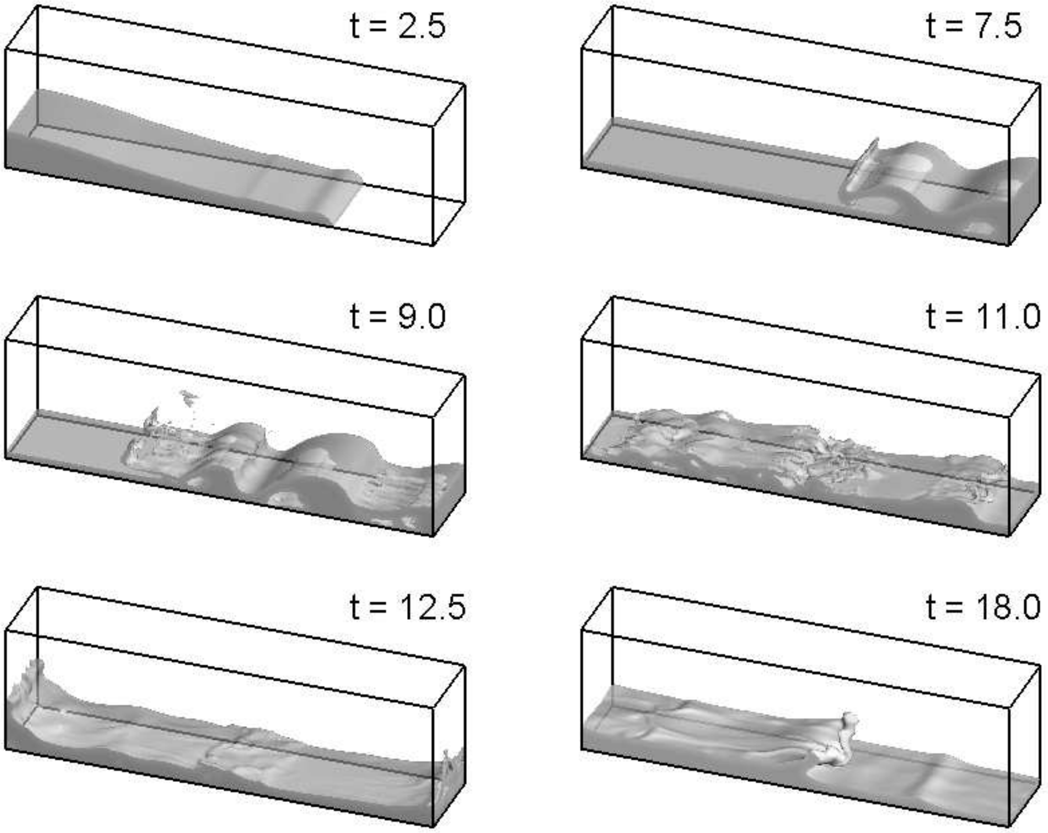

Figure 4.16. Free surface profiles for 3D dam breaking

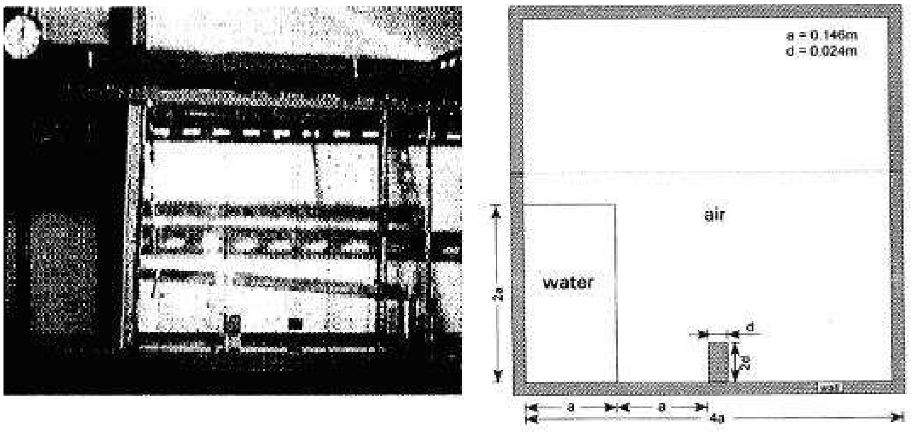

Figure 4.17. Experiment setup of dam-breaking with an obstacle

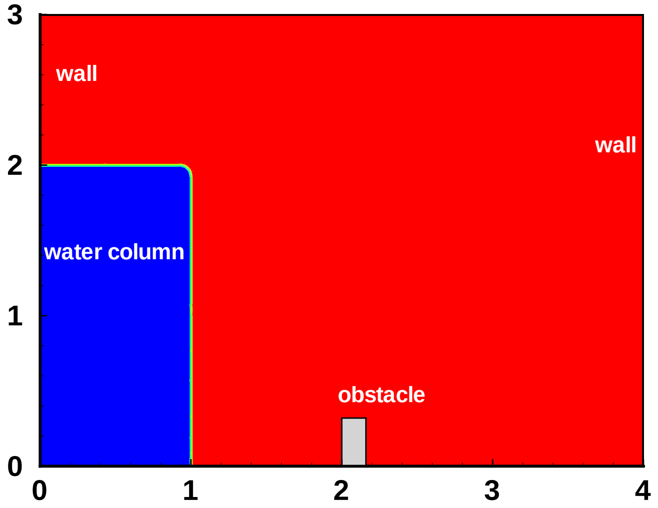

Figure 4.18. Numerical model of dam-breaking with an obstacle

4.7. Dam Breaking with an Obstacle

A more interesting test case of collapsing water column occurs when a small obstacle is placed downstream of the propagating water front. The test geometry used in the experimental investigation of Koshizuka et al. (1995) is illustrated in Figure 4.17. The height and width of the still water column are $2a$ and a (i.e., $0.292\text{m} \times 0.146\text{m}$), respectively. The width of the tank is $4a$ $(= 0.584\text{m})$ and the obstacle is located on the bottom wall at a distance of $2a$ $(= 0.292\text{m})$ from the left wall. The size of the obstacle is $2d \times d$ $(0.048\text{m} \times 0.024\text{m})$. In the present study, we choose $a = 0.146\text{m}$ as the characteristic length. The computational domain after normalization is shown in Figure 4.18.

Figure 4.19 shows a comparison between the experimental data and simulation results. At $t = 0$, the barrier holding the still water column was suddenly removed. The

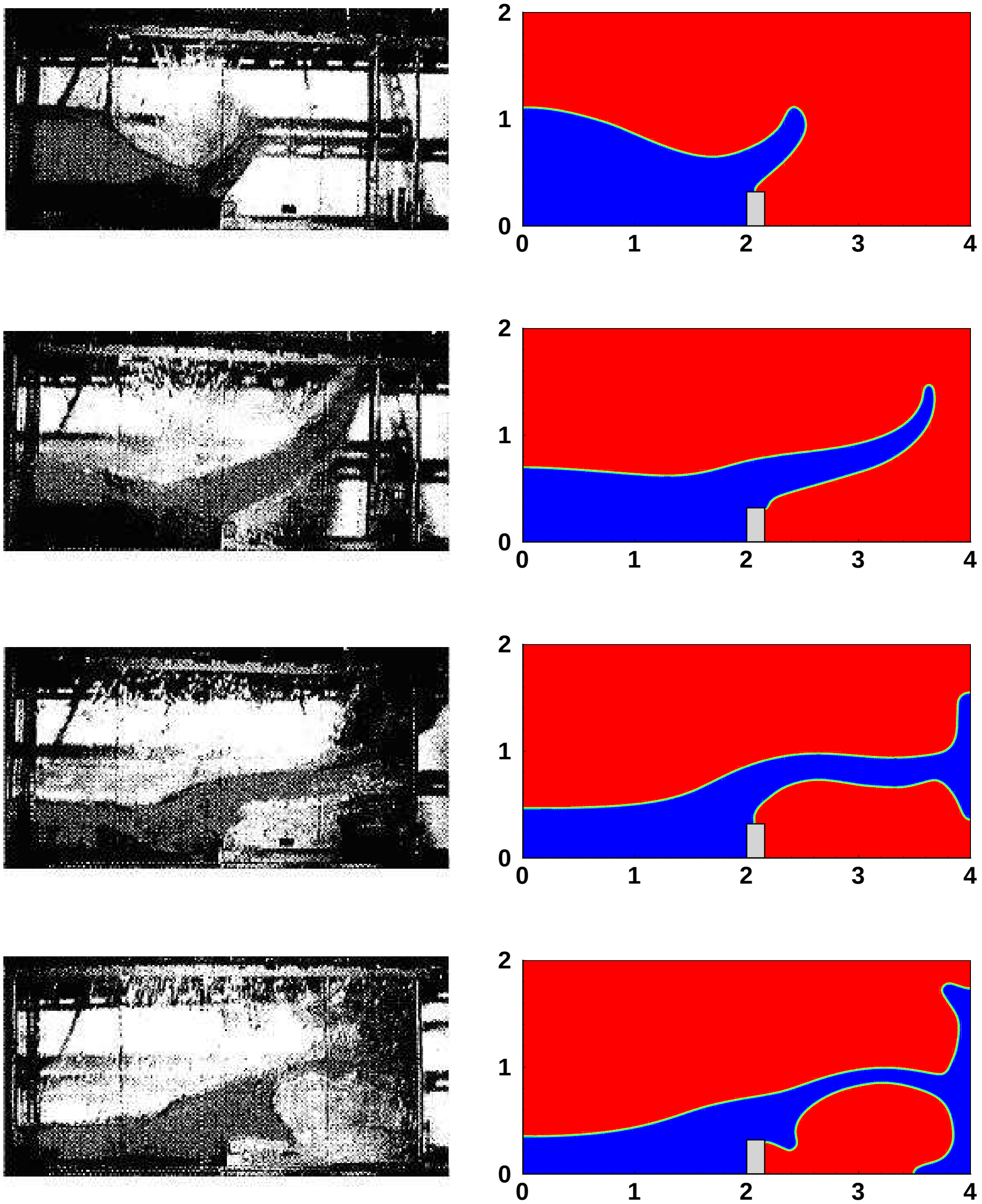

Figure 4.19. Free surface comparison

collapsed water column crashes upon the obstacle and produced a free jet with strong upward flow velocity. The jet continues to move to the right and eventually impinges on the vertical wall on the right hand side of the tank. As the water moves towards the right side of the tank, the jet trajectory becomes considerably flatter due to the gradual decrease of the upward jet velocity under its own weight. After impingement against the vertical wall, the jet is split into two streams moving vertically upward and downward along the tank wall. As the water level drops on the left hand side of the tank, the fluid momentum reduces gradually and the jet trajectory was deflated further downward under the gravitational force. In general, the numerical results are in close agreement with the corresponding experimental data of Koshizuka et al. (1995). This test case clearly illustrated the capability of the level set method in capturing violent free surface motions encountered in dam breaking problems. The same method can also be used for the simulation of vigorous sloshing in tanks and slamming of bodies onto liquid surface.

4.8. Free Jet Simulation

In this test case, we consider a water jet enters horizontally from the left hand side of the computational domain on top of the platform at a constant velocity of 1.0. The dimension of the platform is 2.0×1.0, and the height of the water jet is 0.5 as shown in Figure 4.20. This is similar to a water fall caused by a sudden drop of the streambed elevation in a river. During the initial stage of the simulation, the water jet experiences a free fall under the action of the gravitational force. As the jet impinges on the tank bottom, it spreads across the tank in both directions and induces strong vortices along the front of the air-water interface. It should be noted that the horizontal velocity of the surge front is faster than the inlet velocity of the jet due to the conversion of potential energy into kinetic energy as the water flows into the tank. After the split water jets reach the tank walls, they continue to climb up against the vertical wall by converting the fluid kinetic energy back into potential energy. It is interesting to note that the water runup on the right tank wall is considerably higher than the water level at the jet inlet during the initial stage of the simulation. This is clearly due to the combined effects of the horizontal and vertical momentums and energy while the jet was deflected upward against the vertical tank wall. As the water level continues to rise inside the tank, however, the water level on the right tank wall begins to drop since a significant part of the energy is dissipated due to strong turbulent eddy motions resulted from water splash in the pool.

Calculations were also performed for a 3D free jet problem as shown in Figure 4.21. The dimension of the tank is $1.5 \times 6 \times 3.6$ while the platform size is $1.5 \times 1 \times 2$. The height of the water jet is 0.5 and the inlet velocity is 1.0. It is seen that the free jet quickly becomes three-dimensional after impinging on the tank bottom. Comparing to the 2D simulations shown earlier in Figure 4.20, the flow is strongly three-dimensional with numerous air bubbles trapped beneath the free surface when the free jet collides with the siding water in the pool.

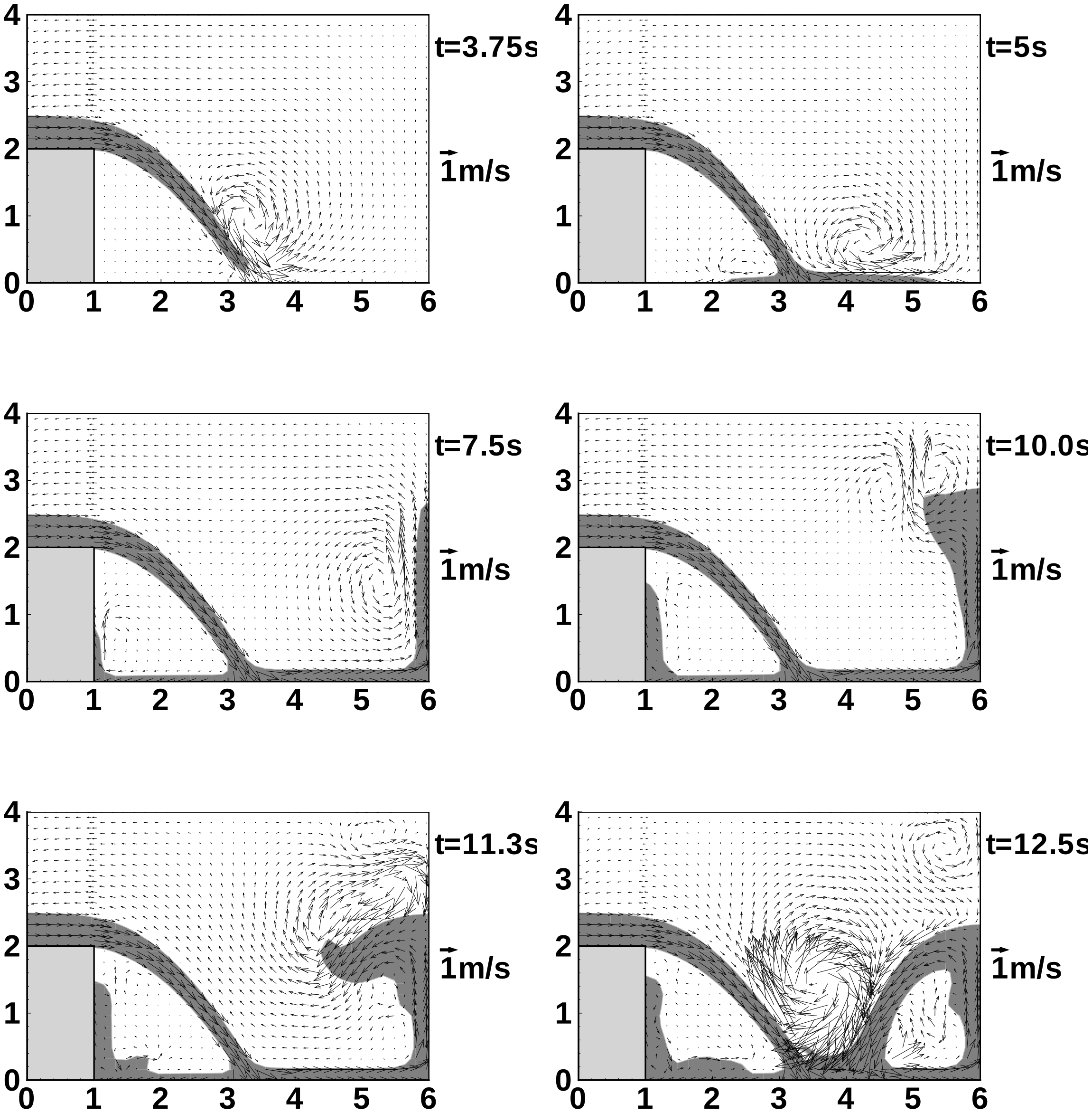

Figure 4.20. Free surface profiles and velocities, 2D free jet

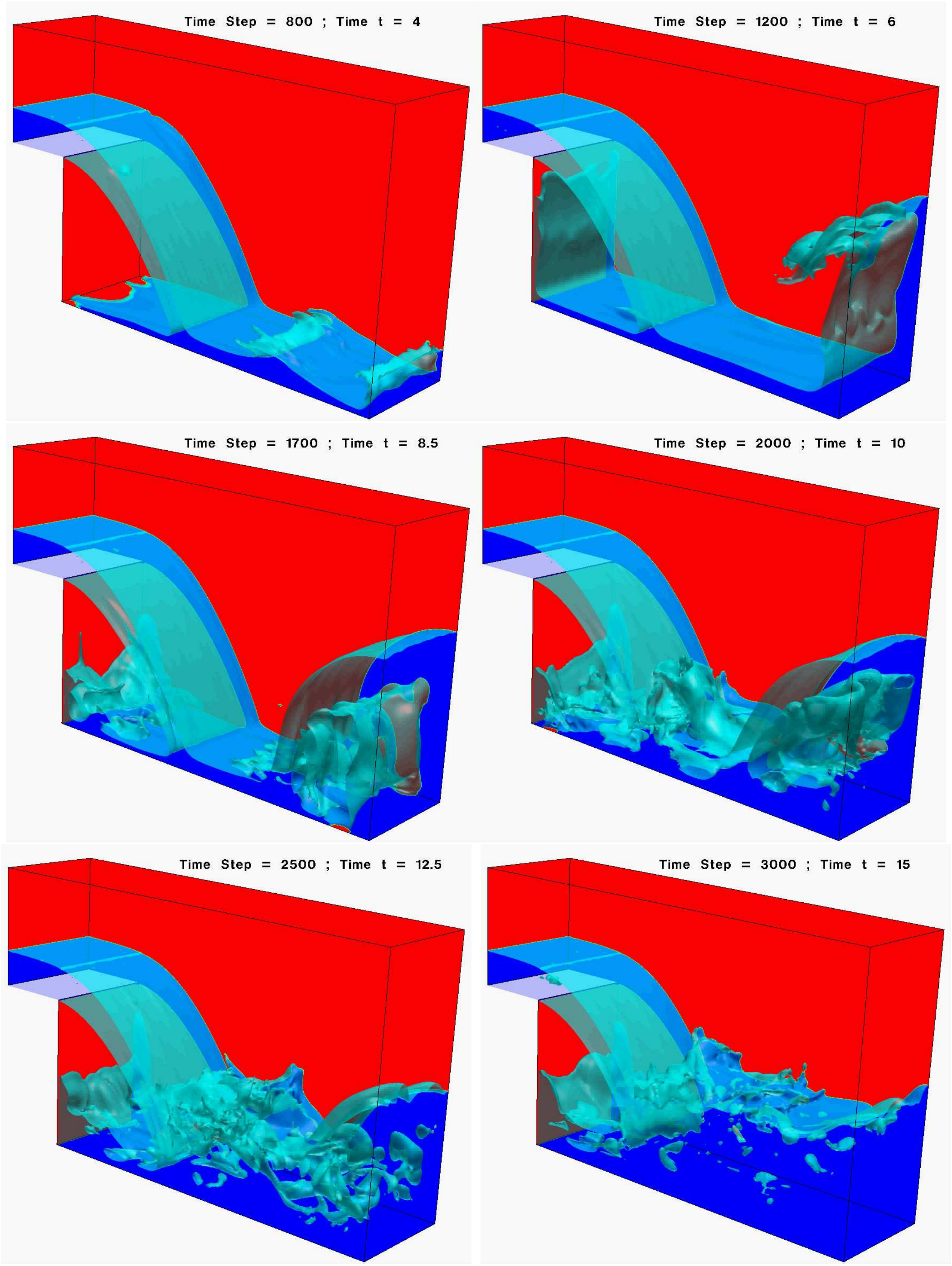

Time Step = 800 ; Time t = 4

Time Step = 1200 ; Time t = 6

Time Step = 1700 ; Time t = 8.5

Time Step = 2000 ; Time t = 10

Time Step = 2500 ; Time t = 12.5

Time Step = 3000 ; Time t = 15

Figure 4.21. Free surface profiles, 3D free jet

CHAPTER V

SLOSHING SIMULATIONS

5.1. Introduction

Due to the growing LNG market, there is a strong demand of new LNG carriers with significantly larger cargo capacity. The safety of the new LNG liquid cargo hold and containment system for the membrane-type LNG carriers with a wide range of filling levels has to be re-evaluated. Sloshing model tests have been performed by, among others, Faltinsen et al. (2000), Lee et al. (2005b), Hwang (2006), Lee et al. (2006a) and Lee et al. (2006b) to simulate six degrees of freedom ship motions and determine the critical sloshing load. In these experiments, the Froude scaling law is adopted to scale down the geometry, tank motion, and gravitational effects. Impact pressures obtained from the model tests are then scaled up to prototype using the Euler scaling with the full-scale pressure proportional to the liquid density and length dimensions. The model test is considered to be the most reliable method in predicting the maximum impact pressure especially for violent sloshing. However, the true impact load in the full scale LNG tank is still unknown due to the scale effects associated with other unmatched parameters such as fluid viscosity, gas/liquid density ratio, gas compressibility, ullage pressure, and wall elasticity.

Numerical simulations have also been used extensively for the simulation of sloshing flow in LNG tank. Considering the sloshing flows as free surfaces flows, there are two major approaches, namely interface-tracking and interface-capturing methods, to find the shape of the free surface. Because of complexity of the free surface phenomena in sloshing, the interface-capturing method is more often used for sloshing flow simulations. The interface-capturing method can be categorized into three different approaches, Marker and Cell (MAC), Volume of Fluid (VOF) and Level Set Method. The smoothed particle hydrodynamics (SPH) method which is developed from MAC is used by Iglesias et al. (2004) and Nam and Kim (2006) for simulating violent sloshing flows in two-dimensional tanks. Kim (2001, 2004) used the SOLA-SURF to solve the sloshing problem in rectangular and prismatic tanks. Lee et al. (2005a) employed a commercial code FLOW3D with VOF method for the free surface flow simulation for parametric sensitivity study on LNG tank sloshing load. Loots et al. (2004) presented an improved VOF (iVOF) method to account for mass conservation in cut cells and eliminate numerical spikes in pressure signals for sloshing tank simulation. Wemmenhove et al. (2005) extended iVOF to incorporate two-phase flow model for more accurate simulation of LNG tank sloshing. Rhee (2004) used FLUENT commercial code for the simulation of a generic membrane type LNG carrier tank with a simplified pump tower. In addition to viscous flow methods, potential flow finite element method has also been employed by Kim et al. (2002, 2003) for the simulation of sloshing impact pressure in LNG tank.

In the present study, the level set method has been incorporated into the chimera RANS method of Chen and Chen (1998) for the prediction of sloshing impact load on membrane-type LNG tanks. The governing equations are formulated in curvilinear coordinate system and discretized using the finite-analytic method of Chen et al. (1990) on a non-staggered grid. For the additional level set equations of evolution and re-initialization, we use the 3rd-order TVD (total variation diminishing) Runge-Kutta scheme (Yue et al., 2003) for time derivative, and the 3rd-order ENO (essentially non-oscillatory) scheme for spatial derivatives. The present interface-capturing method was validated in earlier in Chen and Yu (2006) for several benchmark cases including a stationary circle, the Zalesak's problem, and the stretching of a circular fluid element under prescribed free motion. The level set method was then incorporated into the chimera RANS method of Chen and Chen (1998) for complex free surface flow simulations. Calculations were performed for both the two-dimensional and three-dimensional membrane-type LNG tank under prescribed transverse and longitudinal sloshing motions. The simulation results clearly demonstrated the capability of the level-set FANS method for accurate prediction of violent free surface flows and the associated impact load induced by the sloshing motion of LNG tanks.

5.2. Geometry and Motions

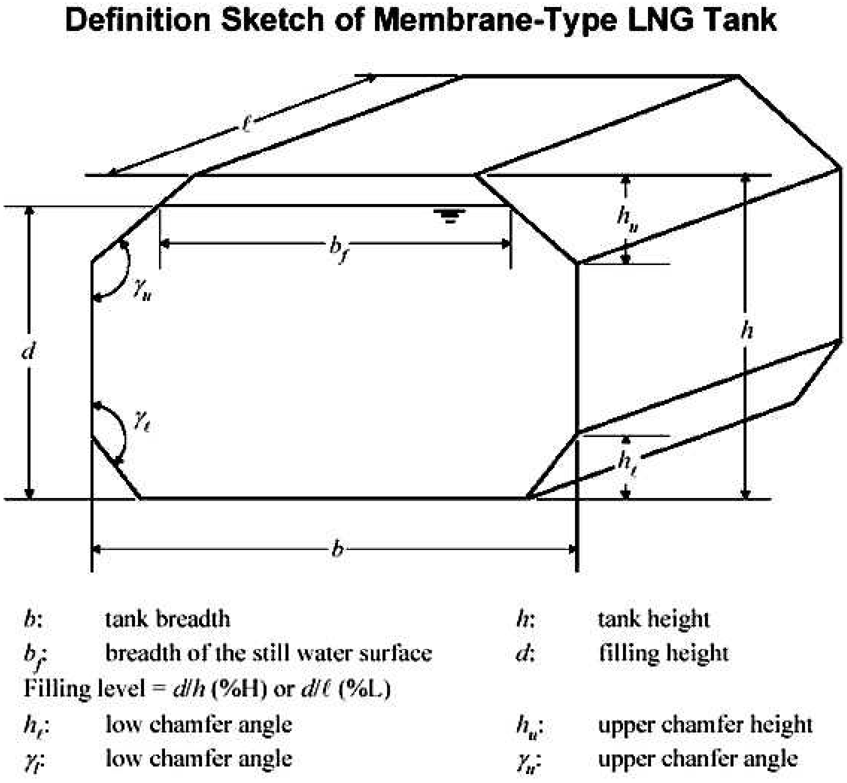

Figure 5.1. Membrane-type LNG tank geometry

Figure 5.1 shows the geometry of the LNG tank used in the present simulations. The dimension of the tank in full scale is 37.9m × 43.72m × 26.75m, (tank breadth) ×

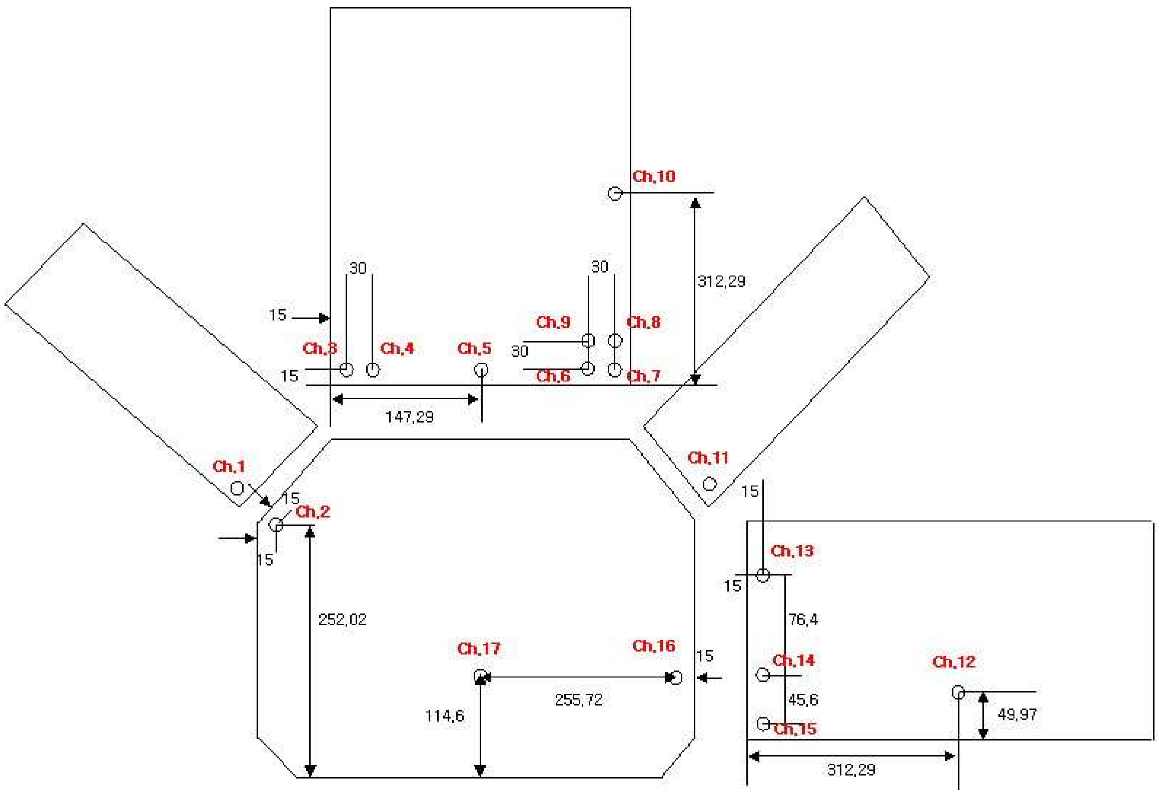

Figure 5.2. Sensor positions on LNG model tank

(tank length) × (tank height). The lower and upper chamfer angles (γ_l, γ_u) are both equal to 135^0. The lower chamfer height h_l is 3.77m, while the upper chamfer height h_u is 8.63m. For all the computations, the filling level is specified in terms of d/h ($\%H$).

Model tests were conducted by Lee et al. (2006b) on a 1/70 scale model with dimensions of 541.36mm × 624.50mm × 382.20mm. The model was instrumented with 17 pressure gages to measure the impact pressure on the LNG tank walls. Figure 5.2 shows the positions of all 17 sensors in the model test. The numbers in this figure are the distances in model scale. The sampling frequency of the pressure gages is about 20,000 Hz.

In the present study, we consider both the transverse and longitudinal sloshing modes with various combinations of horizontal, vertical and rotational motions. The

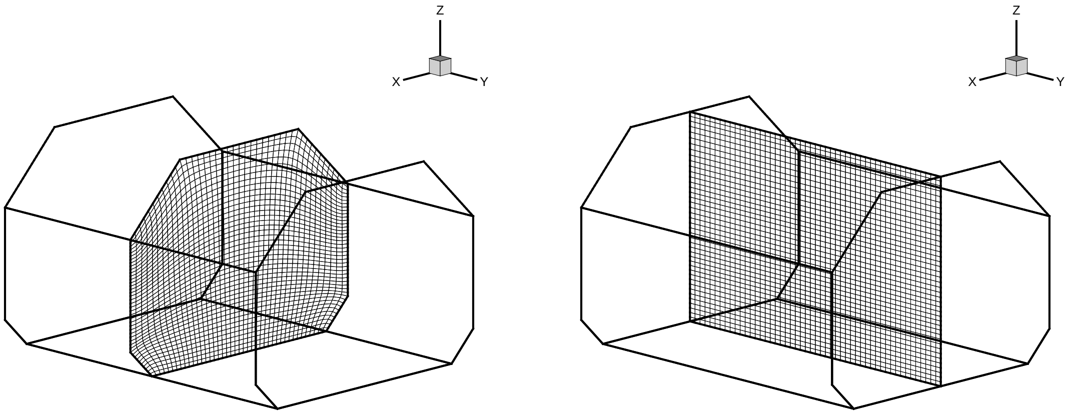

Figure 5.3. 2D grids for transverse and longitudinal motions

transverse motion is in the xz-plane while the longitudinal motion is in the yz-plane as shown in Figure 5.3. The horizontal direction is along the x-axis for transverse motion, and along y-axis for longitudinal motion. Table 5.1 and Table 5.2 show the full scale motion parameters for the three transverse (Cases 1-3) and three longitudinal (Cases 4-6) motion cases considered in the present study. The horizontal, vertical, and rotational motions are defined as follows:

$$\text{Motion(t)} = \text{Amplitude} \cdot \sin(\frac{2 \cdot \pi}{\text{Period}} + \text{Phase})$$

Note that the positive values in Table 5.2 represent motions from left to right, bottom to top, and counterclockwise rotation.

A 1/70 scale model tank was used in the experiments. The tank motion parameters were scaled down based on the Froude scaling law, while the measured impact pressures were scaled up based on the Euler scaling law. The characteristic time and pressure are given by

$$\text{Time} = \sqrt{\text{Length}/\text{Gravity}}$$

$$\text{Pressure} = \text{Density} \times \text{Gravity} \times \text{Length}$$

Table 5.1. LNG tank motion periods

case	FLVL($H\%$)	Direction	Period(s)
1	16.3	Transverse	1.05E+01
2	30	Transverse	9.67E+00
3	50	Transverse	8.98E+00
4	50	Longitudinal	8.37E+00
5	80	Longitudinal	7.17E+00
6	92.5	Longitudinal	9.08E+00

Table 5.2. LNG tank motion amplitudes

case	Horizontal Motion		Vertical Motion		Rotational Motion	
	Amp.(m)	Phase(rad)	Amp.(m)	Phase(rad)	Amp.(m)	Phase(rad)
1	4.75E+00	3.13E+00	9.13E+00	-2.09E+00	1.90E-02	0.00E+00
2	4.05E+00	-2.96E+00	7.78E+00	-2.18E+00	6.00E-03	0.00E+00
3	3.38E+00	-2.14E-01	5.89E+00	3.07E-01	2.48E-03	0.00E+00
4	3.66E-01	-1.89E+00	4.51E+00	-4.12E-01	8.37E-02	0.00E+00
5	5.84E-01	-4.47E+00	1.72E+00	-1.89E+00	1.21E-02	0.00E+00
6	1.81E-01	-1.26E+00	6.80E+00	-4.95E-01	9.52E-02	0.00E+00

Therefore, the horizontal and vertical motion amplitudes in model scale are 1/70 of the corresponding full scale values, while the motion period is scaled down by . The measured impact pressures reported in the experimental study were scaled up by 70 times.

5.3. Time Step Size and Grid Refinement

Numerical simulations were performed using the level-set RANS code for all six cases listed in Table 5.1 and Table 5.2. Both the air and water flows were assumed to be incompressible, and the surface tension was ignored in the present simulations. The reference pressure was specified as the atmospheric pressure at the air-water interface along the vertical axis passing through the geometric center of the LNG tank. In the following, we will present both 2D and 3D simulation results to illustrate the general performance of the present numerical method.

In order to determine the influence of time step size and grid spacing on the predicted impact pressure, two-dimensional numerical simulations were performed for Case 3 (transverse motion at 50% filling level) using three different time increments and two different grid sizes. Figure 5.4 shows the two-dimensional simulation results with a $85 \times 3 \times 85$ grid and three different time increments of $\tau = 0.01T, 0.002T$, and $0.001T$, where T is the motion period. It is seen that the predicted pressure histories are nearly identical for all three time increments, but the predicted peak impact pressures are somewhat sharper for the $\tau = 0.001$ case. To ensure accurate resolution of the short duration impact pressure forces, all 2D and 3D simulations were performed using 1,000 time steps per period (i.e.,$\tau = 0.001$).

A grid refinement study was also performed by doubling the grid points in the transverse cross sections from $85 \times 3 \times 85$ to $169 \times 3 \times 169$. For the coarse grid

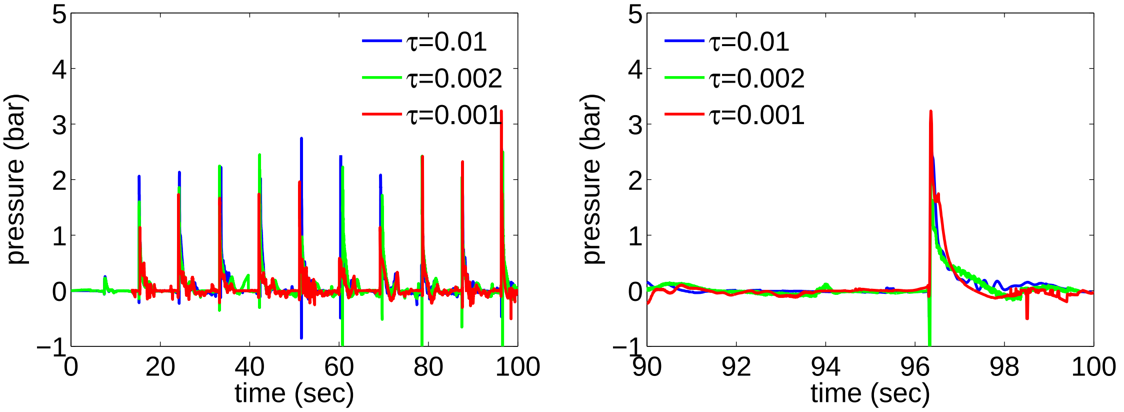

Figure 5.4. Influence of time increment, Ch.11 in Case 3

case, the cell sizes in x-, y-, and z-directions are approximately (0.45 m, 0.43 m, 0.32 m) in full-scale, and (6.4 mm, 6.2 mm, 4.5 mm) in the model-scale tank. The grid sizes are reduced to 1/2 in all three directions for the fine grid case. Figure 5.5 shows a comparison of the coarse ($85 \times 3 \times 85$) and fine ($169 \times 3 \times 169$) grid results over 10 periods. It is quite clear that the coarse and fine grid simulations predicted about the same level of impact pressures, although the peak pressures obtained by fine grid simulations are somewhat higher at certain instants. For optimal usage of the available computer resource, all 2D and 3D simulations presented in this report were performed using $85 \times 3 \times 85$ and $85 \times 101 \times 85$ grid points, respectively.

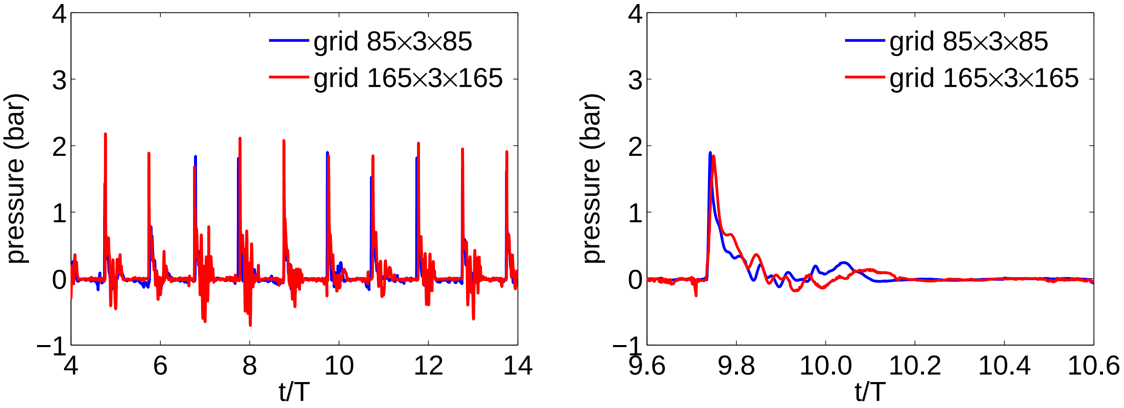

Figure 5.5. Grid refinement study, Ch.11 in Case 3

5.4. Scale Effects

As noted earlier, the impact pressure reported in Lee et al. (2006b) were measured in a 1/70 scale model tank based on Froude scaling law, and scaled up to full scale using the Euler scaling law. According to the Froude scaling law, the Reynolds number in the model test is $(1/70)^{1.5} = 0.01707$ times of that of the prototype. In order to ascertain the scale effects, simulations were performed at both the full-scale and model-scale Reynolds numbers for Case 3 using the same $85 \times 3 \times 85$ numerical grid and the same dimensionless time increment $\tau = 0.001$. To facilitate a direct comparison of the simulation results, the impact pressures obtained for the model-scale tank were scaled up by 70 times based on the Euler scaling law. It is seen from Figure 5.6 that the peak impact pressures observed in the model-scale tank are comparable to those obtained at the full-scale flow condition. For convenience, all simulations reported in the following sections were performed for the prototype LNG tank using the full-scale and motion amplitudes and motion periods.

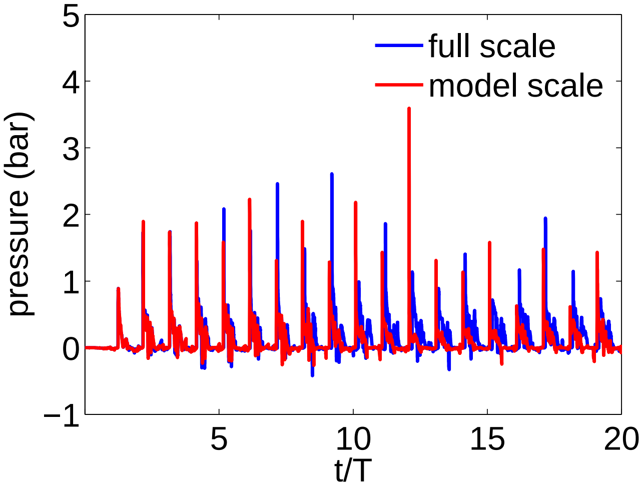

Figure 5.6. Scale effects, Ch.11 in Case 3

5.5. Results and Discussions

Both 2D and 3D full-scale simulations were performed for all six cases listed in Table 5.1 and Table 5.2 using a constant time increment of $0.001T$ (1,000 time steps per period) to provide accurate resolution of the peak impact pressures. For two-dimensional simulations, a one-block grid with $85 \times 3 \times 85$ nodes was used for the transverse motion cases (Cases 1-3), while a $3 \times 101 \times 85$ rectangular grid was used for longitudinal motion cases (Cases 4-6). All 2D simulations were performed for 20 periods and the wall pressures at selected sensor locations shown in Figure 5.7 were recorded every time step to facilitate a direct comparison with the experimental data of Lee et al. (2006b). The total CPU time for 20 periods (20,000 time steps) is about 3 hours on a single-processor Dell Optiplex GX620 computer with 3.2 GHz CPU and 3.5 GB of RAM.

All three-dimensional simulations were performed using a one-block grid with $85 \times 101 \times 85$ nodes. The grid size for 3D simulations was adjusted near the top wall for high filling ratio longitudinal motion cases to ensure appropriate resolution of the high velocity and pressure gradient regions. A Large Eddy Simulation (LES) approach was employed in conjunction with Smagorinsky subgrid scale model to provide appropriate

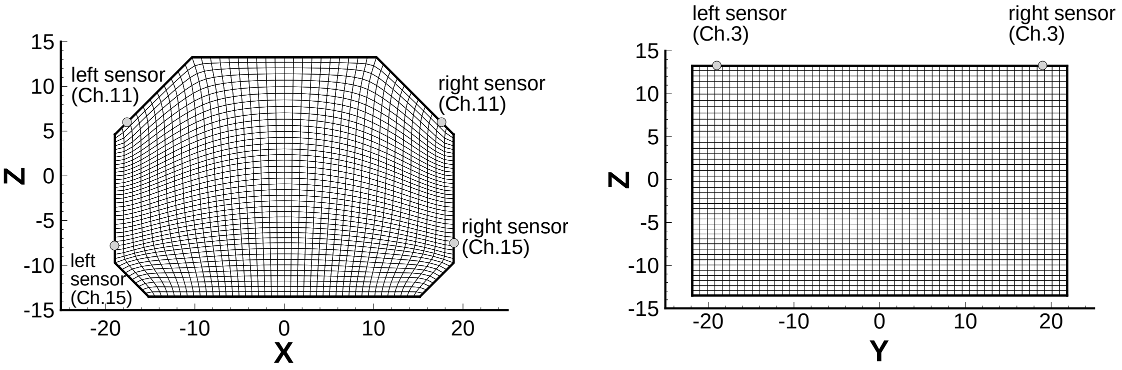

Figure 5.7. Grid and sensor locations for 2D simulations

resolution of the flow turbulence induced by violent free surface motions. The three-dimensional simulations were performed initially for 20 periods and the wall pressures at selected sensor locations were recorded every time step. The 3D velocity and pressure fields for the entire tank were also saved every 50 time steps to provide more detailed descriptions of the complex three-dimensional flow induced by the sloshing tank. The total CPU time for 20 periods (20,000 time steps) is about 120 hours for 3D simulations on a single-processor Dell Optiplex GX620 computer with 3.2 GHz CPU and 3.5 GB of RAM.

A detailed examination of the 3D simulation results indicated that the sloshing flow is highly three-dimensional even though the prescribed transverse or longitudinal motions are strictly two-dimensional. Due to the three-dimensional instability, the impact pressures at the mirror image locations on opposite walls were found to be drastically different under certain flow conditions. Since the wall pressures were recorded only at a small number of sensor locations for the first 20 periods of the present 3D simulations, it was not possible to quantify the three-dimensional effects. In order to provide a more detailed understanding of the violent three-dimensional free surface flows, all 3D simulations were continued for three additional periods to obtain the impact pressure histories at 48 different locations as shown in Figure 5.8. These 48 sensor locations include not only the original 17 pressure sensors in the model tank, but also their mirror images in both x and y directions. This enables us to capture the most critical impact pressures which may occur on the opposite walls of any given pressure sensor locations in the model tank. It should be remarked also that the impact pressure on tank walls is highly localized with significant variations between two adjacent grid points. Therefore, the highest impact pressure may not occur precisely at the sensor locations unless long-duration simulations are performed for several thousand periods to capture the true peak pressure. In view of this, we have

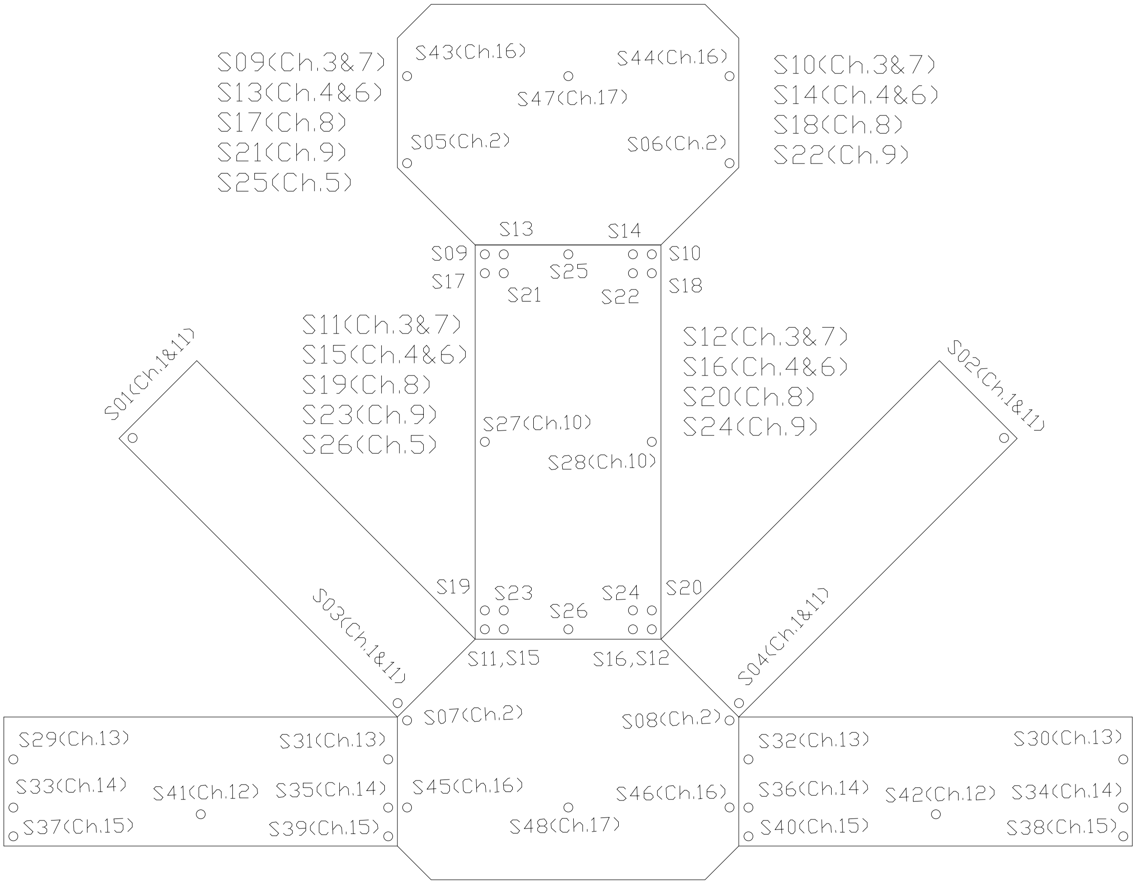

Figure 5.8. Grid and sensor locations for 3D simulations

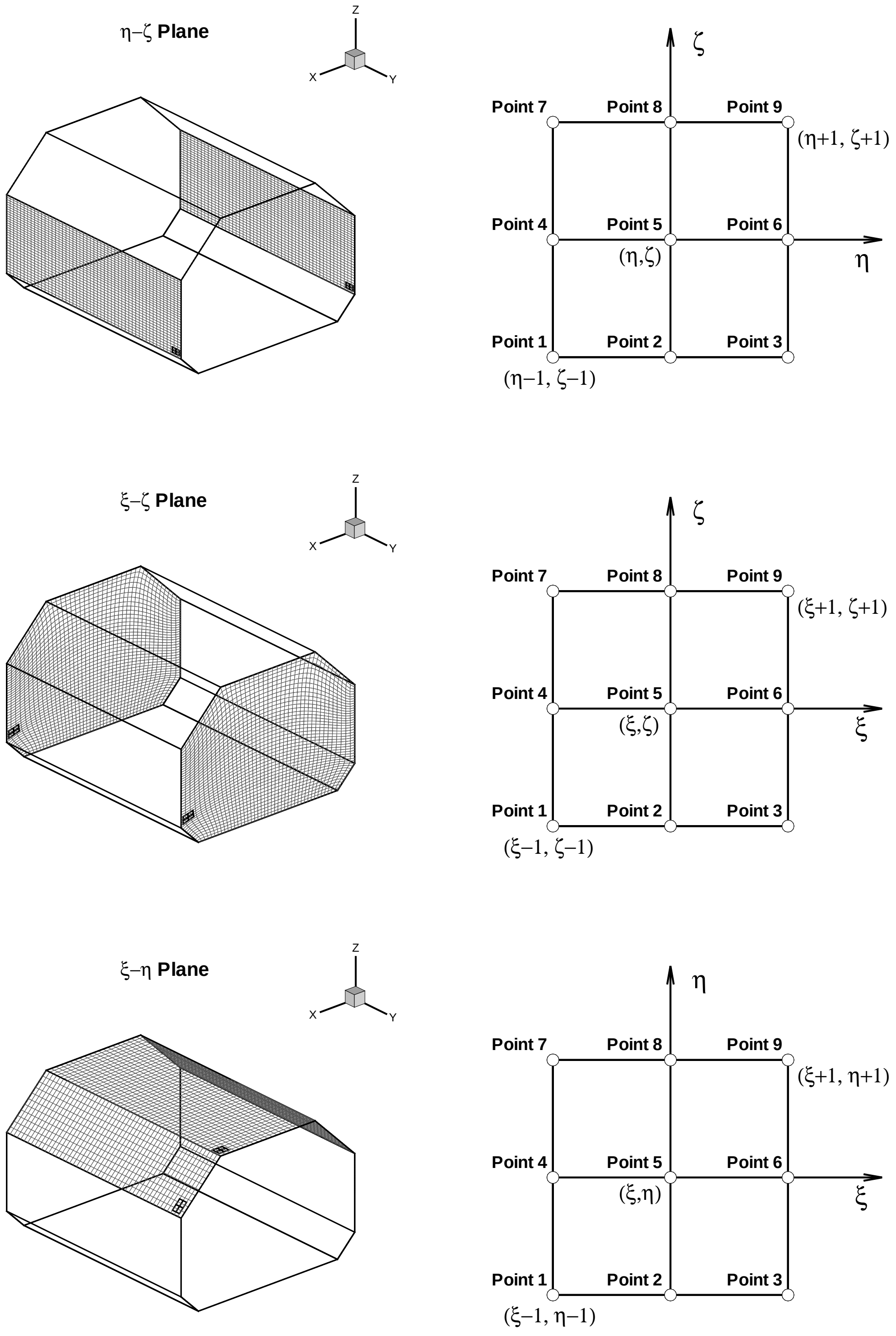

Figure 5.9. Nine-point stencils around pressure sensor

recorded the impact pressures on a 3 × 3 grid around each sensor location as shown in Figure 5.9, where (ξ,η,ζ) represent the grid indices of the curvilinear coordinate system and the center node (i.e., Point 5) is closest to the actual pressure sensor location in the model tank. This enables us to determine the local maximum impact pressure in the vicinity of each pressure sensor. For the sake of brevity, the predicted pressure history at Point 5 will be used for comparison with the corresponding pressure measurements in the following sections.

5.5.1. Case 1 - Transverse & 16.3% FLVL

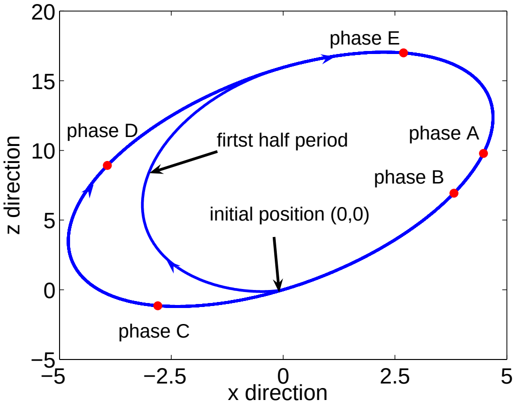

Figure 5.10. Tank motion trajectory, Case 1

Figure 5.10 shows the transverse motion trajectory of the LNG tank for Case 1 with the initial tank position at the origin (0,0). The trajectory of the prescribed tank motion is elliptic and asymmetrical with respect to the x and z axes because of different phase shifts and motion amplitudes in the horizontal and vertical directions. The tank experiences a small amplitude roll motion with a maximum roll angle of ±1.09° .

Figure 5.11 shows the 2D simulation results of impact pressures for both the left

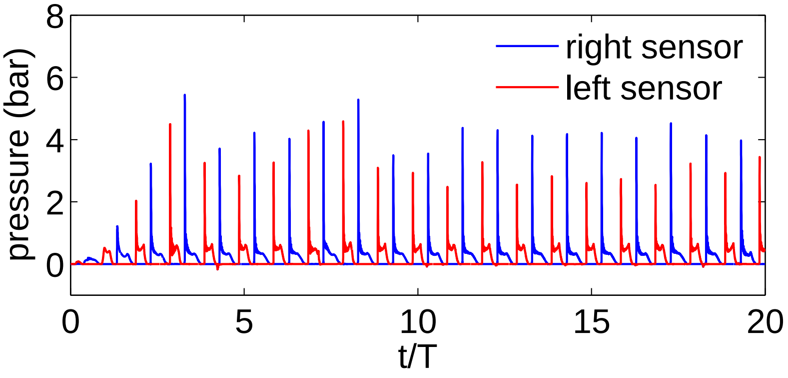

Figure 5.11. 2D pressure history, Ch.15, Case 1

and right pressure sensors corresponding to Ch.15 as shown in Figure 5.7. It is seen that there is a half-period phase difference between the left and right sensor locations. Due to the asymmetric tank motion, the predicted pressure patterns are also quite different for the left and right sensors. It is interesting to note that the pressure at the right sensor location exhibits a distinct double-peak pattern, while a single-peak pattern is observed at the left sensor location.

Figures 5.12 and 5.13 show the comparisons of measured and predicted pressure

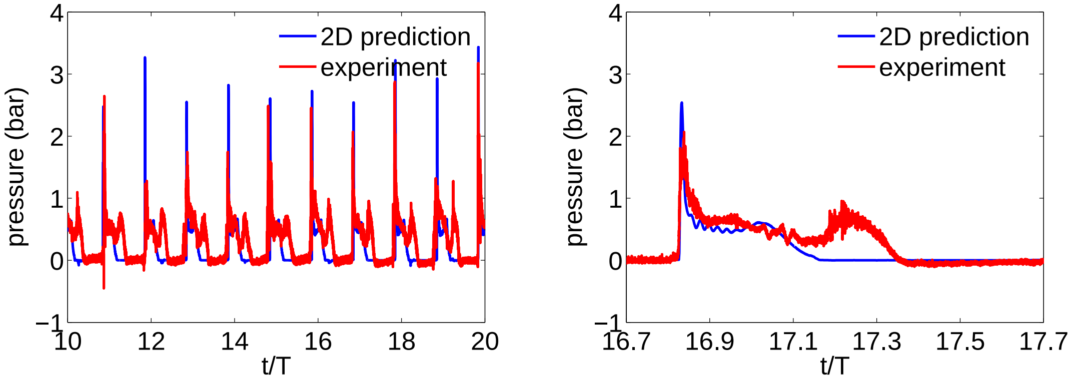

(a) 10 periods

(b) 1 period

Figure 5.12. 2D impact pressure, Ch.15 (right sensor), Case 1

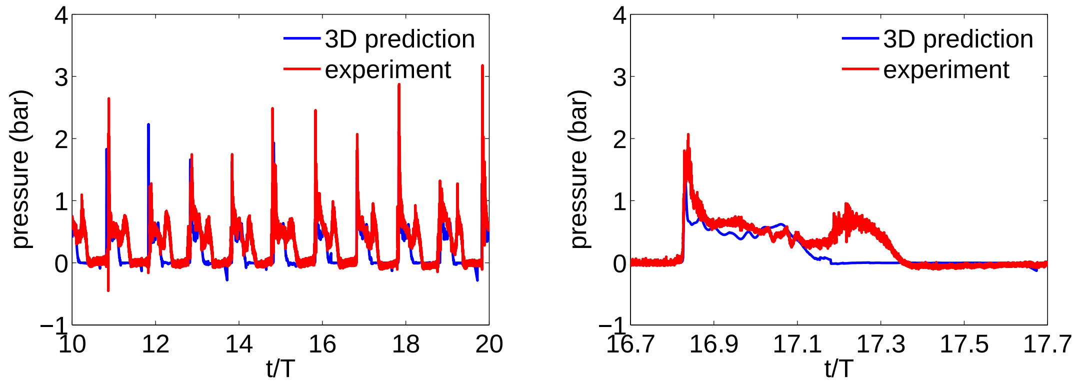

(a) 10 periods (b) 1 period

Figure 5.13. 3D impact pressure, Ch.15 (S40), Case 1

histories at Ch.15 over 10 periods for the 2D and 3D simulations, respectively. It is seen that the pressure rises sharply due to water impact on the tank wall and decays rapidly following the impact. However, the pressure did not return immediately to zero but exhibits a distinct double-peak pattern after the impact. In general, both the pressure pattern and peak pressure values are accurately predicted. It is also noted that the 3D simulation gives a somewhat lower peak pressure than the 2D case since the fluid impact is highly localized in the 3D tank and may not occur at the exact sensor location. The three-dimensional variations of the impact pressure in the vicinity of the Ch.15 pressure sensor can be clearly observed from Figure 5.14. A detailed examination of the pressure history over a single period shown in Figure 5.13(b) indicates that the peak impact pressure occurs between $t/T = 16.80$ and 16.85 over this specific period. In order to facilitate a more detailed understanding of the observed impact pressure pattern, it is desirable to examine the detailed velocity and pressure fields induced by the sloshing tank motions immediately before and after the peak impact corresponding to Phase A ($t/T = 16.80$) and Phase B ($t/T = 16.85$) in the motion trajectory shown in Figure 5.10. For completeness, the 2D and 3D flow and pressure fields will also be presented at three other times instants $t/T = 17.10, 17.35$ and 17.60 which are denoted by Phases C, D, and E in Figure 5.10. Note that Phases B, C, D, and E were chosen to be $T/4$ apart to illustrate the general flow patterns over one sloshing period.

Figure 5.15 shows the 2D free surface patterns, velocity vectors, and pressure contours at five time instants $t/T = 16.80, 16.85, 17.10, 17.35$ and 17.60, which are denoted by Phases A-E in the motion trajectory plot shown earlier in Figure 5.10. As noted earlier, the maximum impact pressure at Ch.15 (lower-right sensor) occurs between Phases A and B when the LNG tank is descending from the upper-right corner towards the lower-left corner along the elliptic motion trajectory. It is seen that the sloshing water moves rapidly from left to right between Phases A ($t/T = 16.80$) and B ($t/T = 16.85$) and produced a sudden impact on the right tank wall where Ch.15 is located. After the primary impact, the water continues to rush up the tank side wall. This leads to a double-peak pressure pattern since the pressure sensor No.15 is submerged under increasing water depth between Phases B and C when the LNG tank continues to move along the lower half of the elliptic motion trajectory towards

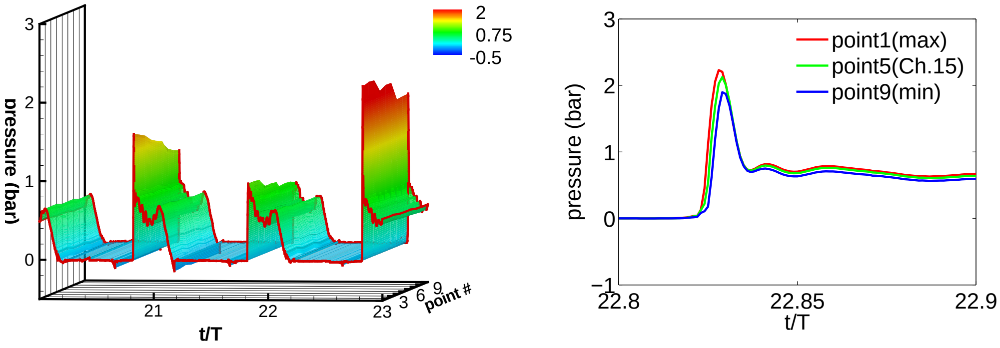

Figure 5.14. Impact pressures, the vicinity of Ch.15 (S40), Case 1

the lower-left corner. Between Phases C and D, the tank reaches the lower-left corner and begins to ascend along the upper half of the elliptic motion trajectory towards the upper-right corner. Due to the change of motion direction, the sloshing water is moving towards the left wall. At Phases D and E, the sloshing water was found to pile up on the tank left wall while the right wall is completely exposed in air with zero pressure reading on Ch.15. In the present two-phase flow approach, both the water and air flows were computed simultaneously as seen from the velocity vector plots in Figure 5.15. This enables us to capture the interaction between the sloshing fluid and the gas in ullage space of the sloshing tank.

Figure 5.16 shows the predicted three-dimensional free surface patterns and the corresponding pressure contours on tank walls for the same five phases shown in Figure 10. The sharp wave fronts induced by sloshing motion can be clearly seen at Phases A, C, and E. At Phase A, the tank right wall is completely exposed with zero pressure reading at Ch.15. Between Phases A and B, the sharp front of the sloshing water impinges directly on the right wall and produces a large impact pressure at Ch.15. It is seen that the impact pressure is strongly three-dimensional at Phase B even though the free surface pattern remains nearly two-dimensional. Since the impact pressure is highly localized and varies from one sloshing period to another, it is difficult to capture the true maximum impact pressure unless the numerical simulations can be performed for hundreds or thousands of sloshing periods. For short-duration simulations, it is desirable to record the maximum impact pressure over the entire tank wall since the peak pressure may not occur precisely at any specific sensor locations. This will provide a more reasonable prediction of the maximum impact pressure on the LNG tank walls. It should also be remarked that the three-dimensional sloshing motion tends to reduce the risk of tank damage since the maximum impact force is less likely to occur at the same location when comparing to purely two-dimensional impacts.

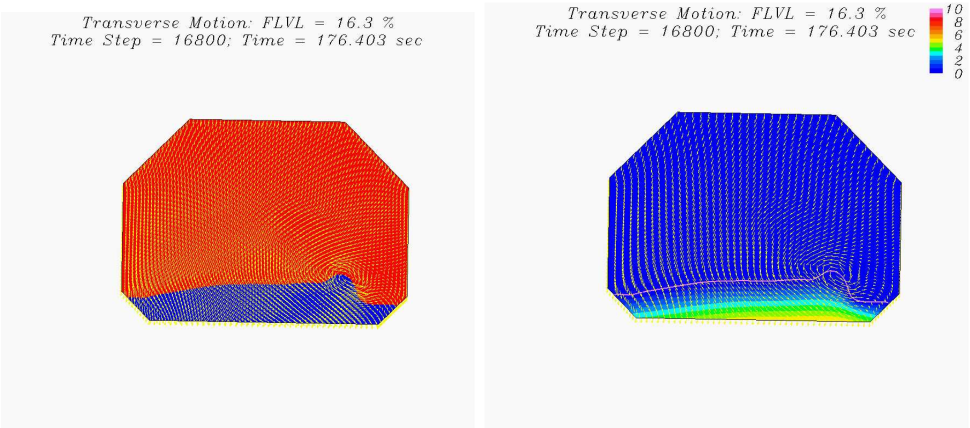

(a) Phase A: t/T = 16.80

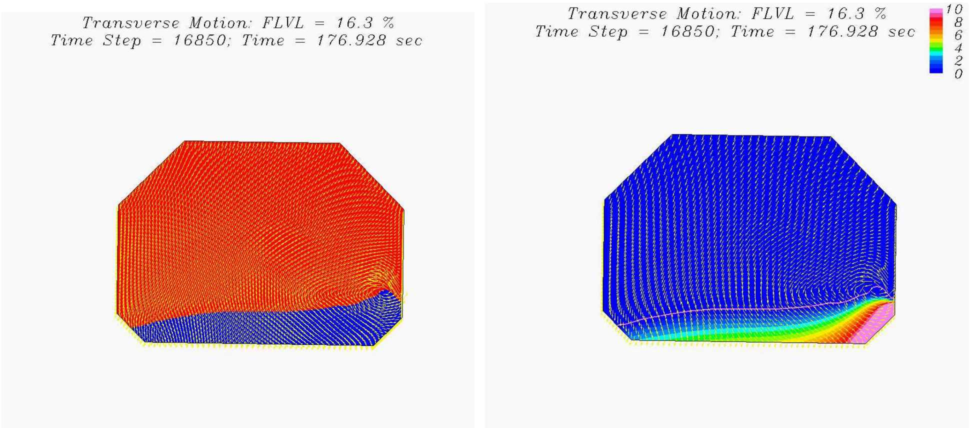

(b) Phase B: t/T = 16.85

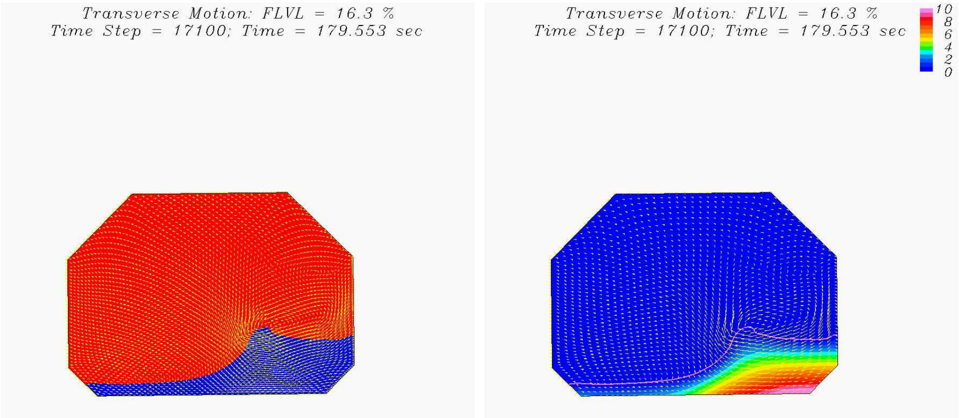

(c) Phase C: t/T = 17.10

Figure 5.15. 2D free surface, $\vec{V}, p$, Case 1

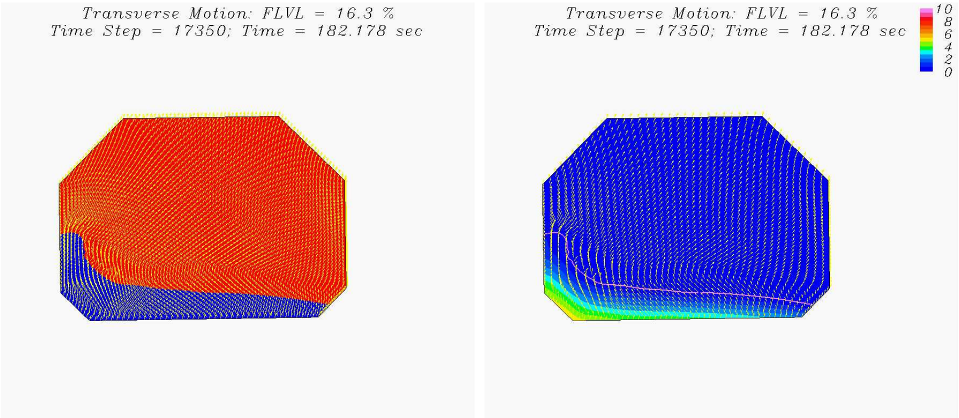

(d) Phase D: t/T = 17.35

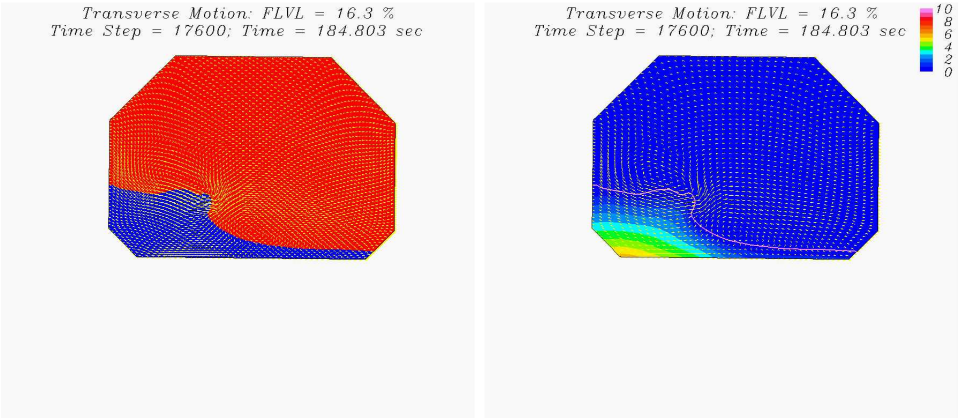

(e) Phase E: t/T = 17.60

Figure 5.15. (Continued)

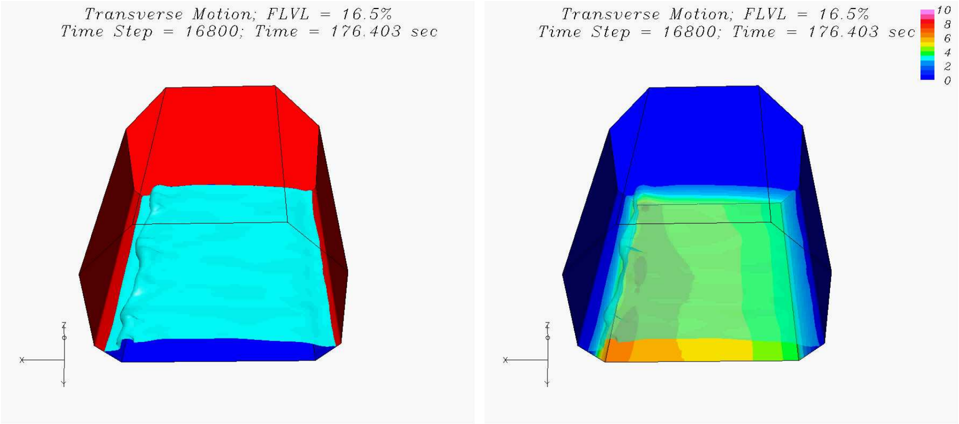

(a) Phase A: t/T = 16.80

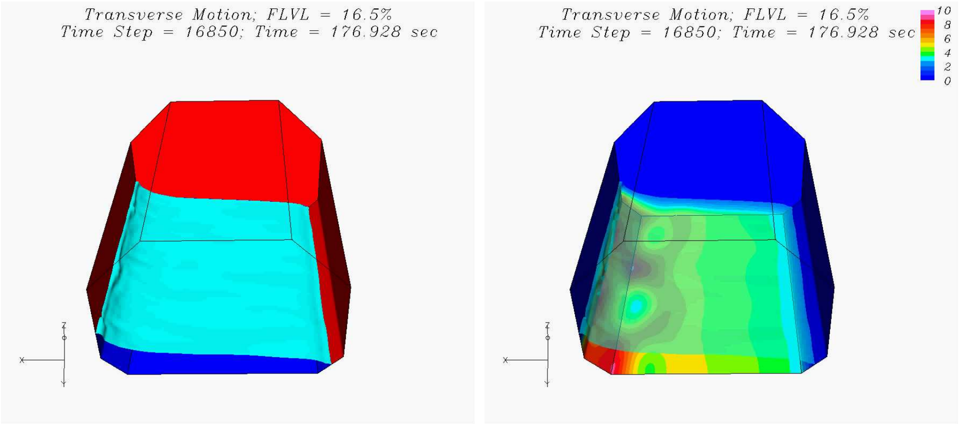

(b) Phase B: t/T = 16.85

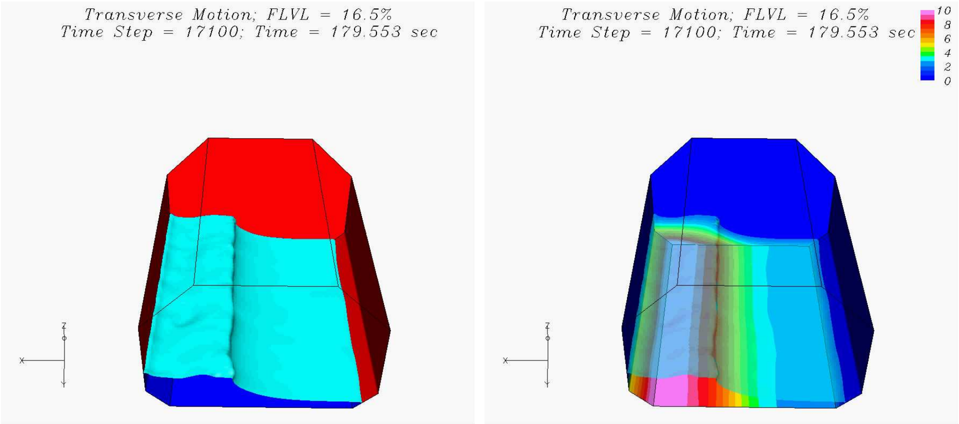

(c) Phase C: t/T = 17.10

Figure 5.16. 3D free surface and pressure contours, Case 1

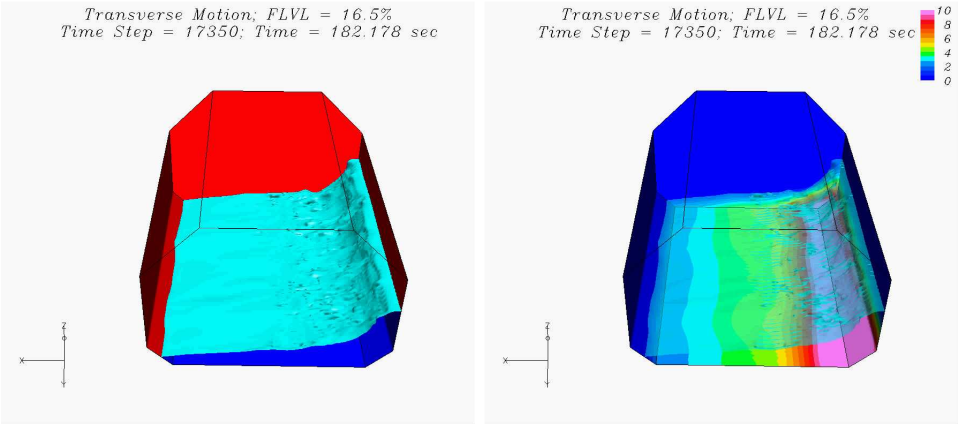

(d) Phase D: t/T = 17.35

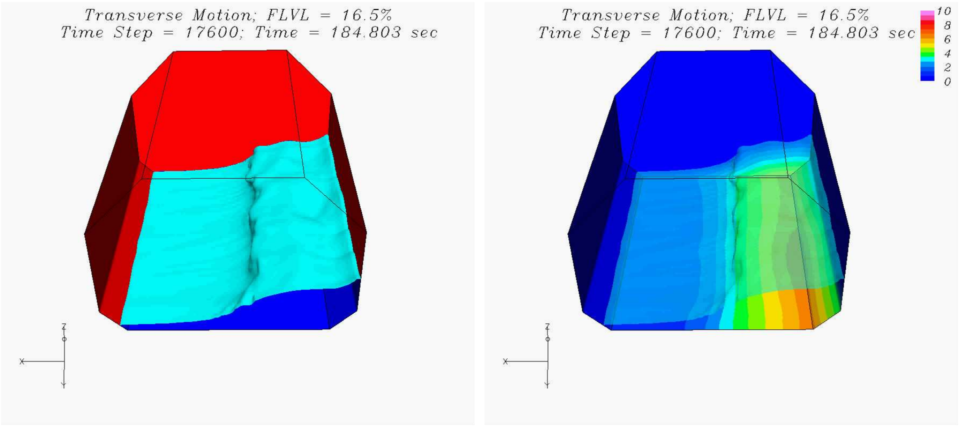

(e) Phase E: t/T = 17.60

Figure 5.16. (Continued)

5.5.2. Case 2 - Transverse & 30% FLVL

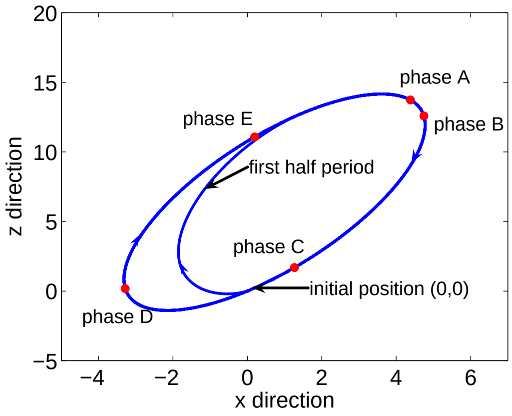

Figure 5.17. Tank motion trajectory, Case 2

Figure 5.17 shows the transverse motion trajectory of the LNG tank for Case 2 with the initial tank position at the origin (0,0). Due to different phase shifts and motion amplitudes in the horizontal and vertical directions, the trajectory of the prescribed tank motion is elliptic and asymmetric with respect to the x and z axes. In addition to the large amplitude translational motions, the tank also experienced a small amplitude roll motion with a maximum roll angle of ±0.344° .

Figure 5.18 shows the 2D simulation results of impact pressures for both the left

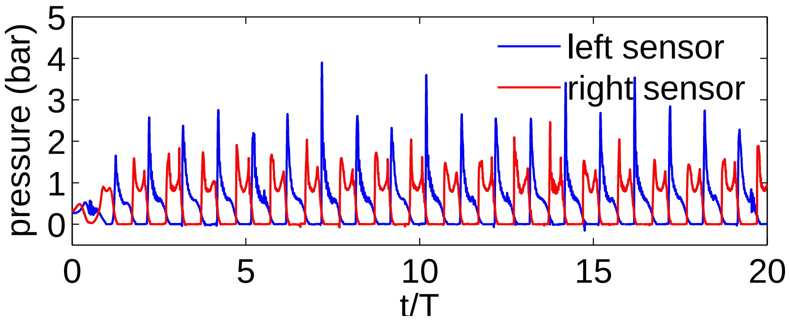

Figure 5.18. 2D pressure history, Ch.15, Case 2

and right pressure sensors corresponding to Ch.15. The predicted pressure histories are similar to those shown earlier for Case 1. Due to the asymmetric tank motion, the pressure at the right sensor location exhibits a distinct double-peak pattern, while a single-peak pattern is observed at the left sensor location.

Figures 5.19 and 5.20 show the comparisons of measured and predicted pressure

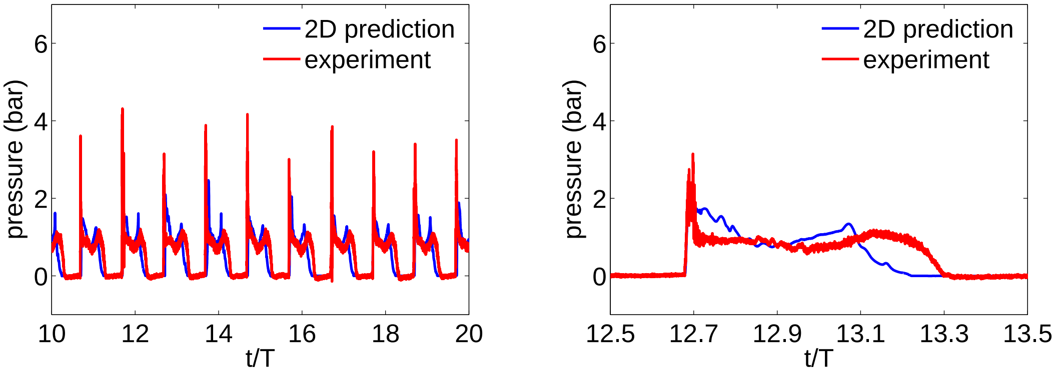

(a) 10 periods

(b) 1 period

Figure 5.19. 2D impact pressure, Ch.15 (right sensor), Case 2

histories at Ch.15 over 10 periods for the 2D and 3D simulations, respectively. It is seen that the pressure rises sharply due to water impact on the tank wall and decays rapidly following the impact. Similar to Case 1, the impact pressure at Ch.15 also exhibits a distinct double-peak pattern after the impact. In general, both the pressure pattern and peak pressure values are accurately predicted in 3D simulations. It should be noted that the pressure history shown in Figure 5.20 was recorded at sensor position S38 which is located at the mirror image position of S40. Due to the three-dimensional effects, the impact pressure at sensor location S38 is significantly higher than that at S40, and in closer agreement with the measured pressure at Ch.15.

Figure 5.21 shows the three-dimensional variations of the impact pressure in the

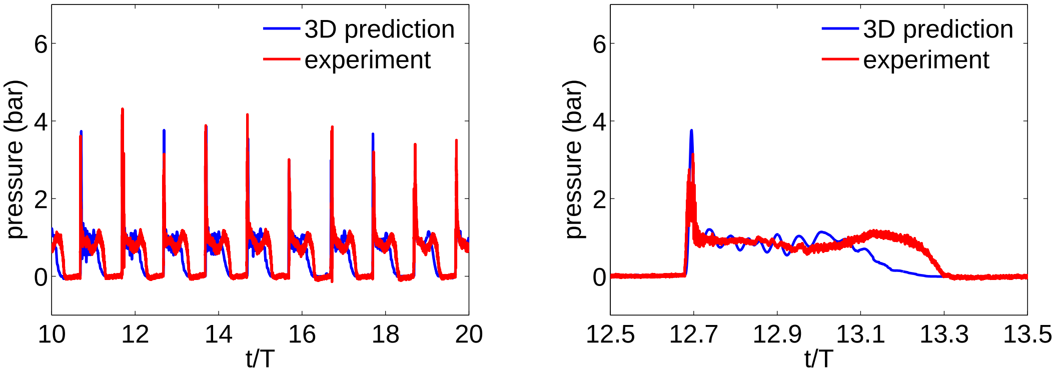

(a) 10 periods

(b) 1 period

Figure 5.20. 3D impact pressure, Ch.15 (S38), Case 2

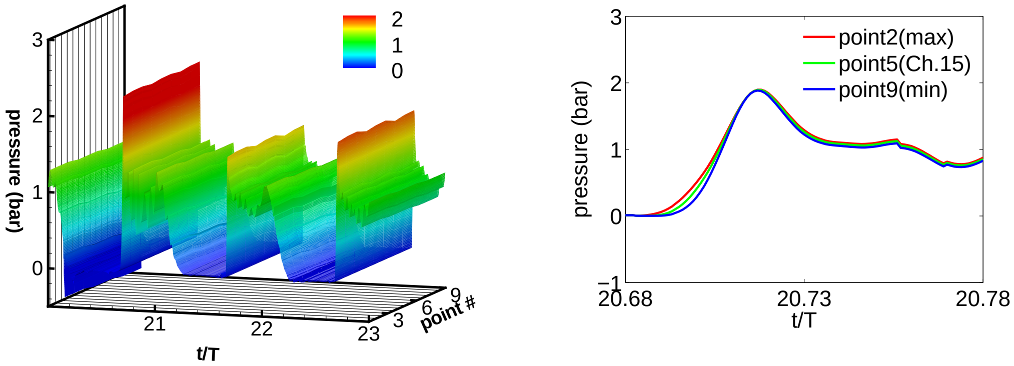

Figure 5.21. Impact pressures, the vicinity of Ch.15 (S38), Case 2

vicinity of Ch.15 (S38) pressure sensor location. It is seen that the impact pressure is fairly uniform at this location, so the pressure at Point 5 is a good representation of the pressure at Ch.15. A detailed examination of the 3D pressure history over a single sloshing period shown in Figure 5.20(b) indicates that the peak impact pressure occurs at $t/T = 12.695$ over this specific period. On the other hand, the 2D impact occurs shortly after $t/T = 12.70$. In order to facilitate a more detailed understanding of the observed impact pressure pattern, it is desirable to examine the detailed velocity and pressure fields induced by the sloshing tank motions immediately before and after the peak impact corresponding to Phase A ($t/T = 12.65$) and Phase B ($t/T = 12.70$) in the motion trajectory shown in Figure 5.17. For completeness, the 2D and 3D flow and pressure fields will also be presented at three other times instants $t/T = 12.95, 13.20$ and 13.45 which are denoted by Phases C, D, and E in Figure 5.17. Note that Phases B, C, D, and E were chosen to be $T/4$ apart to illustrate the general flow patterns over one sloshing period.

Figure 5.22 shows the 2D free surface patterns, velocity vectors, and pressure contours at five time instants $t/T = 12.65, 12.70, 12.95, 13.20$ and 13.45, which are denoted by Phases A-E in the motion trajectory plot shown earlier in Figure 5.17. As noted earlier, the maximum 3D impact pressure at sensor location S37 occurs at $t/T = 12.695$ just prior to Phase B ($t/T = 12.70$) for the 3D case when the LNG tank reaches the upper-right corner and begins to descend towards the lower-left corner along the elliptic motion trajectory. In the present two-dimensional simulations, however, the sloshing water has not yet reached the tank right wall at Phase B. As noted earlier, the 2D impact on the left wall occurs shortly after $t/T = 12.70$. In view of this, we will focus on the three-dimensional flow patterns in the following discussions.

Figure 5.23 shows the predicted 3D free surface motions and the corresponding

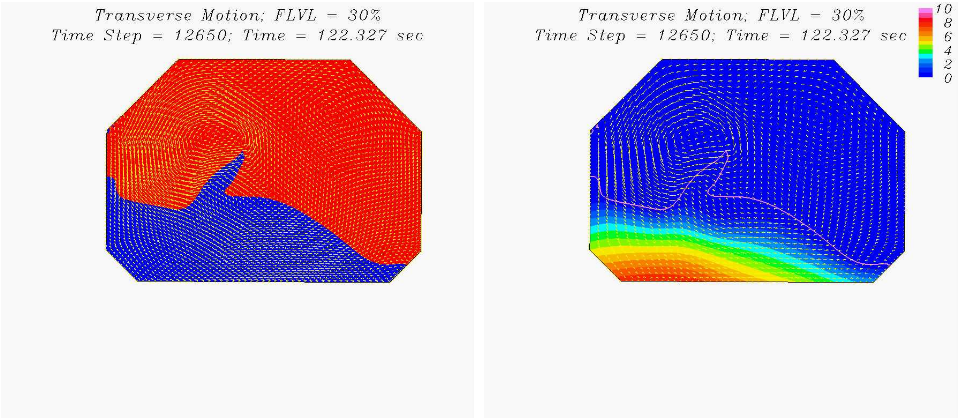

(a) Phase A: t/T = 12.65

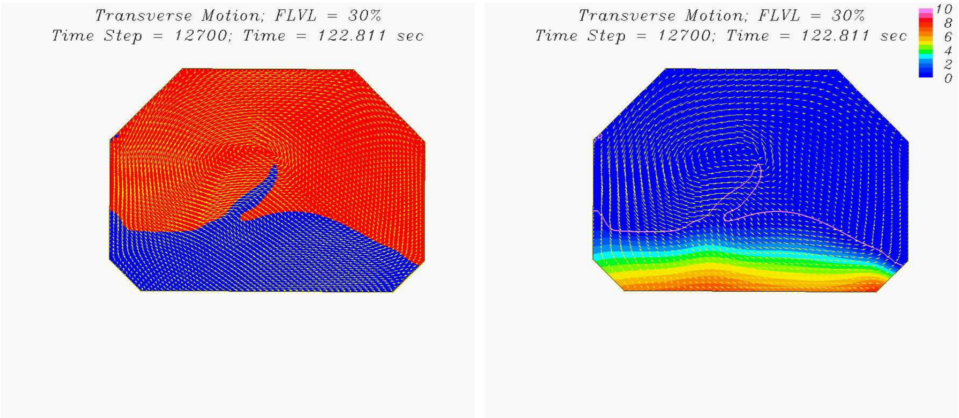

(b) Phase B: t/T = 12.70

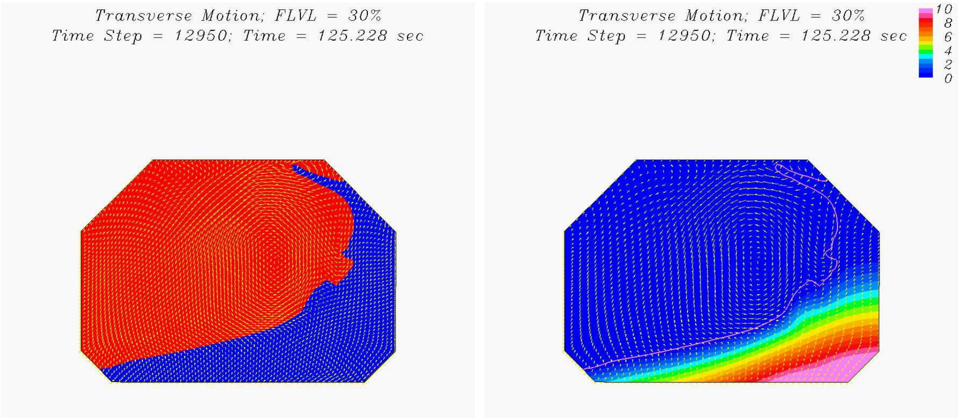

(c) Phase C: t/T = 12.95

Figure 5.22. 2D free surface, $\vec{V}, p$, Case 2

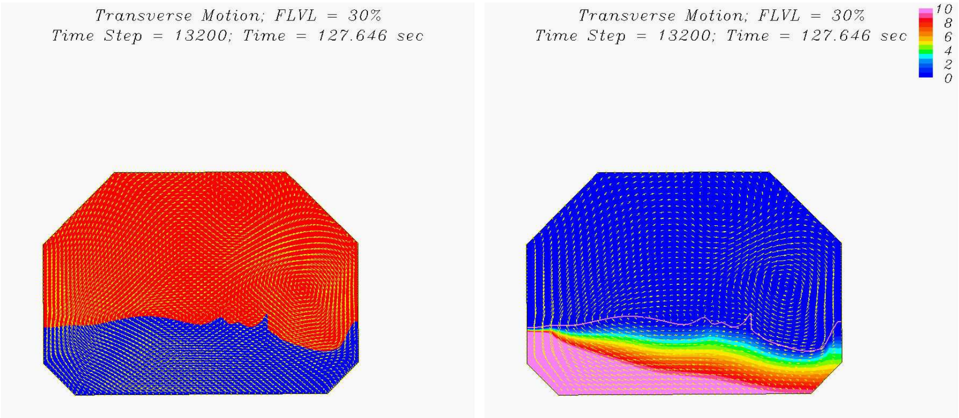

(d) Phase D: t/T = 13.20

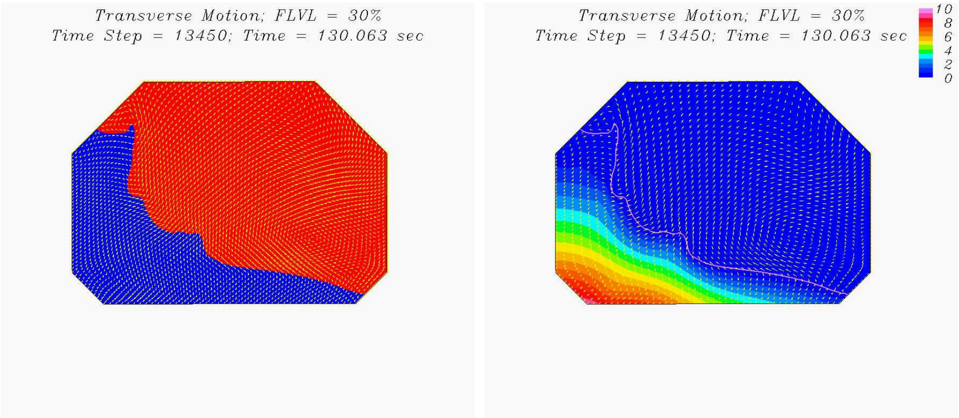

(e) Phase E: t/T = 13.45

Figure 5.22. (Continued)

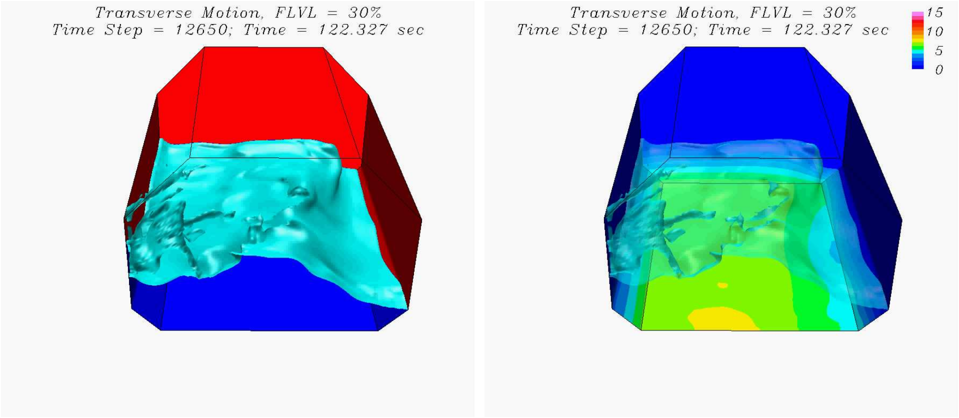

(a) Phase A: t/T = 12.65

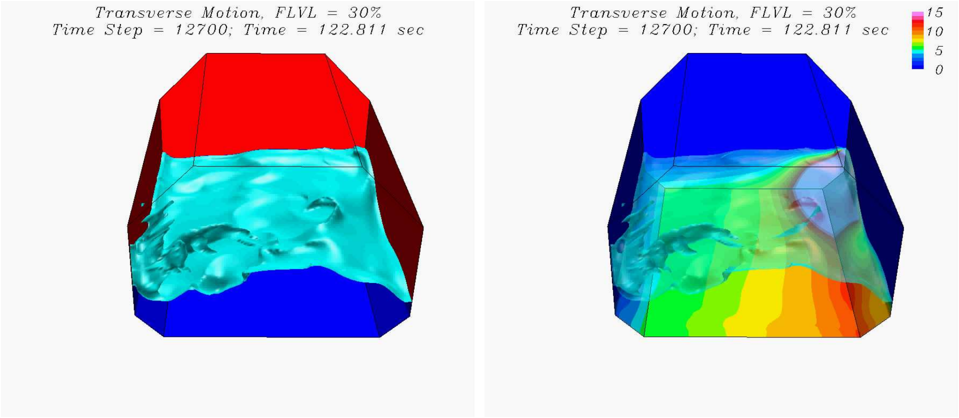

(b) Phase B: t/T = 12.70

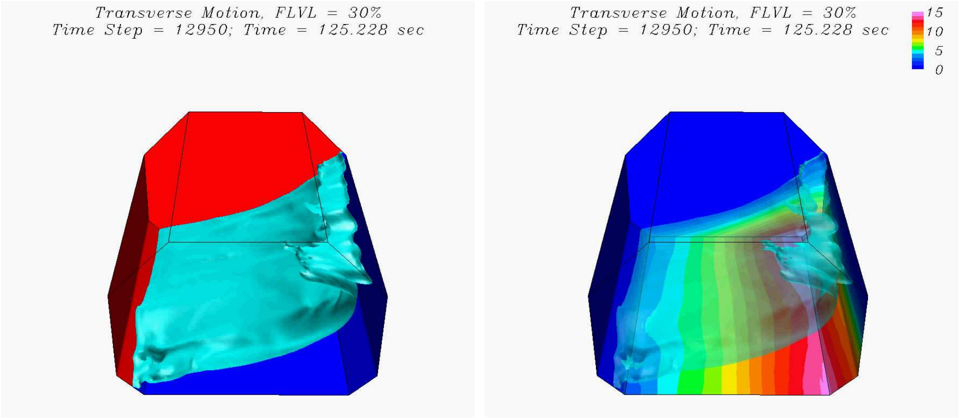

(c) Phase C: t/T = 12.95

Figure 5.23. 3D free surface and pressure contours, Case 2

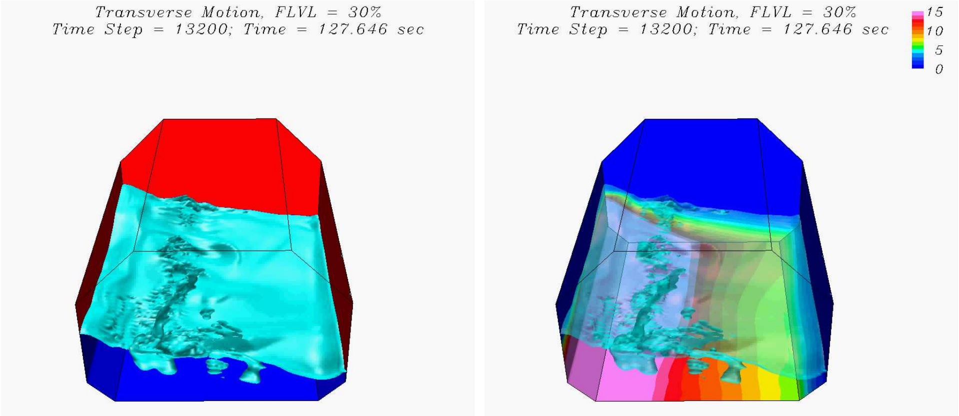

(d) Phase D: t/T = 13.20

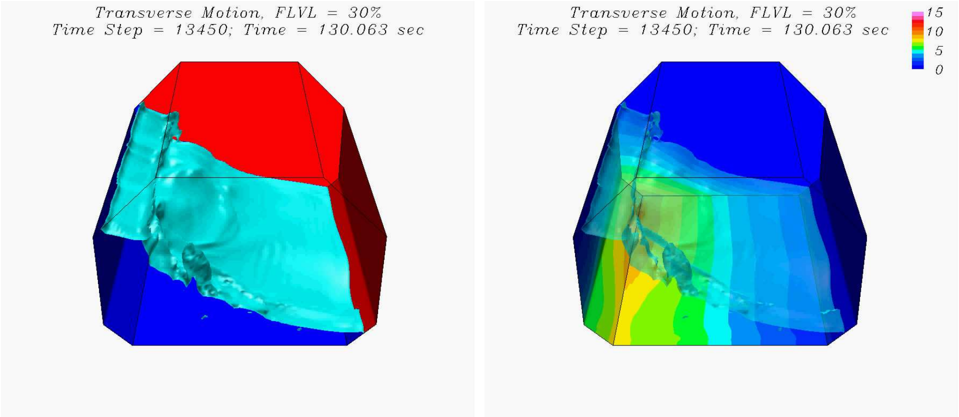

(e) Phase E: t/T = 13.45

Figure 5.23. (Continued)

pressure contours on tank walls at five different time instants for Case 2. As noted earlier, the maximum impact pressure at pressure sensor location S38 (mirror image of Ch.15 in model tank) occurs at $t/T = 12.695$ when the LNG tank reaches the upper-right corner of the motion trajectory and begins to descend towards the lower-left corner. It is seen that the sloshing water moves rapidly from left to right between Phases A ($t/T = 12.65$) and B ($t/T = 12.70$) and produced a very high impact pressure on the right tank wall where the S38 pressure sensor is located. After the primary impact, the water continues to rush up the tank side wall. This leads to a double-peak pressure pattern since the pressure sensor S37 (Ch.15) is submerged under increasing water depth between Phases B and C. At Phase D ($t/T = 13.20$), the tank just passed the lower-left corner of the motion trajectory and begins to ascend along the upper half of the elliptic motion trajectory. At this instant, the tank acceleration is close to maximum and acts in the opposite direction of the gravity acceleration. The combined effects of fluid momentum change (i.e., hydrodynamics pressure) and gravity (i.e., hydrostatic pressure) produced very high surface pressures around the lower-left corner of the LNG tank as shown in Figure 5.23(d). Between Phases D and E, the water continued to move up the left tank wall while the tank right wall is completely exposed with zero pressure reading on Ch.15. The experimental data in Figure 5.20(b) indicates a somewhat slower decay of pressure at Ch.15 during this stage. The observed discrepancy may be due to the surface tension effects at model scale, which is ignored in the present full scale simulations. It is also worthwhile to note that the flow pattern is highly three-dimensional even though the excitation force due to the prescribed transverse motion is strictly two dimensional. The three-dimensional instability of the sloshing flow was also confirmed by the experimental observations.

5.5.3. Case 3 - Transverse & 50% FLVL

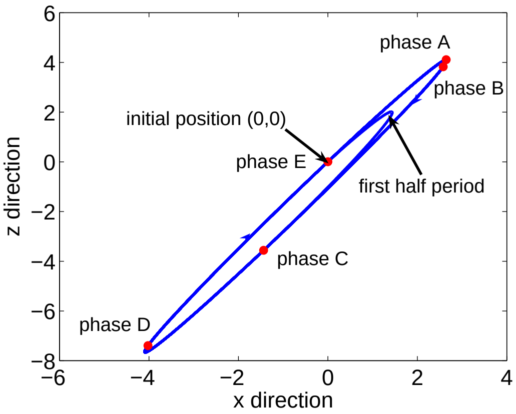

Figure 5.24. Tank motion trajectory, Case 3

Figure 5.24 shows the trajectory of the LNG tank center for Case 3 in prescribed transverse motion. It is worthwhile to note that the initial tank position for Cases 1 and 2 are located on the lower half of their corresponding motion trajectories. On the other hand, the tank motion for Case 3 is initiated on the upper half of the motion trajectory. Consequently, the sloshing flow patterns for Case 3 are also out of phase with those observed earlier for Cases 1 and 2. As shown in Table 5.2, the horizontal and vertical motion amplitudes for Case 3 are somewhat smaller than those experienced by Case 2. The maximum roll angle ($\pm 0.142°$) is also smaller for Case 3. A modulation function was again applied for the first half period of the simulation to eliminate excessive fluid motion due to the impulsive start. Simulations were performed for 50 periods with a time increment of $0.001T$. The wall pressures at selected sensor locations were recorded every time step, while the 3D velocity and pressure fields for the entire tank were saved every 50 time steps.

Figure 5.25 shows the 2D simulation results of impact pressures for the left and right pressure sensors corresponding to Ch.11 and its mirror image. Note that

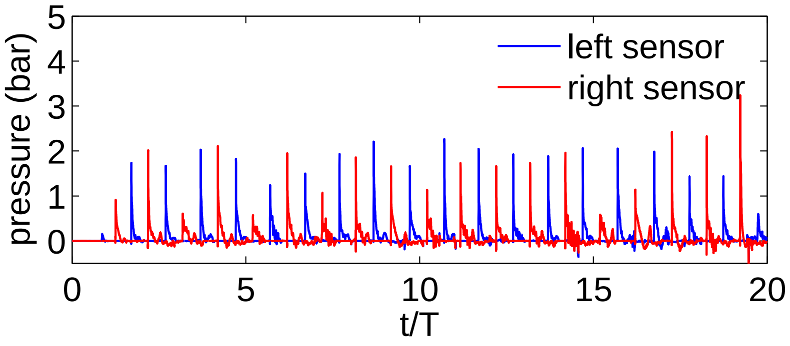

Figure 5.25. 2D pressure history, Ch.11, Case 3

Ch.11 is located on the inclined surface slightly above the lower knuckle point of the upper chamfer as shown in Figure 2. Under the transverse tank motion, the pressure patterns are again shifted by half-period between the left and right sensors. However, the impact pressures on the upper chamfer exhibit similar single-peak patterns at both the left and right sensor locations since Ch.11 is located on the upper chamfer.

Figures 5.26 and 5.27 show the comparisons of measured and predicted pressure histories at Ch.11 over 10 periods for the 2D and 3D simulations, respectively.

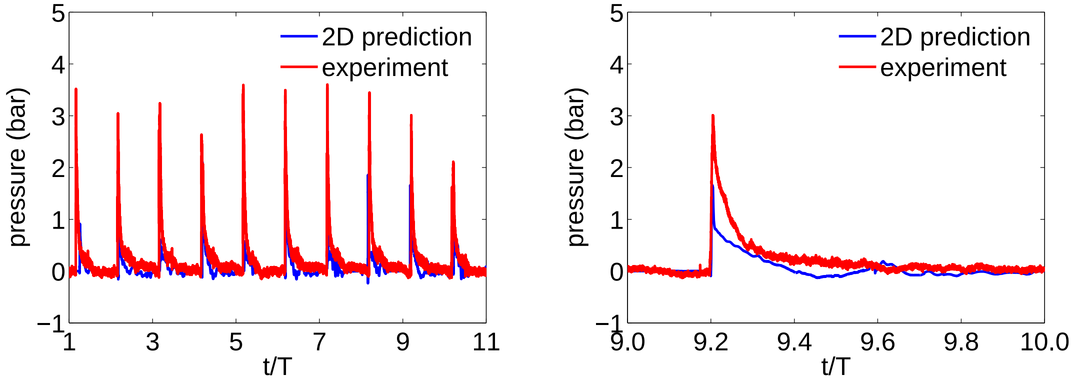

(a) 10 periods (b) 1 period

Figure 5.26. 2D impact pressure, Ch.11 (right sensor), Case 3

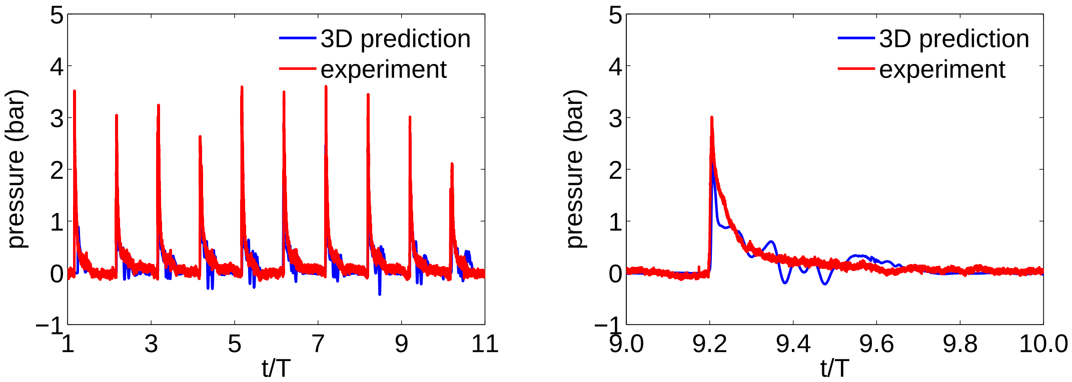

(a) 10 periods (b) 1 period

Figure 5.27. 3D impact pressure, Ch.11 (S04), Case 3

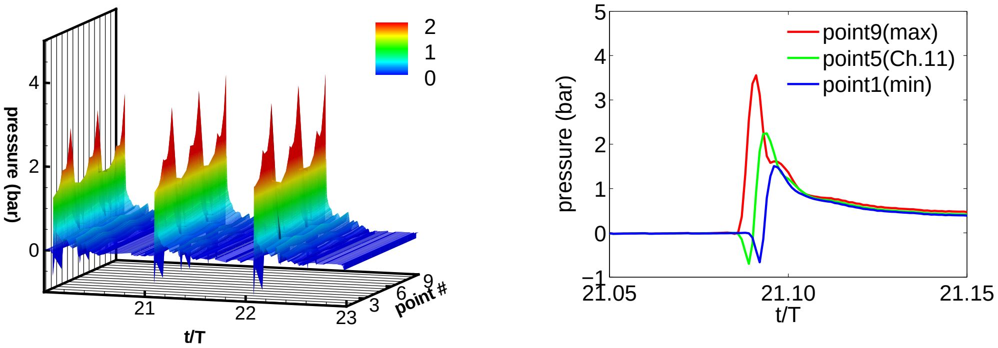

Figure 5.28. Impact pressures, the vicinity of Ch.11 (S04), Case 3

It is seen that the pressure rises sharply due to water impact on the tank wall and decays rapidly immediately after the impact. Unlike the double-peak patterns observed earlier for Cases 1 and 2, the pressure decays monotonically to zero following the impact. In general, the 3D pressure pattern at sensor location S04 is in closer agreement with the experimental data than the corresponding 2D simulation result. It is also seen from Figure 5.28 that the peak impact pressure is highly localized in the vicinity of the pressure sensor with very sharp variations between two adjacent grid points. A detailed examination of the 3D pressure history over a single period shown in Figure 5.27(b) indicates that the maximum impact pressure occurs at $t/T = 9.207$ over this specific period. In the following, we will examine the 2D and 3D velocity and pressure fields at $t/T = 9.20, 9.25, 9.50, 9.75$ and 10.00. These five time instants are denoted by Phases A, B, C, D, and E, respectively, along the motion trajectory shown in Figure 5.24. Note that Phases B, C, D, and E were chosen to be $T/4$ apart to illustrate the general flow patterns over one sloshing period.

In order to facilitate a more detailed understanding of the observed impact pressure pattern for Case 3, it is desirable to examine the 2D and 3D velocity and pressure fields induced by the sloshing tank motions as shown in Figures 29 and 30, respectively. A comparison of Figures 5.29(a) and 5.30(a) for Phase A ($t/T = 9.20$) indicates that the 2D simulation predicted a somewhat earlier impact at Ch.11 than the corresponding 3D simulation. This can be attributed to the three-dimensional effects which delayed the impact at pressure sensor location S04, even though a significant section of the inclined wall on the upper right chamfer was already inundated by sloshing water at $t/T = 9.20$. In the 3D simulations, the maximum impact pressure at Ch.11 occurs between Phases A and B when the LNG tank reaches the upper-right corner of the motion trajectory (see Figure 5.24) and begins to descend back to the equilibrium position. At Phase A ($t/T = 9.20$), the free surface around the Ch.11 pressure sensor

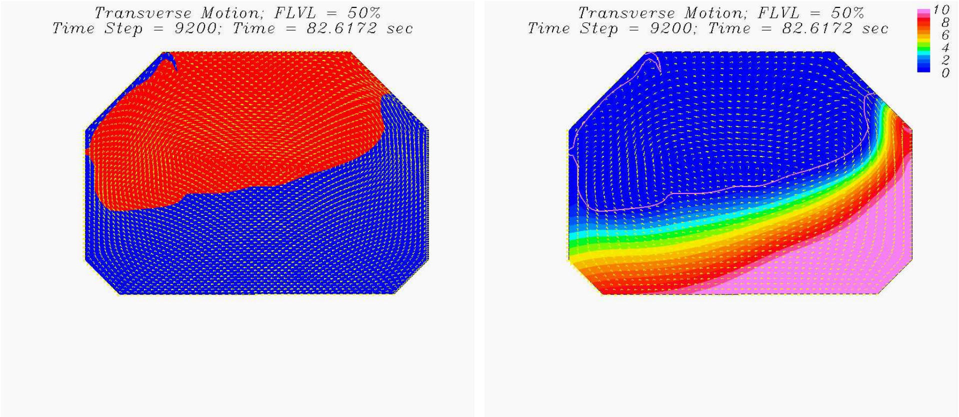

(a) Phase A: t/T = 9.20

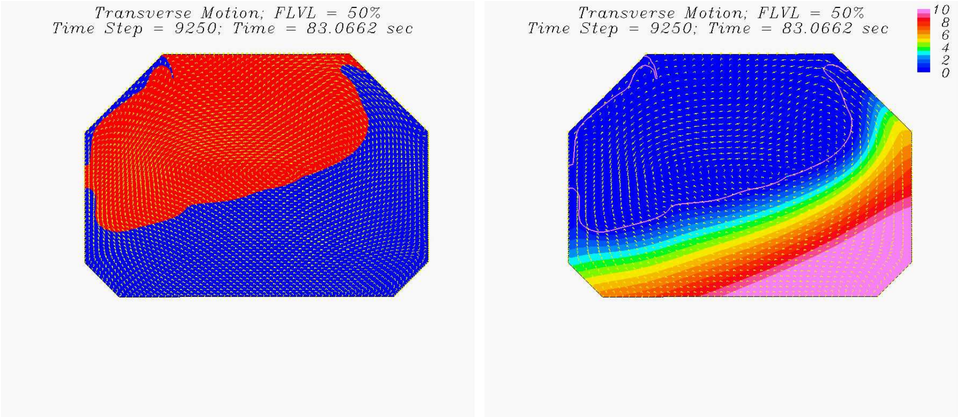

(b) Phase B: t/T = 9.25

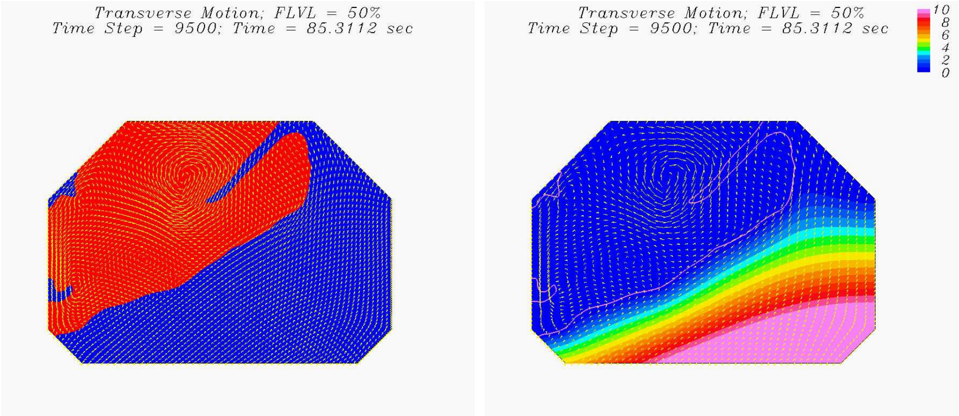

(c) Phase C: t/T = 9.50

Figure 5.29. 2D free surface, $\vec{V}, p$, Case 3

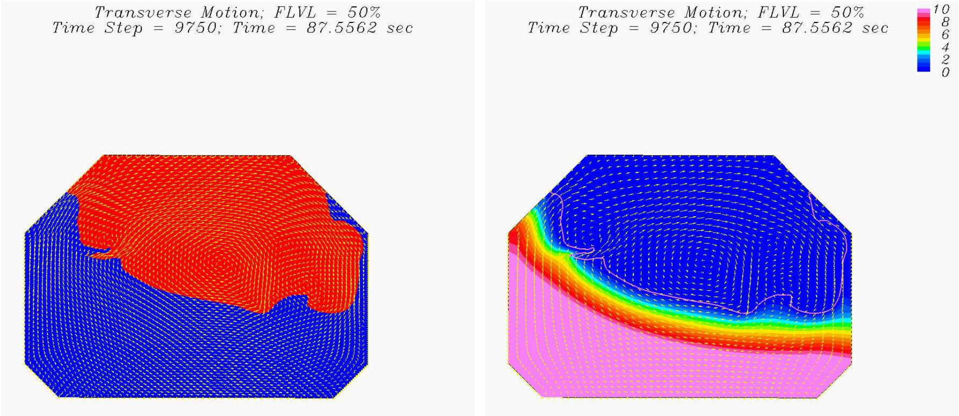

(d) Phase D: t/T = 9.75

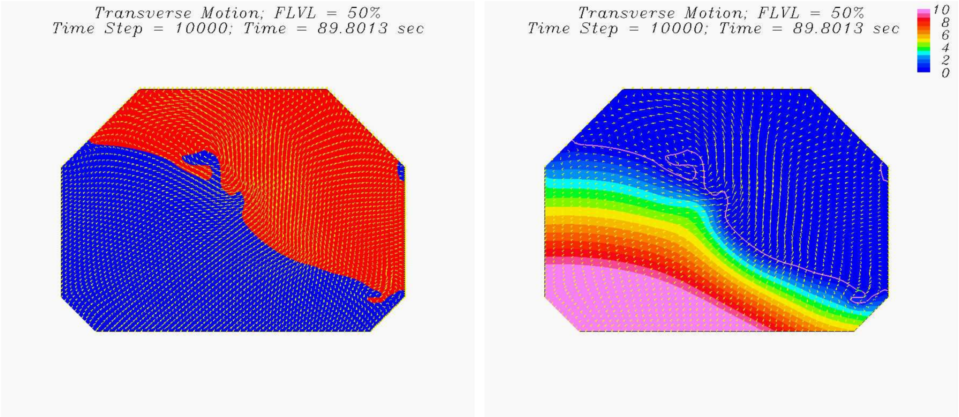

(e) Phase E: t/T = 10.00

Figure 5.29. (Continued)

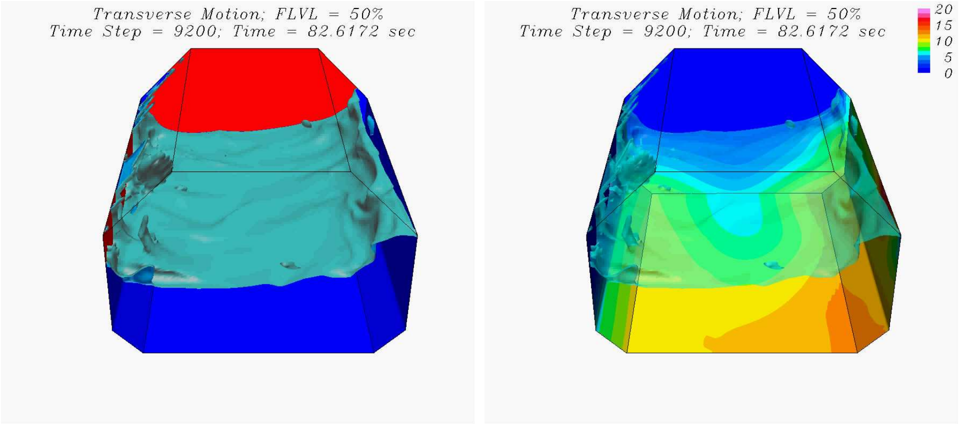

(a) Phase A: t/T = 9.20

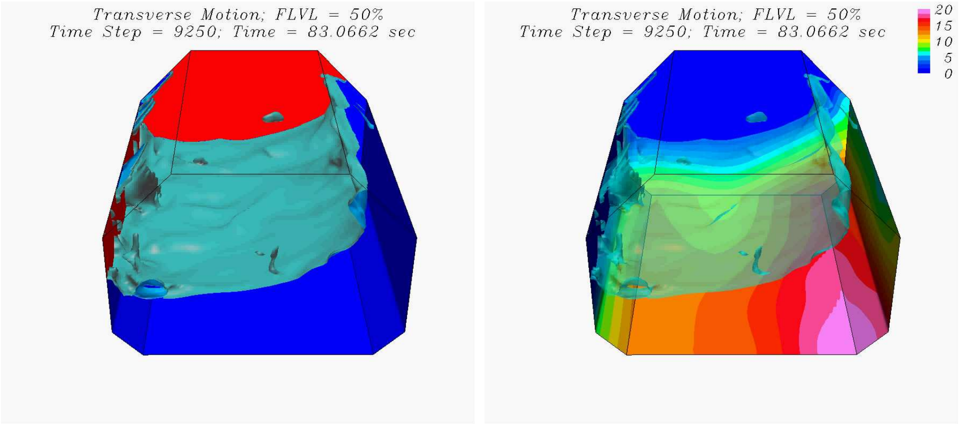

(b) Phase B: t/T = 9.25

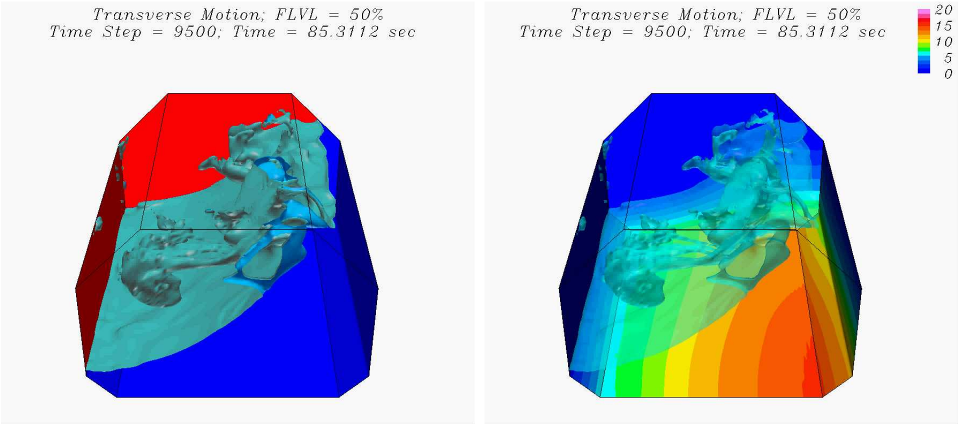

(c) Phase C: t/T = 9.50

Figure 5.30. 3D free surface and pressure contours, Case 3

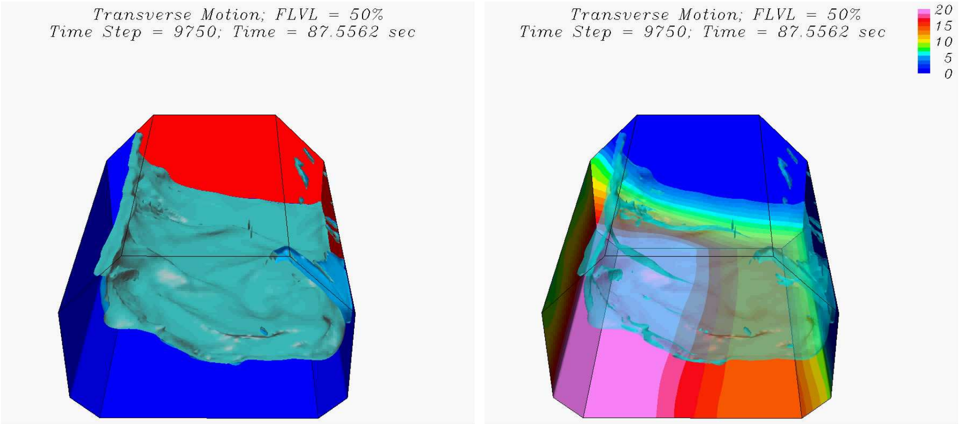
Transverse Motion; FLVL = 50%
Time Step = 9750; Time = 87.5562 sec

Transverse Motion; FLVL = 50%
Time Step = 9750; Time = 87.5562 sec

(d) Phase D: t/T = 9.75

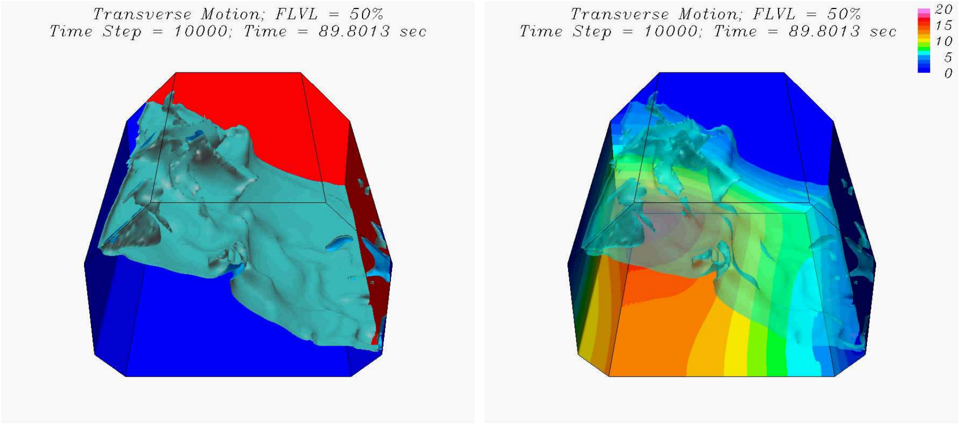
Transverse Motion; FLVL = 50%
Time Step = 10000; Time = 89.8013 sec

Transverse Motion; FLVL = 50%
Time Step = 10000; Time = 89.8013 sec

(e) Phase E: t/T = 10.00

Figure 5.30. (Continued)

is slightly below the lower knuckle point of the upper chamfer. As noted earlier, the maximum impact pressure was observed at $t/T = 9.207$ when the sloshing water rises rapidly over the lower knuckle point of the upper chamfer as seen at Phase B. At 50% filling level, the violent free surface flow was found to slam on the top wall of the LNG tank as seen in Figures 5.29(c) and 5.30(c) at $t/T = 9.50$. As the LNG tank continues to move downward along the lower half of the elliptic motion trajectory between Phases C and D, the standing wave moves towards the left wall and the water on the upper chamfer of the right tank wall recedes quickly. Consequently, the pressure at Ch.11 decays monotonically to zero without the presence of a double-peak pattern.

It is clearly seen from Figure 5.30 that the free surface and pressure patterns are highly three-dimensional even though the excitation force is strictly two-dimensional. Furthermore, it was observed in the experiments that the sloshing flow for Case 3 also developed a distinct swirling flow pattern in the LNG tank which was not present in the lower filling level cases (i.e., Cases 1 and 2). In view of this, we have continued the Case 3 simulation for 30 more periods in addition to the standard 20-period simulation. A detailed examination of the simulation results clearly indicates that the three-dimensional flow instability eventually leads to the development of a swirling flow pattern after about 25 sloshing periods similar to those observed in the experiment. Figure 5.31 shows the predicted swirling flow pattern over one sloshing period. It should be remarked that the swirling motion is not symmetric with respect to the tank center due to asymmetric tank motion. Moreover, the highest free elevation on four different corners does not occur exactly at T/4 interval since the LNG tank has a rectangular cross section with variable tank breadth in the lower and upper chamfers. The simulation results clearly illustrate the capability of the present method in predicting the three-dimensional instability induced by large amplitude motions in a partially filled LNG tank.

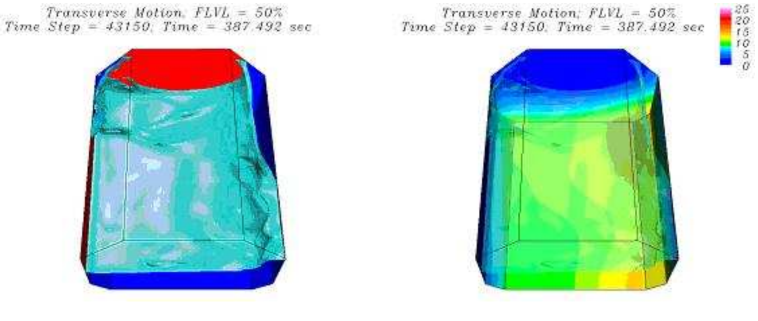

(a) t/T = 43.15

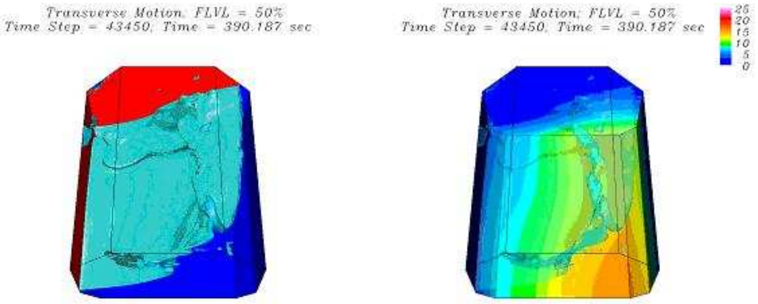

(b) t/T = 43.45

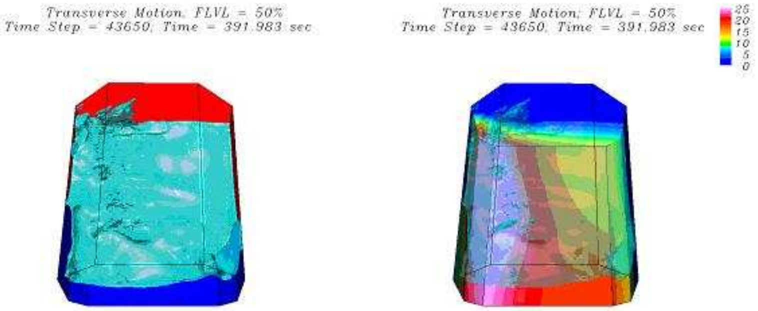

(c) t/T = 43.65

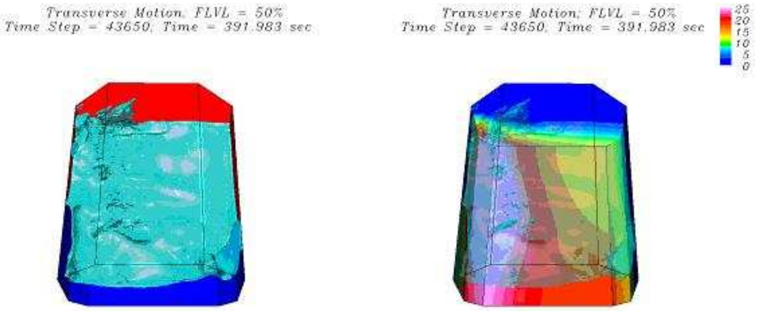

(d) t/T = 43.95

Figure 5.31. The swirling flow, Case 3

5.5.4. Case 4 - Longitudinal & 50% FLVL

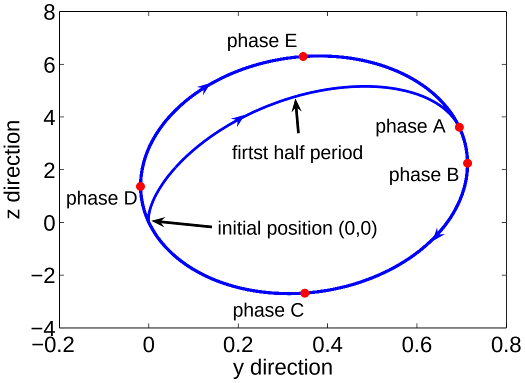

Figure 5.32. Tank motion trajectory, Case 4

Figure 5.32 shows the longitudinal motion trajectory (in yz-plane) of the LNG tank for Case 4 with the initial tank position at the origin (0,0). Note that the amplitude of horizontal motion is much smaller than the vertical motion amplitude. In addition to the large amplitude vertical motions, the tank also experienced a large amplitude roll motion with a maximum pitch angle of ±4.80° . A modulation function was again applied for the first half cycle to eliminate the pressure oscillations caused by the impulsive start of the LNG tank motion. Simulations were performed for 20 periods and the wall pressures at selected sensor locations were recorded every time step to facilitate a direct comparison with the experimental data.

Figure 5.33 shows the 2D impact pressures for both the left and right pressure sensors corresponding to Ch.3 on the top wall of the LNG tank as shown in Figure 5.7. It is quite clear that the sloshing water did not hit the top wall in the present two-dimensional simulations. The three-dimensional simulation result also indicates that the sloshing water did not reach the top wall even though the predicted water level is significantly higher than that observed in the 2D simulation.

Figure 5.34 shows a comparison of the measured impact pressure history at Ch.1

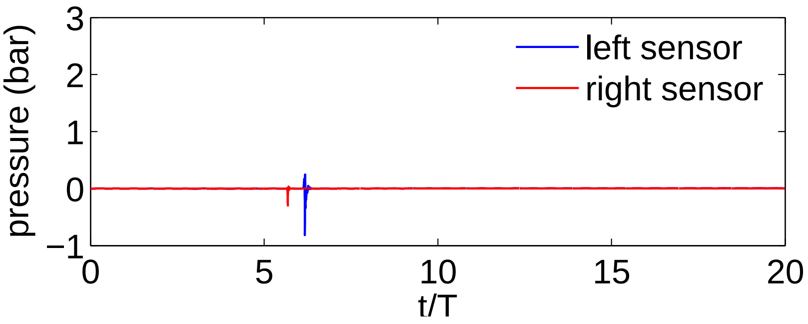

Figure 5.33. 2D pressure history, Ch.3, Case 4

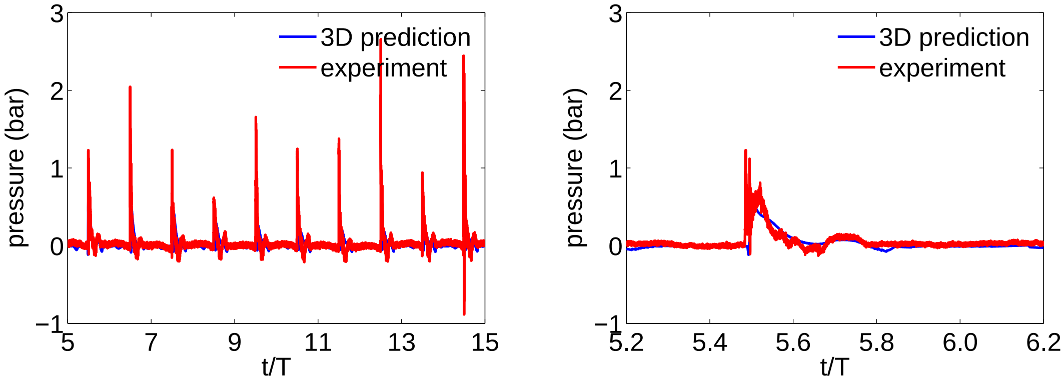

(a) 10 periods

(b) 1 period

Figure 5.34. 3D impact pressure, Ch.1 (S04), Case 4

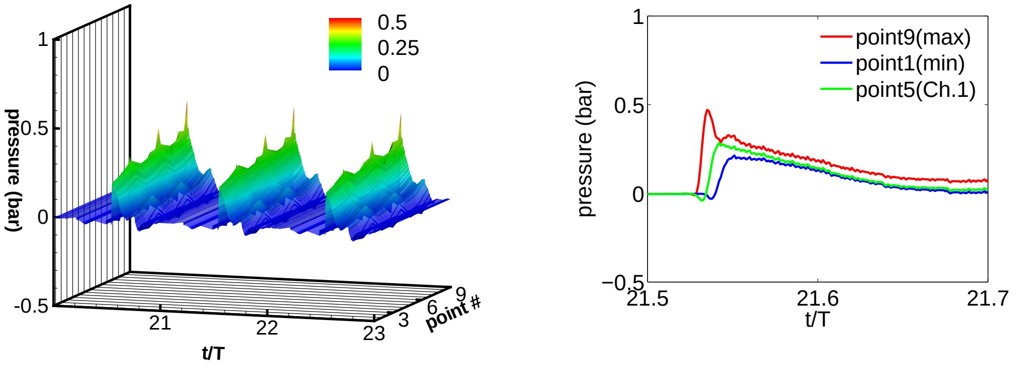

Figure 5.35. Impact pressures, the vicinity of Ch.1 (S04), Case 4

(see Figure 5.2) with that obtained from the 3D simulations. As shown in Figure 5.2, Ch.1 is located on the inclined surface slightly above the lower knuckle point of the upper chamfer. It coincides with the pressure sensor S04 in Figure 5.8, and is symmetric with Ch.11 on the opposite wall. It is seen from Figure 5.34 that the pressure at Ch.1 rises sharply due to water impact on the tank wall and decays monotonically after the impact. In general, the pressure pattern is in reasonably agreement with the experimental data although the peak pressures are somewhat underpredicted. Also, the peak impact pressure is highly localized in the vicinity of the pressure sensor location as shown in Figure 5.35. A detailed examination of the pressure history over a single period shown in Figure 5.34(b) indicates that the maximum impact pressure occurs at $t/T = 5.505$ over this specific period. For completeness, we will examine the detailed velocity and pressure fields at $t/T = 5.50, 5.55, 5.80, 6.05$ and 6.30, which are denoted by Phases A, B, C, D, and E, respectively, on the motion trajectory shown in Figure 5.32.

Figure 5.36 shows the predicted 2D free surface flow patterns and the corresponding pressure contours for Case 4 at five different phases A-E which were marked in

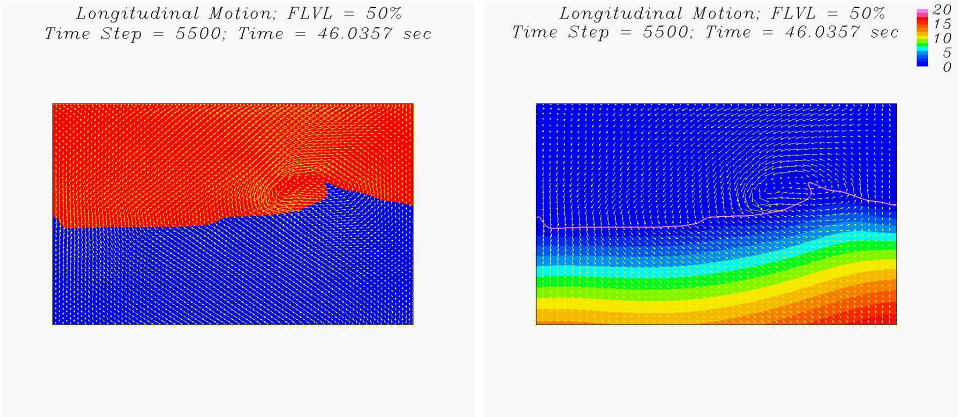

(a) Phase A: t/T = 5.50

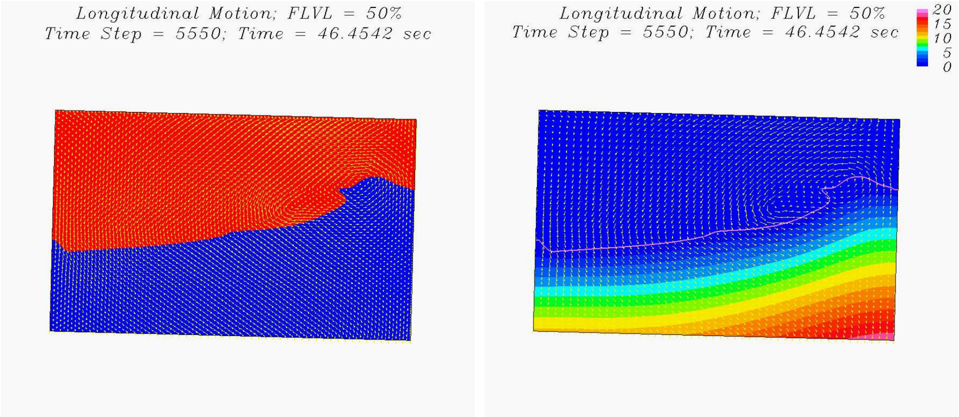

(b) Phase B: t/T = 5.55

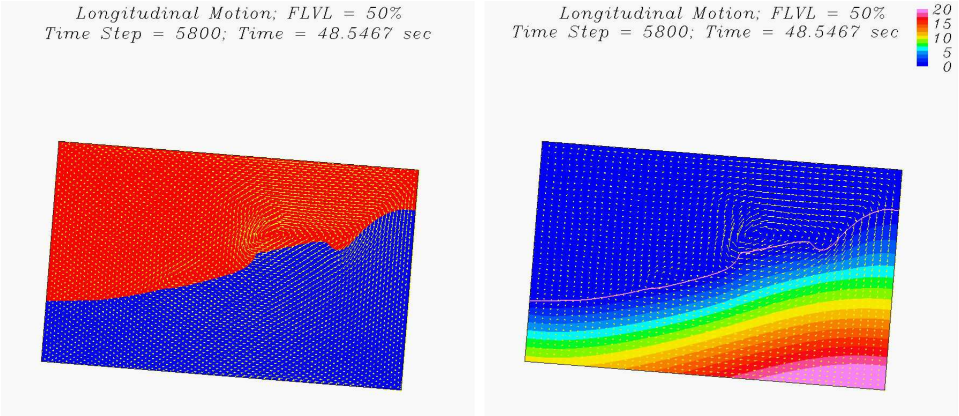

(c) Phase C: t/T = 5.80

Figure 5.36. 2D free surface, $\vec{V}, p$, Case 4

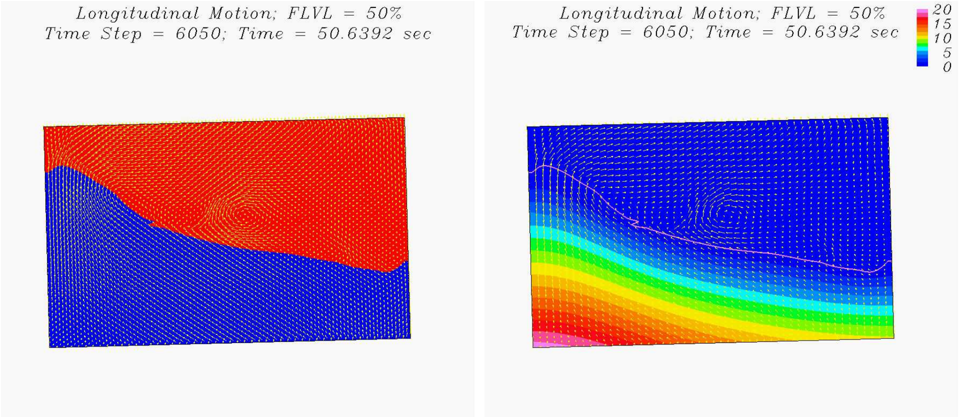

(d) Phase D: t/T = 6.05

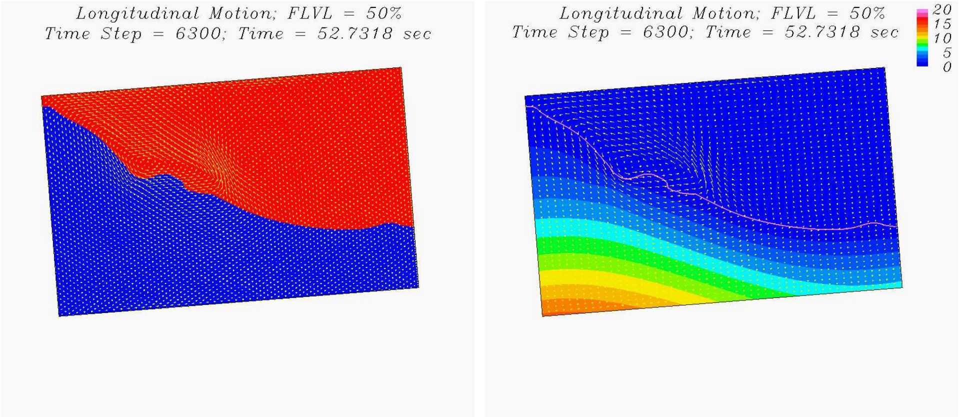

(e) Phase E: t/T = 6.30

Figure 5.36. (Continued)

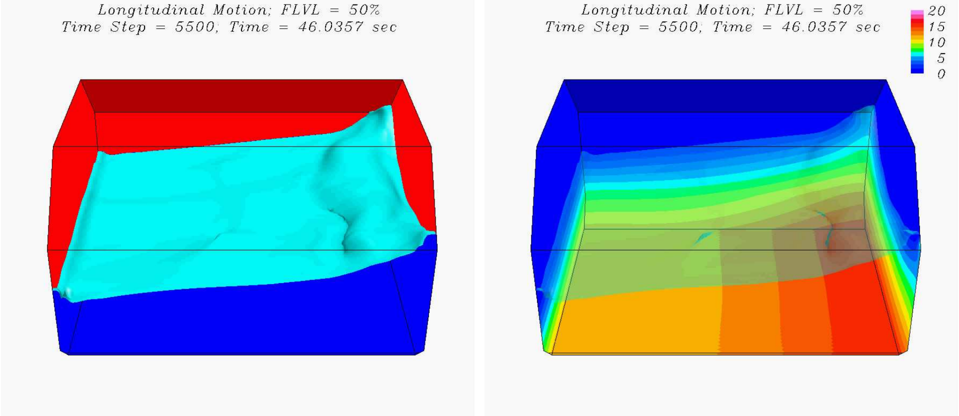

(a) Phase A: t/T = 5.50

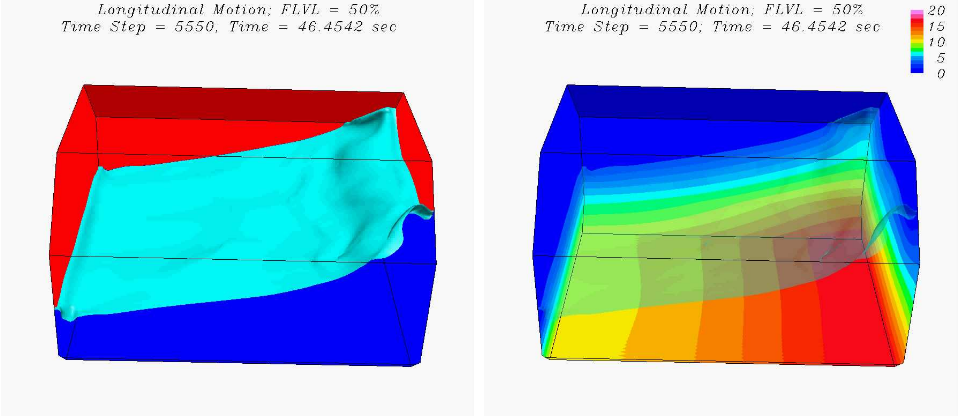

(b) Phase B: t/T = 5.55

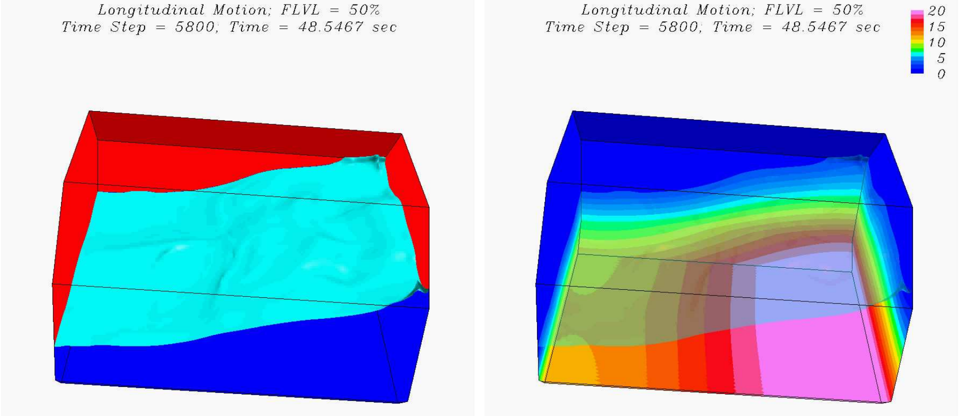

(c) Phase C: t/T = 5.80

Figure 5.37. 3D free surface and pressure contours, Case 4

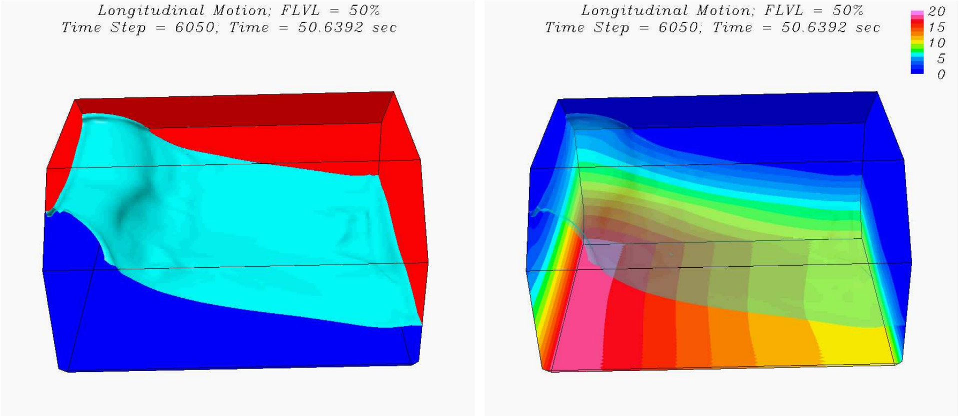

(d) Phase D: t/T = 6.05

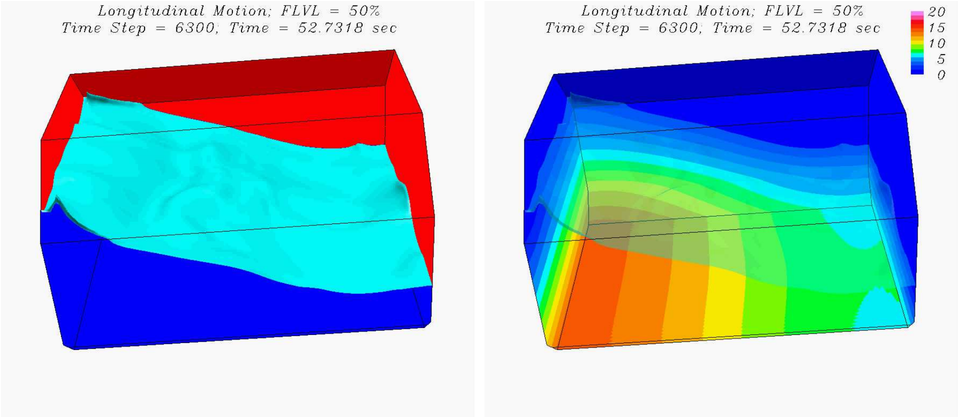

(e) Phase E: t/T = 6.30

Figure 5.37. (Continued)

the trajectory plot shown earlier in Figure 5.32. It should be remarked that the two-dimensional simulation results obtained here cannot properly account for the reduction of tank cross section area in the upper or lower chamfers of the three-dimensional LNG tank shown in Figure 5.1. Consequently, the predicted free surface elevation tends to be lower than the corresponding three-dimensional simulation results shown in Figure 5.37. As noted earlier, the maximum impact pressure at Ch.1 occurs at $t/T = 5.505$ in the present 3D simulation. At Phase A ($t/T = 5.50$), the free surface level is just below Ch.1 pressure sensor location. After impact, the water level continues to rise along the inclined wall of the upper chamfer as seen in Figure 5.37(b). However, the sloshing water never hit the top wall of the tank in the present simulation. On the other hand, experimental observation in the model tank clearly indicates the presence of violent free surface motions with numerous water droplets impinging on the tank top. It is quite clear that the present $85 \times 101 \times 85$ grid is too coarse to resolve the water droplets and their impacts on the top surface of the LNG tank. In spite of the observed discrepancy on the tank top wall, the impact pressure at Ch.1 on the upper chamfer was in fairly agreement with the corresponding experimental data as shown earlier in Figure 5.34.

5.5.5. Case 5 - Longitudinal & 80% FLVL

Figure 5.38 shows the trajectory of the LNG tank center for Case 5 in prescribed transverse motion with 80% fluid filling level. Comparing to Case 4, the horizontal motion amplitude is somewhat larger but the vertical motion amplitude is reduced by more than 60%. The maximum pitch angle ($\pm 0.693°$) for Case 5 is also much smaller than that experienced by Case 4. A modulation function was again applied for the first half period of the simulation to eliminate excessive fluid motion due to the impulsive start. It is worthwhile to note that the orientation of the elliptic motion

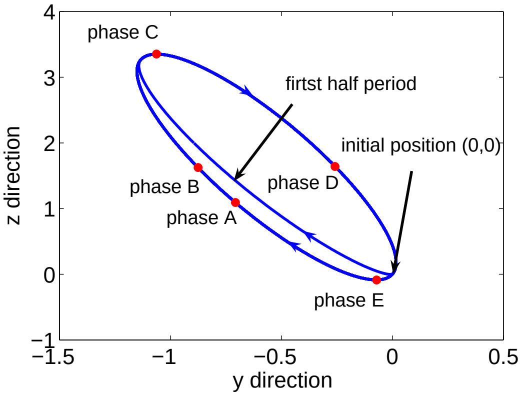

Figure 5.38. Tank motion trajectory, Case 5

trajectory for Case 5 is different from the previous four cases with the LNG tank oscillates between the lower-right and top-left corners.

Figure 5.39 shows the predicted 2D impact pressure history for both the left

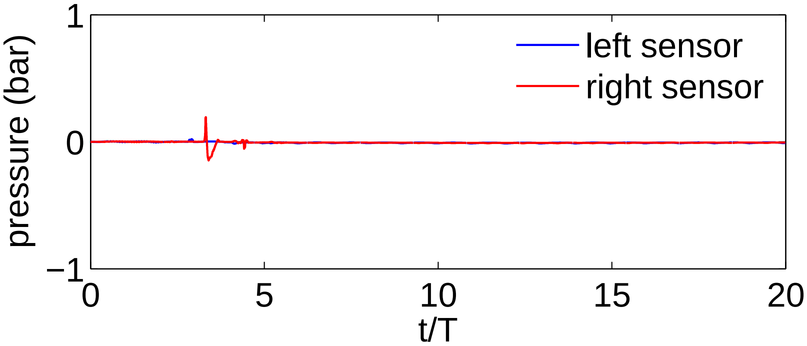

Figure 5.39. 2D pressure history, Ch.7, Case 5

and right sensors on the tank top. The 2D simulation again failed to predict the impact of sloshing water on the top surface of the LNG tank even though the fluid filling level has been increased from 50% to 80%. On the other hand, the 3D simulation results shown in Figure 5.40 accurately predicted the impact pressure at Ch.7 (Senor S11) on the top wall of the LNG tank. It is also seen from Figure 5.41 that the impact pressure is highly localized with huge pressure variations within the 3×3

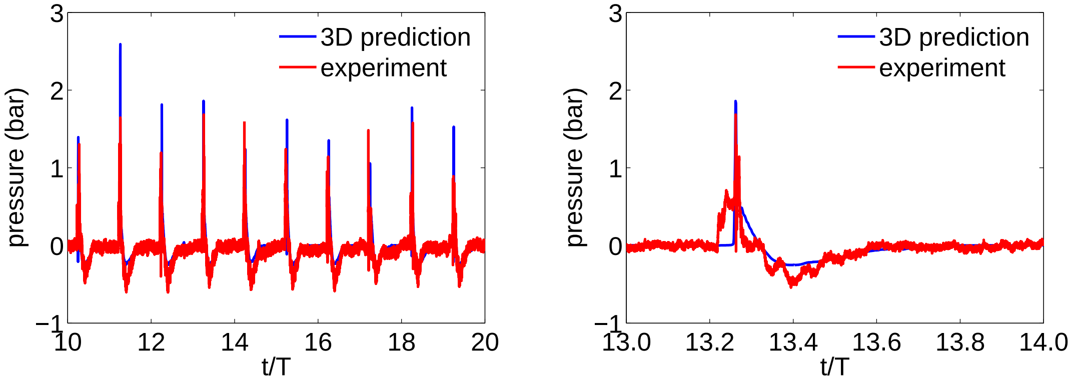

(a) 10 periods (b) 1 period

Figure 5.40. 3D impact pressure, Ch.7 (S11), Case 5

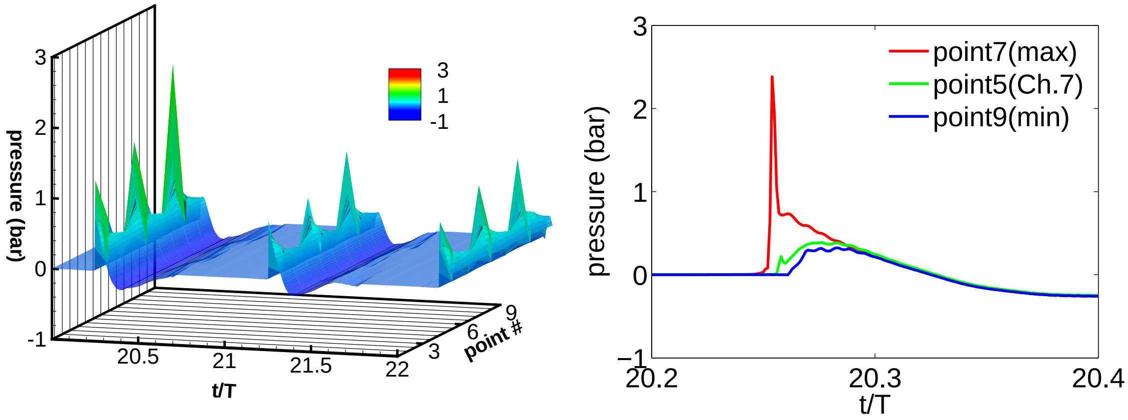

Figure 5.41. Impact pressures, the vicinity of Ch.7 (S11), Case 5

numerical element surrounding Ch.7. A detailed examination of the pressure history over a single period shown in Figure 5.40(b) indicates that the maximum impact pressure occurs at $t/T = 13.262$ over this specific period. To facilitate a more detailed understanding of the observed impact pressure pattern, we will examine both the 2D and 3D flow fields at $t/T = 13.25, 13.30, 13.55, 13.80$ and 14.05, which are denoted by Phases A-E in Figure 5.38.

Figure 5.42 shows the predicted two-dimensional free surface motions and the corresponding pressure contours in the sloshing LNG tank. Due to incorrect representation of the tank geometry, the sloshing water was not able to hit the tank top in the present 2D simulation. More specifically, the two-dimensional rectangular grid cannot account for the reduction of tank cross sectional area in the upper chamfer. In order to facilitate a more detailed understanding of the three-dimensional effects for sloshing flow in the upper chamfer, it is desirable to compare the 2D flow patterns to the corresponding 3D simulation results shown in Figure 5.43.

Figure 5.43 shows the predicted free surface motions and the corresponding pressure contours for Case 5 in the three-dimensional LNG tank. Comparing to the two-dimensional rectangular tank geometry shown in Figure 5.42, it is quite obvious that the sloshing flow near the tank top wall is greatly affected by the inclined surfaces of the upper chamfer. Due to the narrowing of tank cross section near the top wall, the sloshing flow is forced to converge towards the top surface with stronger acceleration and increasing water elevation than those encountered in a rectangular tank. During the selected period $13 < t/T < 14$ shown in Figure 5.40(b), the peak impact occurs at $t/T = 13.262$ between Phases A and B. It is seen from Figure 5.43(a) that the free surface level near Ch.7 is slightly below the tank top at Phase A ($t/T = 13.25$). When the LNG tank continues to move towards the upper-left corner from Phases A to Phase B, the combined translational and rotational motion of the tank produced

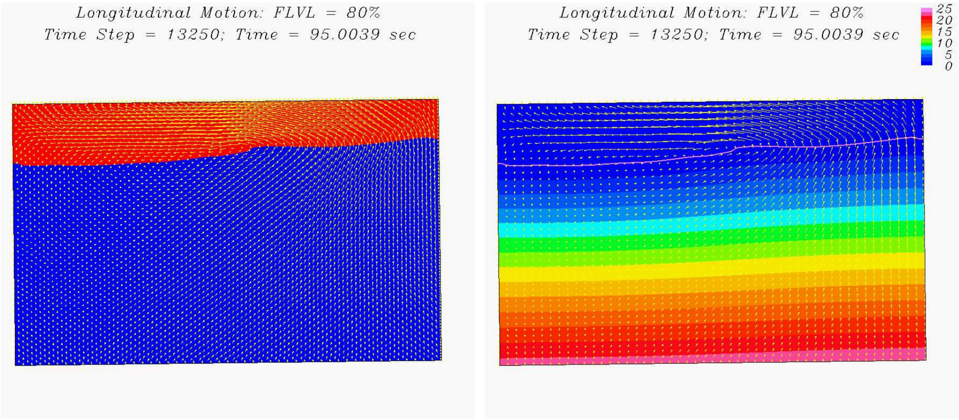

(a) Phase A: t/T = 13.25

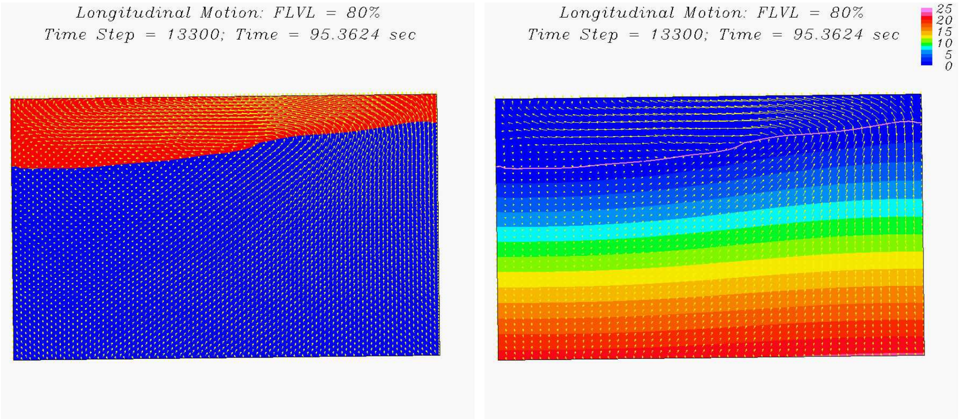

(b) Phase B: t/T = 13.30

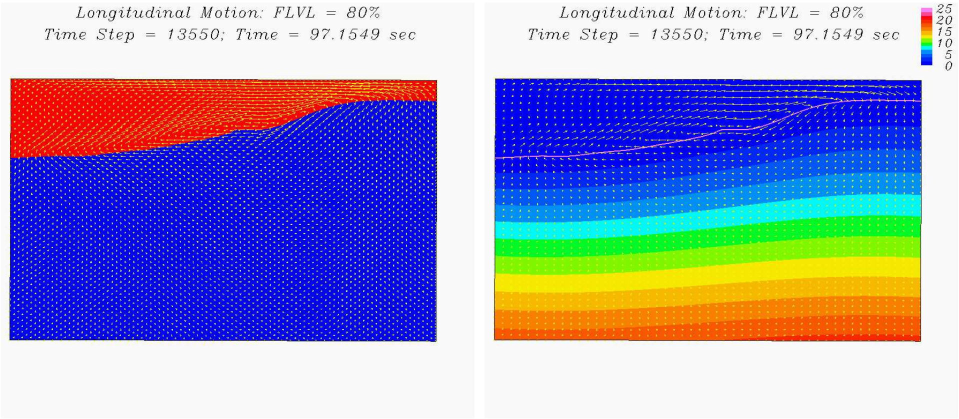

(c) Phase C: t/T = 13.55

Figure 5.42. 2D free surface, $\vec{V}, p$, Case 5

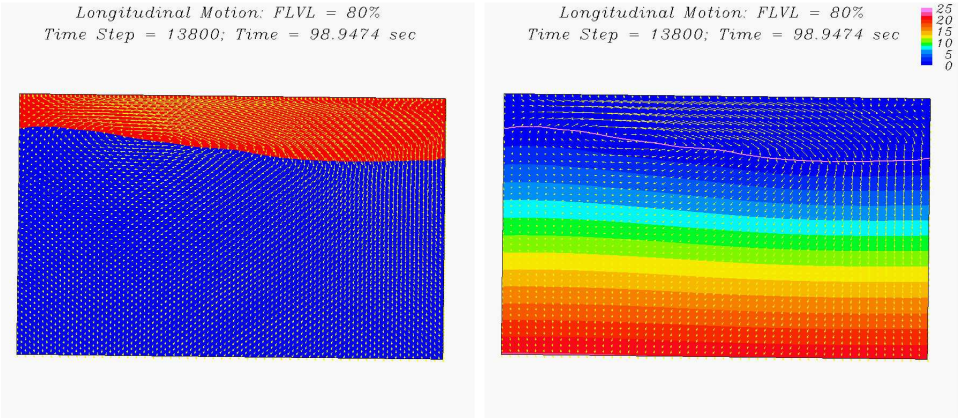

(d) Phase D: t/T = 13.80

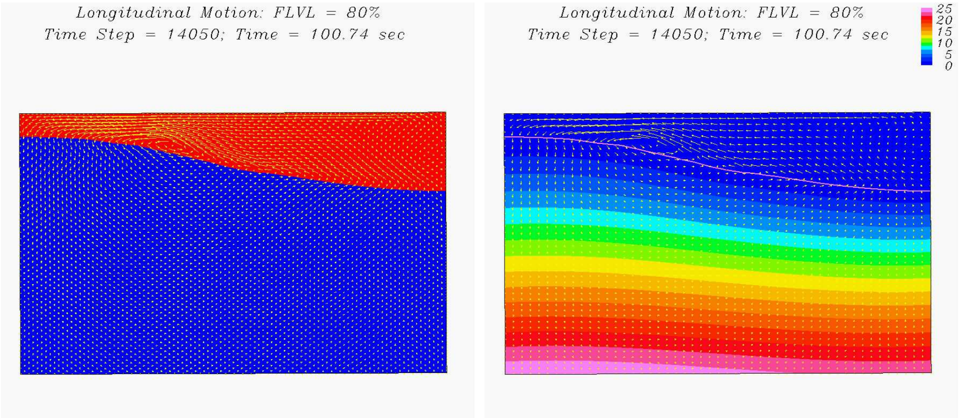

(e) Phase E: t/T = 14.05

Figure 5.42. (Continued)

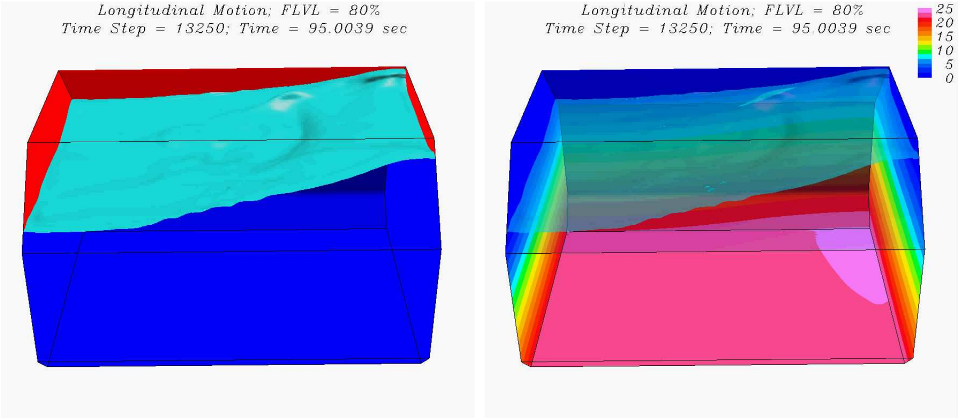

(a) Phase A: t/T = 13.25

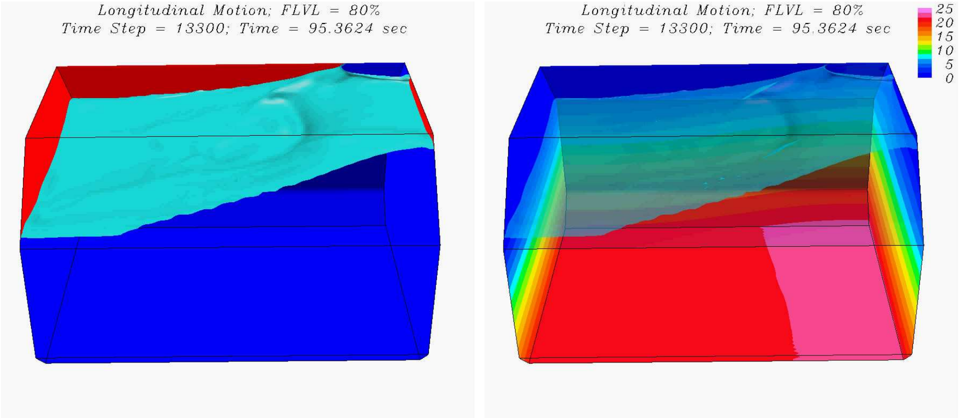

(b) Phase B: t/T = 13.30

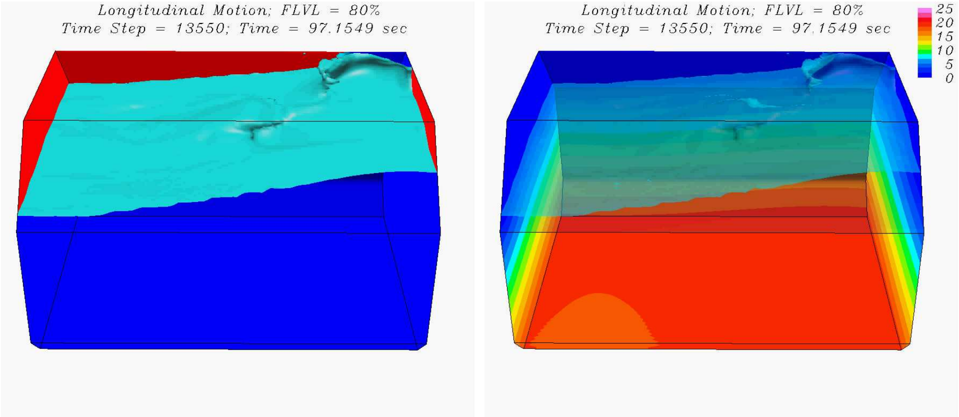

(c) Phase C: t/T = 13.55

Figure 5.43. 3D free surface and pressure contours, Case 5

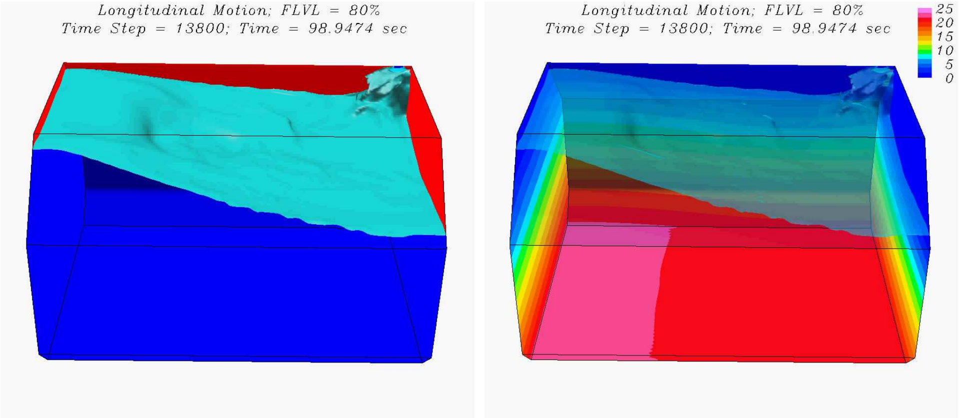

(d) Phase D: t/T = 13.80

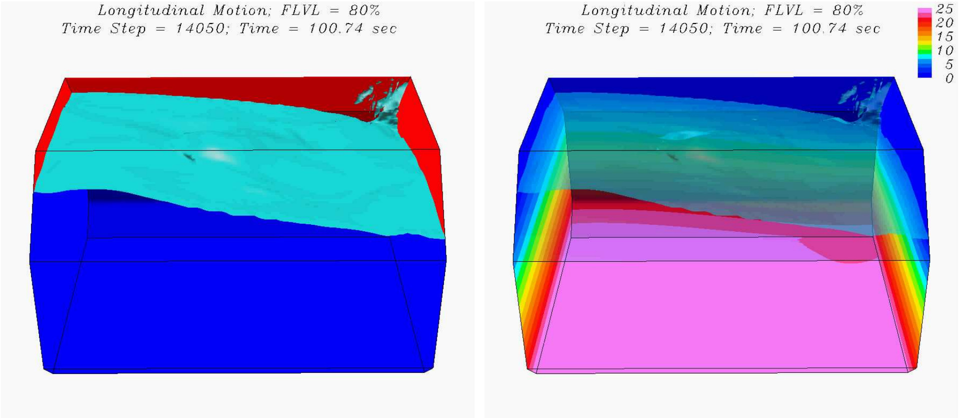

(e) Phase E: t/T = 14.05

Figure 5.43. (Continued)

a rapid rise of the water level and a sharp impact on the tank top wall at the sensor location Ch.7. Due to the three-dimensional instability, the flow becomes asymmetric after 7th sloshing periods with sloshing water impinging upon only one corner of the top wall as shown in Figures 5.43(b) and 5.43(c). It is also worthwhile to note from Figure 5.40 that both the measurement and numerical simulation clearly indicate the presence of small negative pressures following each impact. These negative pressure signals are very different from the pure hydrodynamic impacts observed in low filling level cases, and are due to the strong air-water interactions in the confined ullage space.

5.5.6. Case 6 - Longitudinal & 92.5% FLVL

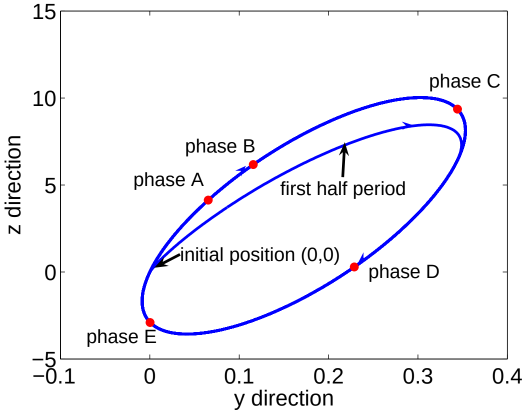

Figure 5.44. Tank motion trajectory, Case 6

Figure 5.44 shows the longitudinal motion trajectory (in yz-plane) of the LNG tank for Case 6 with a 92.5% filling level. In comparison with Cases 4 and 5, Case 6 has a relatively small horizontal motion while the vertical motion amplitude is significantly higher. In addition to the large amplitude vertical motions, the tank also experienced a large amplitude pitch motion with a maximum pitch angle of ±5.45°

. A modulation function was again applied for the first half cycle to eliminate the pressure oscillations caused by the impulsive start of the LNG tank motion. The 2D and 3D simulations were performed for 20 and 23 periods, respectively, and the wall pressures at selected sensor locations were recorded every time step to facilitate a direct comparison with the experimental data. At the 92.5% filling level, the free surface motion and high impact pressure regions are confined to the upper chamfer near the tank top. In view of this, the numerical grid was redistributed in the vertical direction to provide more accurate resolution of the impact pressures in the upper chamfer.

Figure 5.45 shows the 2D simulation results of impact pressures for the left and right pressure sensors corresponding to Ch. 3 on the top wall. Due to asymmetric tank motion, the pressure on the right sensor location is significantly higher than that on the left sensor location.

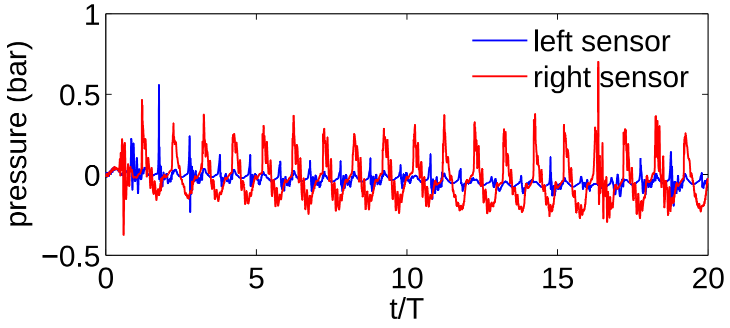

Figure 5.45. 2D pressure histories, Ch.3, Case 6

Figure 5.46 and 5.47 show the time histories of the measured and predicted pressures at Ch.3 on the top surface of the LNG tank for the 2D and 3D simulations, respectively. Note that Ch.3 and Ch.7 are mirror images on opposite side of the tank top wall. In general, the predicted impact pressures are in good agreement with the corresponding measurements. The 2D simulation gives less satisfactory predictions

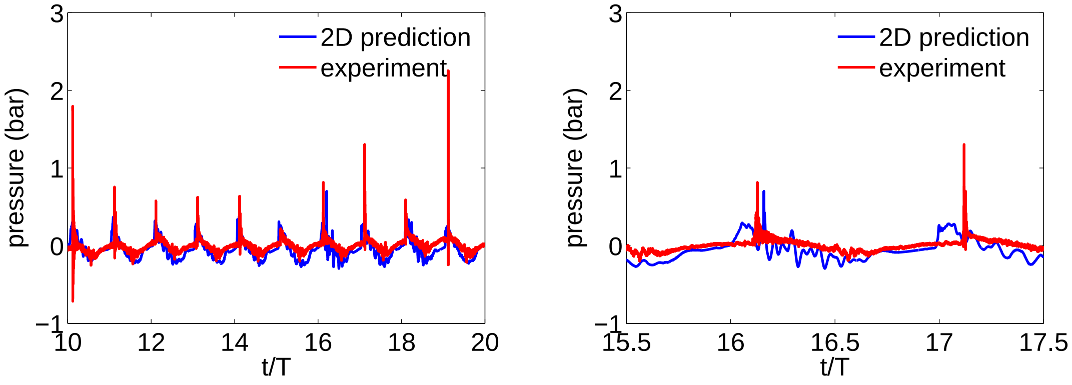

(a) 10 periods

(b) 2 periods

Figure 5.46. 2D impact pressure, Ch.3, Case 6

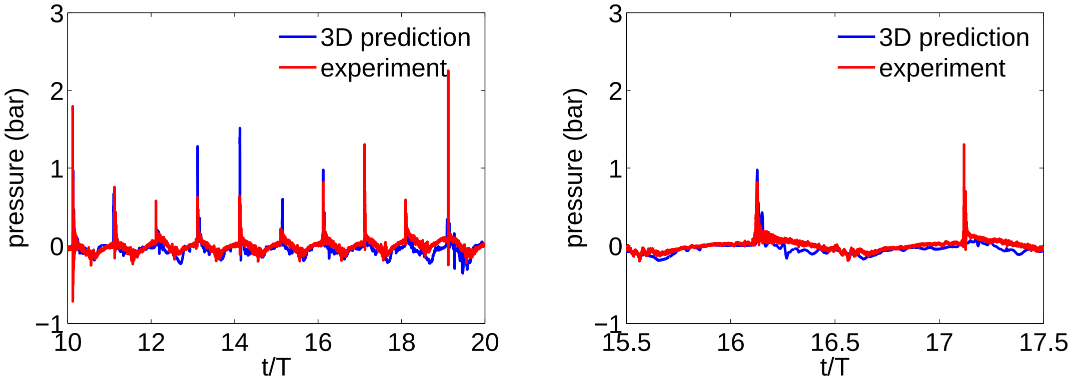

(a) 10 periods

(b) 2 periods

Figure 5.47. 3D impact pressure, Ch.3 (S12), Case 6

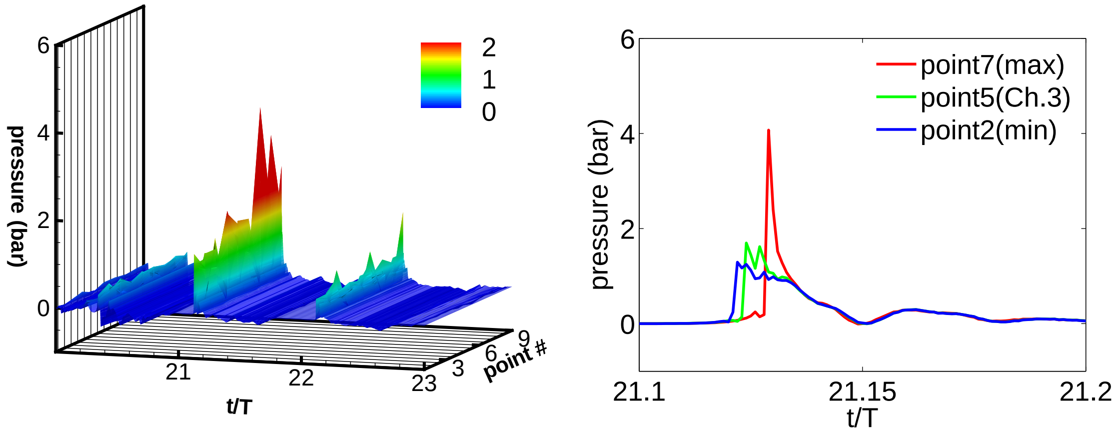

Figure 5.48. Impact pressures, the vicinity of Ch.3 (S12), Case 6

due to incorrect representation of tank geometry, but the result is still reasonable because the change of tank cross section is relatively small at the 92.5% fluid filling level. It is clearly seen that the peak impact pressure on the top wall is relatively low for this high filling case since the free surface motion is less violent in the confined ullage space. It is also interesting to note that the measured and predicted pressure histories exhibit a nearly symmetric pattern between two peak impacts. Furthermore, the wall pressure at Ch.3 is slightly below the atmospheric pressure between sharp pressure impacts. These pressure signals are caused by the combined hydrodynamic impact and air trapping effects which are very different from the pure hydrodynamic impacts observed in Cases 1-4 for the lower filling level cases. In the 3D simulations, the impact pressure is again highly localized as seen in Figure 5.48 with very strong variations between two adjacent grid points at the time of peak impact.

Figure 5.49 shows the predicted two-dimensional velocity field and pressure contours in the LNG tank at five different time instants $t/T = 16.10, 16.15, 16.40, 16.65,$ and 16.90. The corresponding free surface patterns and wall pressure contours for

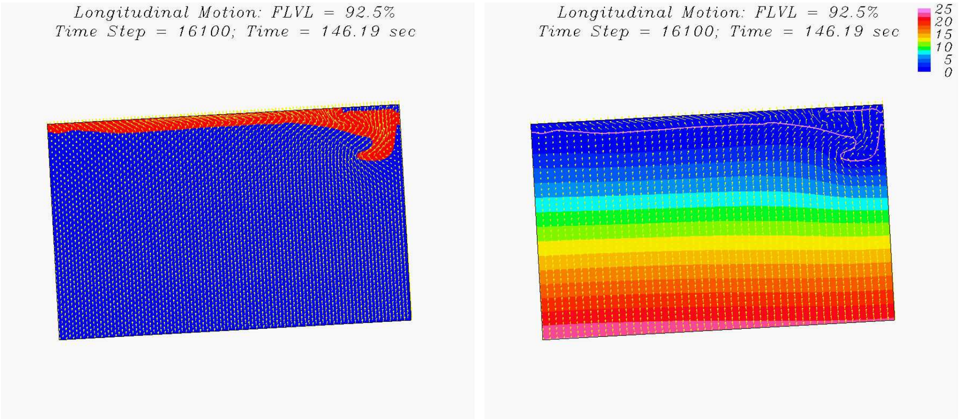

(a) Phase A: t/T = 16.10

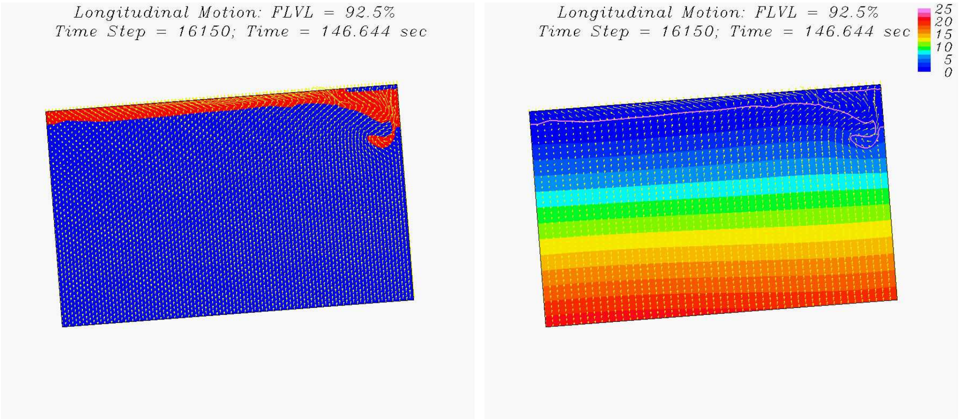

(b) Phase B: t/T = 16.15

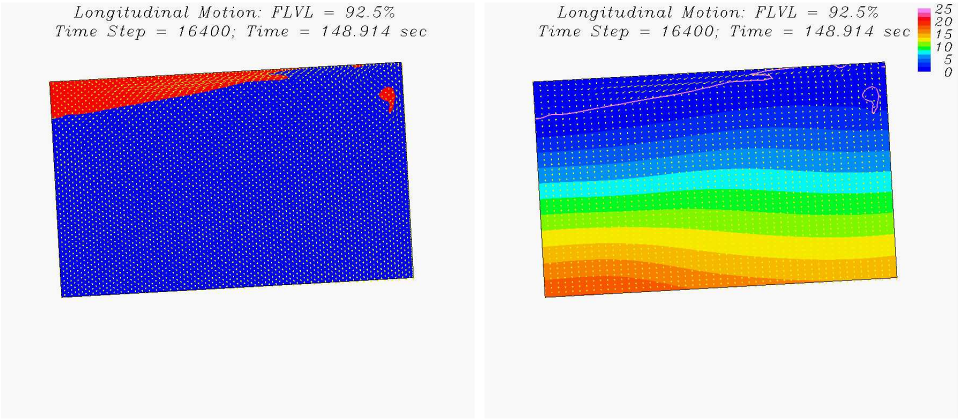

(c) Phase C: t/T = 16.40

Figure 5.49. 2D free surface, $\vec{V}, p$, Case 6

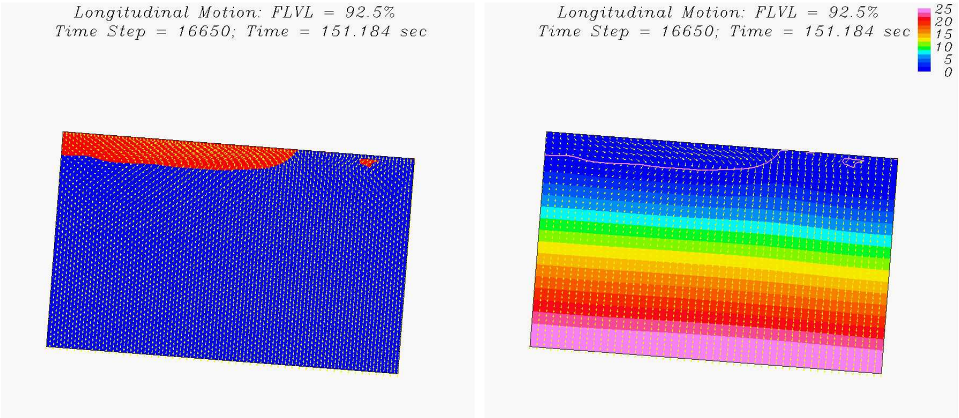

(d) Phase D: t/T = 16.65

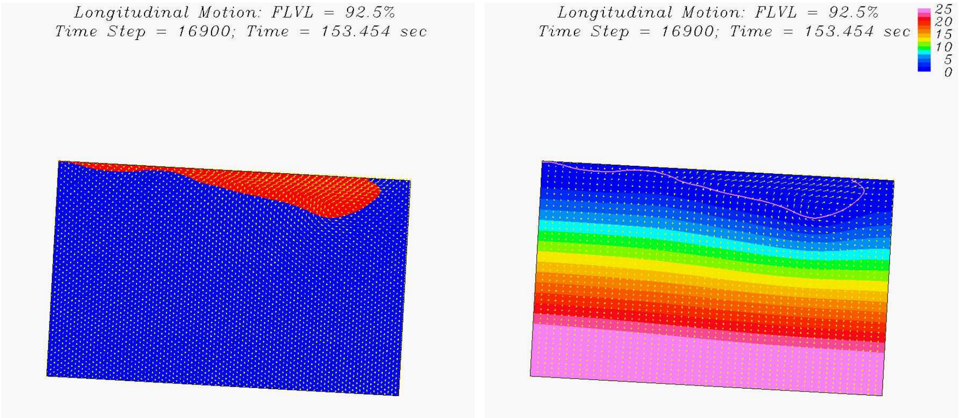

(e) Phase E: t/T = 16.90

Figure 5.49. (Continued)

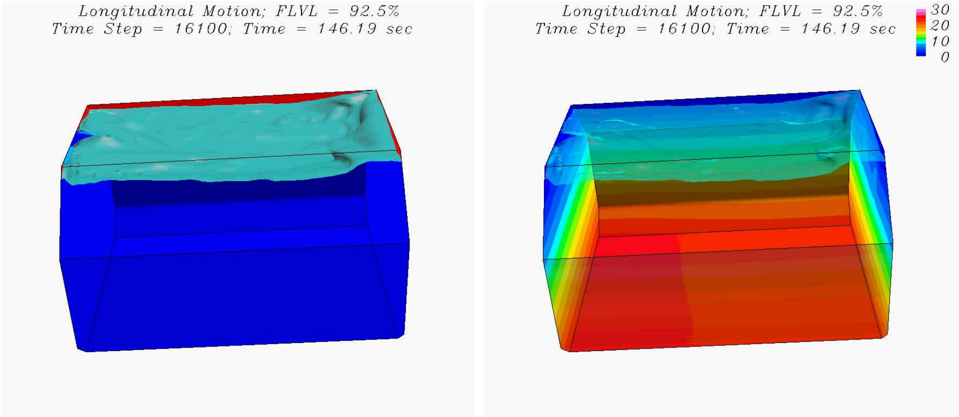

(a) Phase A: t/T = 16.10

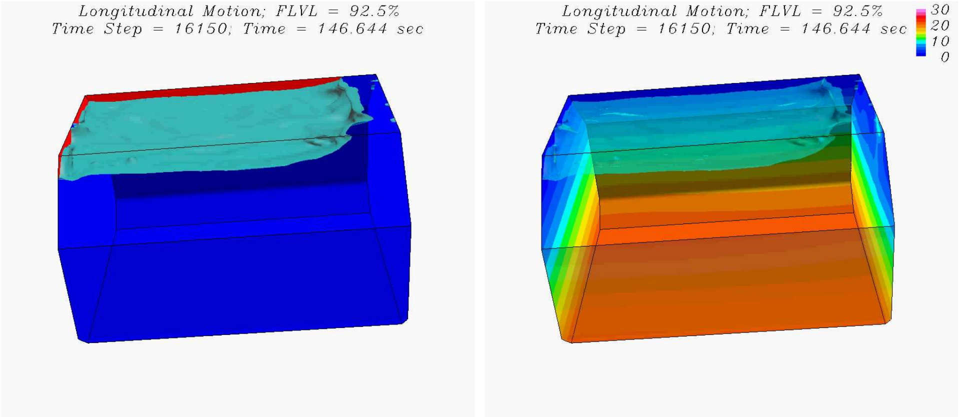

(b) Phase B: t/T = 16.15

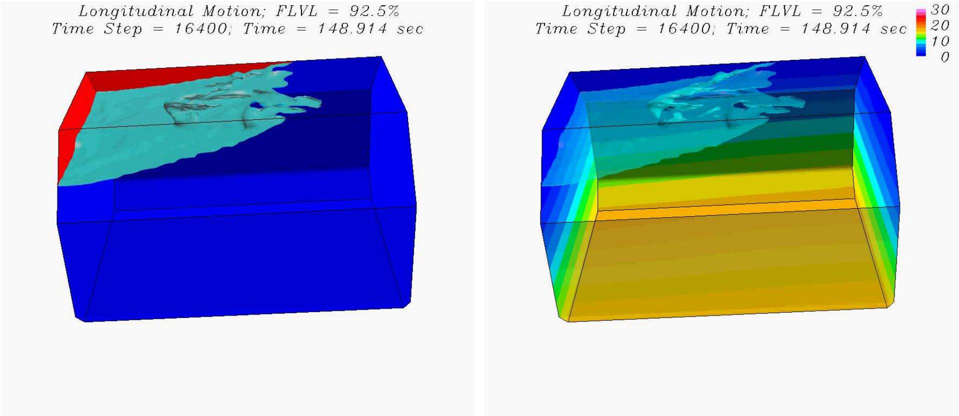

(c) Phase C: t/T = 16.40

Figure 5.50. 3D free surface and pressure contours, Case 6

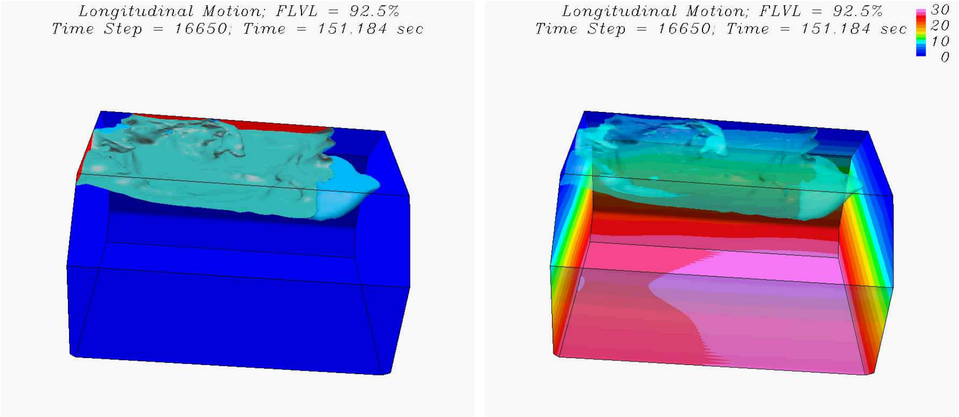

(d) Phase D: t/T = 16.65

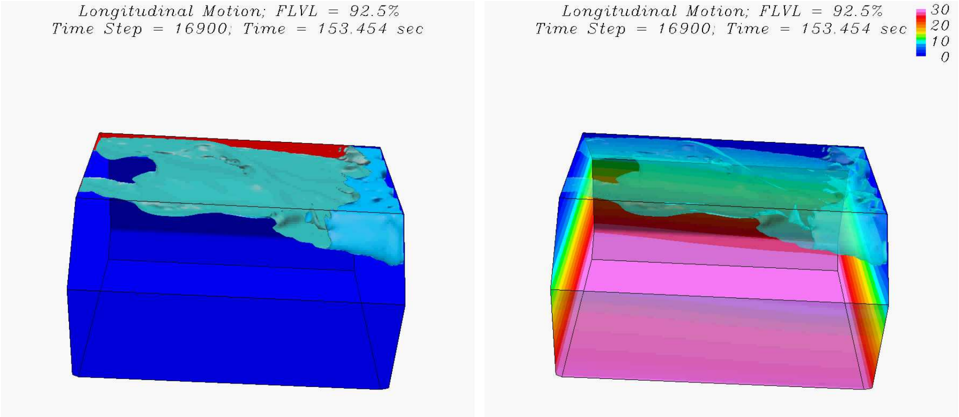

(e) Phase E: t/T = 16.90

Figure 5.50. (Continued)

three-dimensional case are shown in Figure 5.50 to facilitate a detailed understanding of the three-dimensional effects. For clarity, the five time are denoted by Phases A, B, C, D and E in the motion trajectory plots shown earlier in Figure 5.44. These five time phases were chosen based on the 3D impact pressure history in Figure 5.47(b) which shows that the maximum impact occurs between Phases A and B.

It is noted that the 2D and 3D flow patterns are very different at Phases A and E because the rectangular grid used in 2D simulation cannot account for the changing cross sectional area in the upper chamfer. It is also observed that the free surface motion for Case 6 is much less violent in comparison with those observed earlier for lower filling level Cases 1-4 since the ullage space is confined to a small region in the upper chamfer. During this selected period, the maximum impact pressure at Ch.3 occurs at $t/T = 16.128$ between Phases A and B. At Phase A ($t/T = 16.10$), the free surface level near Ch.3 is slightly below the tank top. The combined translational and rotational motion produced a rapid rise of the water level below Ch.3 (pressure sensor S12) and a sharp impact on the tank top wall between Phases A and B. It is also worthwhile to note that the pressure is relatively low at $t/T = 16.40$ since

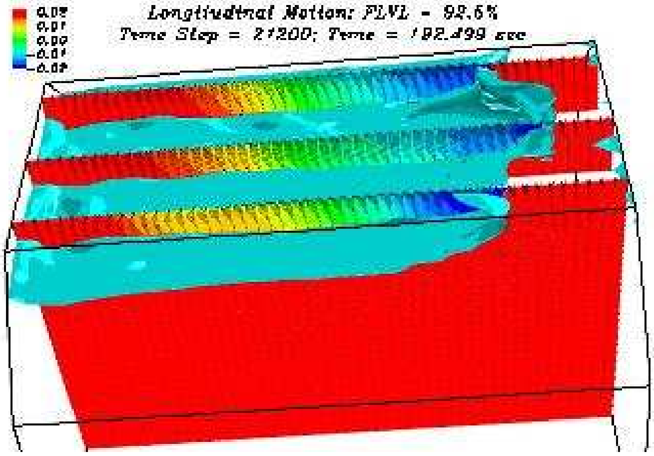

Figure 5.51. Pressure and velocity in the ullage space

the hydrodynamic pressure due to fluid momentum acts in the opposite direction of the gravity when the tank is near the top-right position. On the other hand, the wall pressure reaches maximum due to the combined hydrodynamics and hydrostatic pressure forces at $t/T = 16.90$ when the LNG tank reaches the lower-left position and begins it ascend to the equilibrium position.

In the present level-set Navier-Stokes method, both the water and air flows were solved simultaneously using a two-phase flow approach. In a single-phase model, the air pressure in the ullage space is assumed to be constant and equal to the atmospheric pressure. In the present two-phase flow simulation, however, the aerodynamic pressure in the narrow ullage space is strongly affected by the motion of the sloshing water flow. It is clearly seen from Figure 5.51 that the air velocity is much larger than the water velocity since the air is much lighter than water. The sloshing water was found to induce strong air motion which results in negative aerodynamic pressures in the ullage space. It is also interesting to note that some of the air bubbles were trapped near the tank corner for this high filling level case. However, the air cushioning effects of the trapped air cannot be properly accounted for in the present two-phase flow simulation since the air is assumed to be incompressible. In the future study, it is desirable to include the effect of ullage gas compressibility in order to determine the gas cushioning effects on the sloshing impact load of full scale LNG carriers.

5.6. Conclusion

In the present study, violent sloshing flows induced by the transverse and longitudinal motions of a membrane-type LNG tank were solved using the level-set Navier-Stokes method. The effects of turbulence were modeled using the Smagorinsky subgrid scale model in a Large Eddy Simulation (LES) approach. Both the water and air flows were solved simultaneously in the present two-phase flow approach to resolve the strong air-water interactions in the ullage space of the LNG tank. The predicted impact pressures for both the transverse and longitudinal motion cases are in good agreement with the corresponding experimental data although the peak pressures are somewhat underpredicted. For the 80% and 92.5% high filling level case, the free surface motion is less violent in the confined ullage space with lower impact pressures. Small negative pressures were observed for the high filling cases which can be attributed to the air trapping and strong air-water interactions in the narrow ullage space. Three-dimensional instability of sloshing flow was observed for both the transverse and longitudinal motion cases and confirmed by the experiments even though the tank excitation forces are strictly two-dimensional. In three dimensional simulations, it was also found that the highest impact pressure may not occur precisely at the sensor locations. The results show that the true peak pressure maybe appear at the vicinity of each sensor location.

CHAPTER VI

GREEN WATER SIMULATIONS

6.1. Introduction

The interaction between the extreme waves and floating structures is of primary concern in the design of offshore structures. Most of the earlier works employed potential flow theory without considering the viscous effects. In the past several years, however, the viscous-flow methods have been used by, among others, Park et al. (2001), and Chen et al. (2001, 2002) for the study of fully nonlinear free surface flow around coastal and offshore structures. In order to provide accurate resolution of viscous, nonlinear free surface flow around offshore structures, it is necessary to employ more sophisticated numerical methods and turbulence models capable of dealing with complex three-dimensional flow separation and fully nonlinear free surface waves.

In the wave runup simulations, we used the interface-tracking method in conjunction with a chimera Reynolds-Averaged Navier-Stokes (RANS) method for time-domain simulation of nonlinear waves around the platform. For the interface-tracking method, it is convenient to use separate body-fitted numerical grids for the structures and the ambient wave field. In the present chimera domain decomposition approach, the numerical grids around the platform remained fixed while the free surface grids are adjusted every time step to conform to the exact free surface. Since the submerged portion of the structures change continuously at different time instants, the interpolation between different chimera grid blocks were updated every time step to enforce conservation of mass and momentum across block boundaries over the entire simulation. In addition, an effective damping beach approach proposed by Chen and Huang

(2004) was implemented on the wave maker boundary to prevent the reflected waves from reaching the wave maker boundary. This enabled us to perform long-duration simulations without significantly increase the size of the computational domain. In the present study, the chimera RANS method of Chen et al. (2000, 2001, 2002) was generalized for time-domain simulation of fully nonlinear wave runup around the two-dimensional platform.

The level set method was incorporated into the chimera RANS method for the prediction of green water on offshore platforms. The governing equations were formulated in curvilinear coordinate system and discretized using the finite-analytic method of Chen et al. (1990) on a non-staggered grid. For the additional level set equations of evolution and re-initialization, we used the 3rd-order TVD (total variation diminishing) Runge-Kutta scheme (Yu et al, 2003b) for time derivative, and the 3rd-order ENO (essentially non-oscillatory) scheme for spatial derivatives. The final results clearly demonstrated that the level set method is capable of simulating violent free surface flows encountered in the green water simulations.

6.2. Wave Runup on 2D Platform

Ryu and Chang (2004) performed detailed velocity measurements in a laboratory flume at Texas A&M University for wave runup on a two-dimensional fixed rectangular structure based on the dimensions of a typical tension leg platform (TLP). The length and height of the model platform are 0.15 m and 0.31 m, respectively. The still water level is 0.105 m below the platform deck. Velocity fields in the vicinity of the structure were measured using the particle image velocimetry (PIV) technique for 8 phases per each wave period. Both instantaneous and phase-averaged quantities were obtained and analyzed. These PIV data provide an excellent database for the validation of the present numerical method.

In the present chimera domain decomposition approach for platform wave runup

(a) Chimera grid with structure; t/T = 20.375

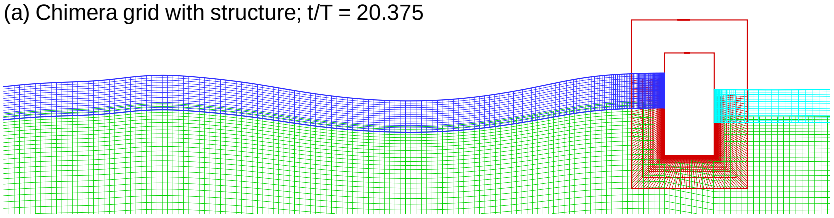

(b) Wave tank grid without the structure; t/T = 20.375

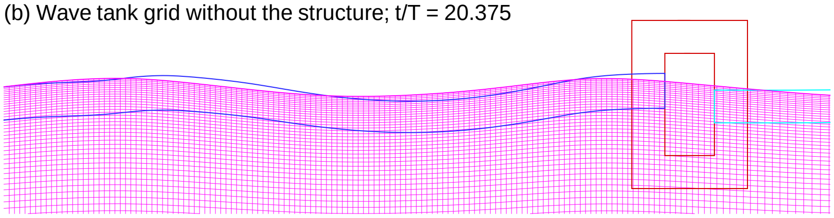

(c) Chimera grid with structure; t/T = 20.875

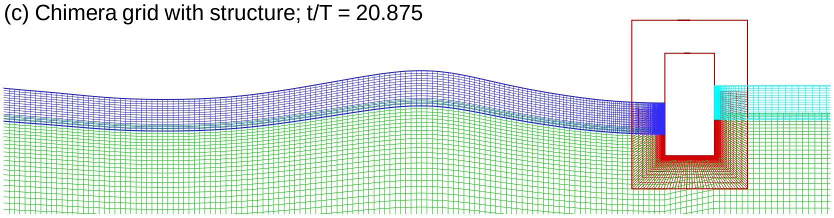

(d) Wave tank grid without the structure; t/T = 20.875

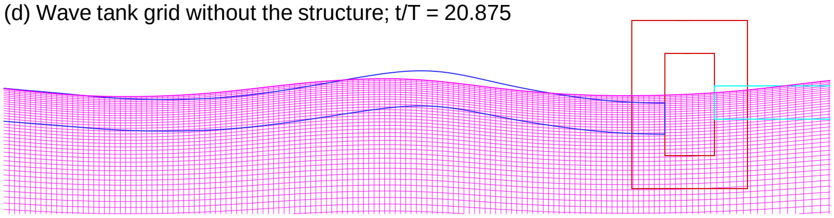

Figure 6.1. Chimera grid for wave runup simulation

simulation, the solution domain is divided into several computational blocks as shown in Figure 6.1 to provide appropriate resolution of the platform boundary layers, wakes, as well as the nonlinear free surface waves. Figure 6.1(a) and 6.1(c) shows the chimera grid block structures around the platform at t/T = 20.375 and 20.875, respectively. For completeness, the wave tank grids at the same time instants are also shown in

Figure 6.1(b) and 6.1(d). These wave tank grids are not linked to the other grid blocks and are used solely for the implementation of absorbing beach in front of the wave maker. For long-duration simulations over many wave periods, it is well known that the wave reflected by the platform will propagate back to the wave maker boundary and interfere with the incident wave field. In the present study, a new absorbing beach approach developed recently by Chen and Huang (2004) has been implemented to prevent the reflected wave from returning to the wave maker. In this absorbing beach approach, the wave tank grids shown in Figure 6.1(b) and 6.1(d) were used to allow concurrent computation of the incident wave field without the presence of the offshore structure. This enables us to determine the exact pattern of the reflected wave since both wave fields with and without the structure were computed simultaneously at every time step. A damping function was then used to absorb the reflected waves so that the time-domain simulation can be continued for many wave periods without wave reflection from the wave maker.

In the present wave runup simulations, the incident wave field was generated using the higher order nonlinear wave theory of Cokelet (1977). The free surface grid blocks are updated at every time step to follow the instantaneous free surface wave elevation. Furthermore, nonlinear dynamic free surface boundary condition is imposed on the exact free surface for accurate prediction of the fully nonlinear wave field. It should also be noted that the platform grid covers the entire platform surface including the dry deck area. Moreover, the platform grid remains fixed during the entire simulation even though the submerged section changes with instantaneous wave elevation. This not only simplifies the grid-generation process, but also eliminates undesirable grid distortion which typically occurs in the simulation of large amplitude wave motions.

Simulations were performed for wave runup on the two-dimensional platform used

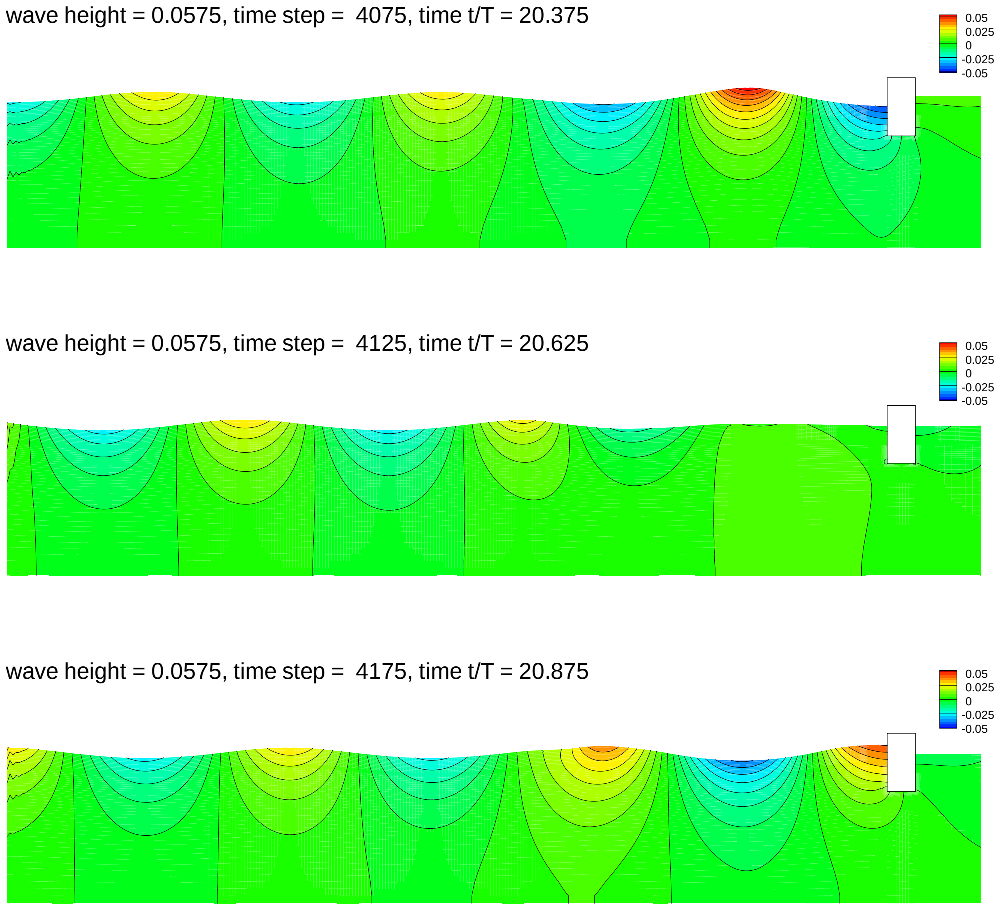

Figure 6.2. Wave elevation and pressure contours

in the experimental study of Ryu and Chang (2004) with an incident wave height of H = 0.0575 m. Figure 6.2 shows the computed free surface wave elevation and pressure contours at t/T = 20.375, 20.625, and 20.875, respectively, for the H = 0.0575 m case. The superposition and cancellation of the incident and reflected waves at different time instants can be clearly seen from this figure. The present simulation results also clearly demonstrated the effectiveness of the new absorbing beach approach as the simulation was continued for more than 20 wave periods without any distortion in incident wave field.

Figure 6.3 shows the time history of the wave elevation in front of the structure.

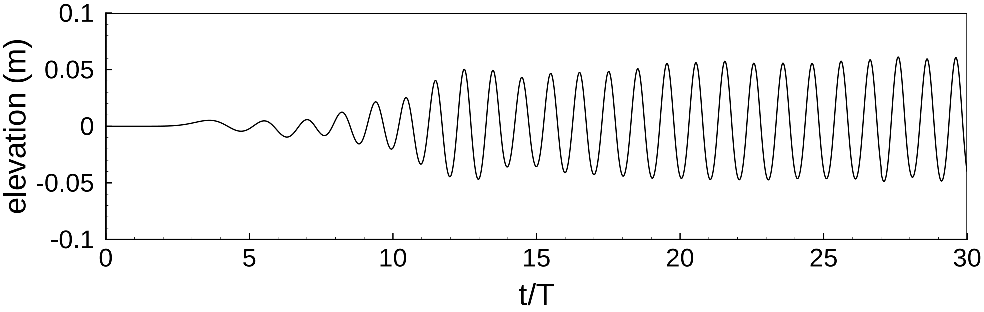

Figure 6.3. Time history of wave elevation

It is seen that the first wave reaches the structure after three wave periods since the wave maker is located about three wavelengths upstream of the model TLP. Note that the relatively large waves occurred around the 12th-13th wave periods followed by a transition period with significant fluctuation in wave height. The flow attained a nearly periodic pattern after about 20 wave periods. It is quite clear that the absorbing beach in front of the wave maker successfully absorbed all the waves reflected from the structure so that the same incident wave can be maintained for long duration simulation with a rather small solution domain.

Figure 6.4 shows the predicted velocity vectors and the corresponding vorticity

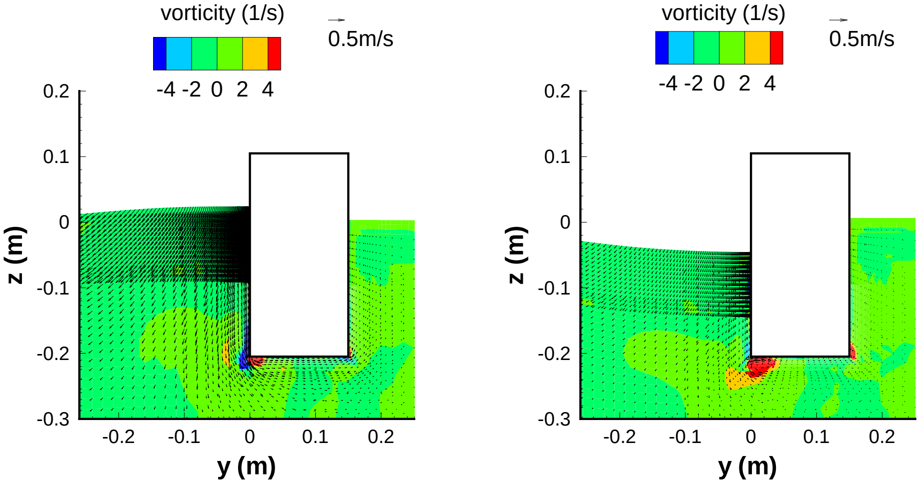

(a) t/T=20.125

(b) t/T=20.375

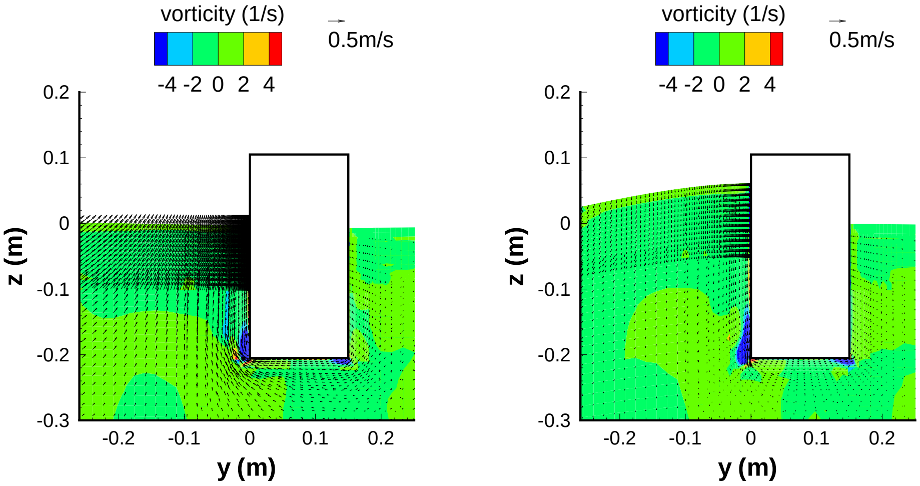

(c) t/T=20.625

(d) t/T=20.875

Figure 6.4. Velocity and vorticity around the platform

contours at t/T = 20.125, 20.375, 20.625 and 20.875, respectively. At t/T = 20.125, the wave-induced current is moving downward and produces a strong counterclockwise vortex on the platform bottom surface adjacent to the weather side corner. Another weaker counterclockwise vortex was also observed on the lee side. The wave reaches its lowest elevation and begins to move upward around t/T = 20.375. At t/T = 20.625, the upward current velocity reaches a maximum value and a pair of clockwise vortices were induced around the sharp platform corners. The wave in front of the platform continue to move upward until the maximum runup is reached at t/T = 20.875. It is also worthwhile to note that the water elevation on the lee side of the platform changes only slightly since the platform draft is relatively deep with negligible wave transmission. The predicted velocity vector plots are in very good agreement with the corresponding PIV measurement of Ryu and Chang (2004) at the same phases.

After successful validations of the chimera RANS method for two-dimensional platform configurations, the method was further generalized for time-domain simula-

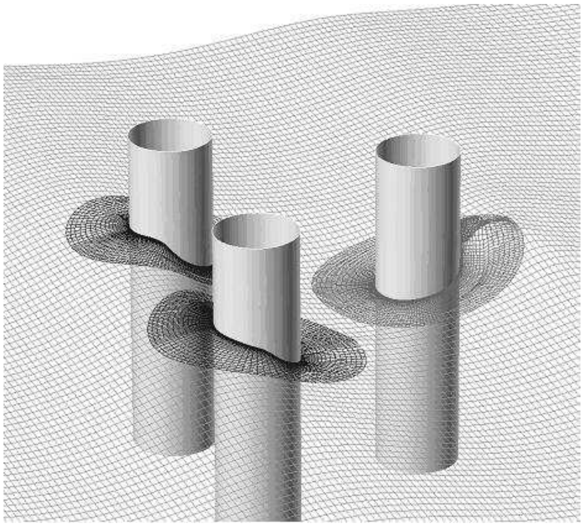

Figure 6.5. Chimera grids around vertical cylinders

tion of wave runup around single and multiple vertical cylinders which are common structural elements of TLP and other types of offshore structures. Figure 6.5 shows the numerical grids around three vertical cylinders. In the chimera domain decomposition approach, it is convenient to use overset grid system with body-fitted cylindrical grids embedded in the background rectangular grids. For the fully nonlinear waves considered here, the numerical grids are updated every time step to conform with the exact free surface.

Time-domain simulations were also performed for wave diffraction around three vertical cylinders. The center-to-center spacing between the two front cylinders is 2.96 D, where D is the diameter of the cylinder. The third cylinder is placed at 2.56 D (center-to-center) downstream of the two front cylinders. Figure 6.6 shows the predicted wave patterns at t/T = 0.55, 0.60, 0.64, 0.66, 0.68 and 0.70. The incident wavelength specified in the present simulation is /D = 5.62 and the incident wave height is H/D = 0.30. The simulation results clearly indicated the presence of strong interactions between the two front cylinders in side-by-side arrangement. It is also seen that the wave runup on the downstream cylinder is almost completely out-of-phase in comparison with the front cylinders since the wavelength is about twice of the cylinder spacing. Moreover, the wave diffraction pattern on the downstream cylinder is significantly different from that of the single cylinder case. This is clearly due to the strong interactions among the three vertical cylinders.

6.3. Green Water on 2D Platform

The experimental measurement of velocity fields of a plunging wave impacting on a platform was investigated recently by Ryu and Chang (2005). A new technology called bubble image velocimetry (BIV) was used to measure the velocity in the

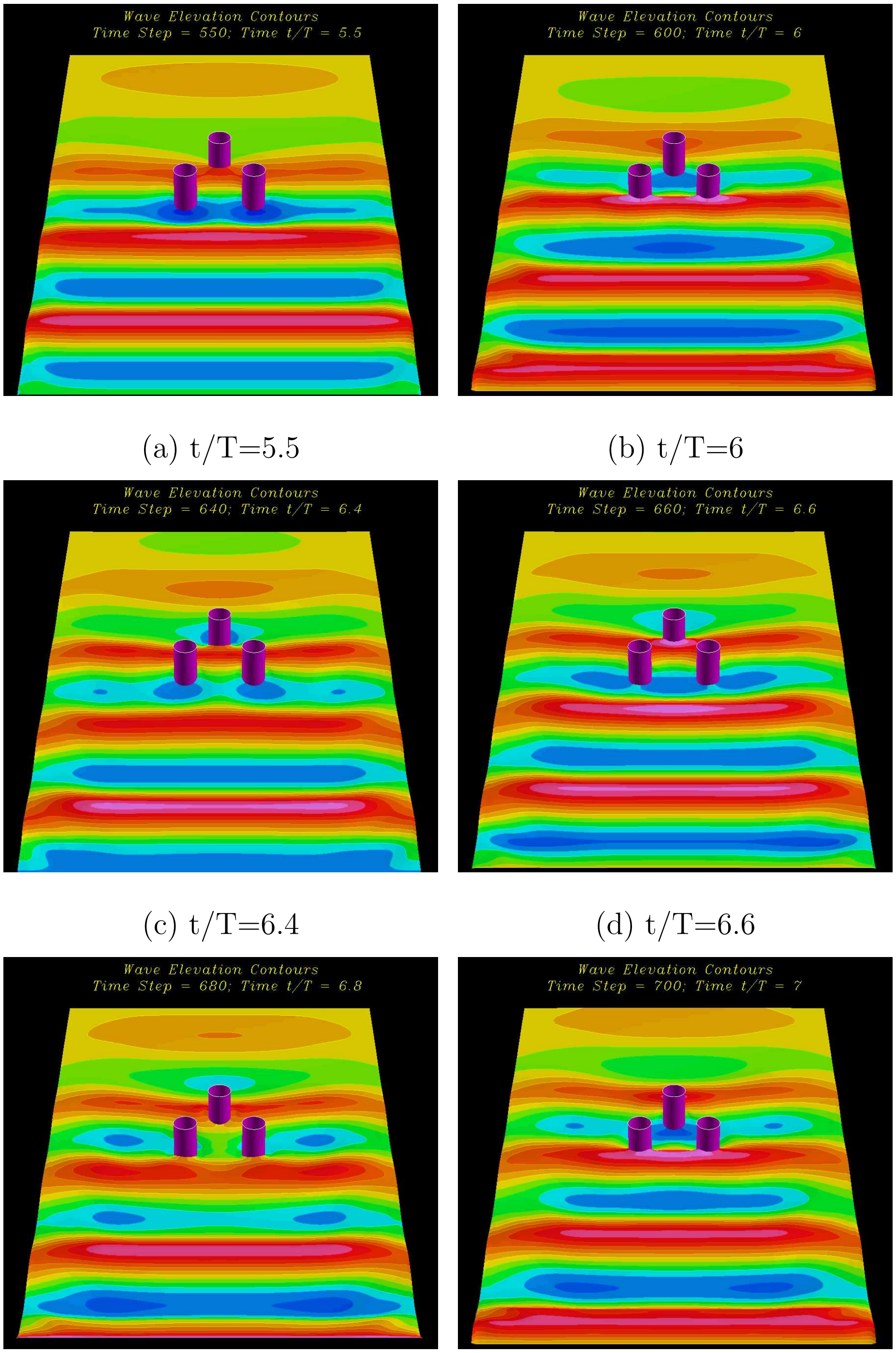

(a) t/T=5.5

(b) t/T=6

(c) t/T=6.4

(d) t/T=6.6

(e) t/T=6.8

(f) t/T=7.0

Figure 6.6. Free surface pressure contours around cylinders

aerated region and the associated green water. The experiments were performed in a glass-walled wave tank which was described in details in Ryu (2005). The water depth was kept constant at h=0.8m. A flap type wave maker was installed at one end of the wave tank and a sloping beach was at the other end in order to absorb the wave energy and reduce reflection. The platform was located at 21.7m from the wave maker. A plunging breaker was generated by the wave focusing method. The wave train consisted of waves with various frequencies ranging from 0.7Hz to 1.3Hz. With the superposition of different wave frequencies and some trials and errors, a plunging breaker was breaking at a desired location right in front of the structure. More details can be found in Ryu (2005). Figure 6.7 shows the sketch of the model structure, coordinate system and experimental field of view (FOV). The small window in numerical grid is the area to be compared with FOV1 in the model structures.

Because of its high nonlinearity, the plunging breaker is difficult to be generated

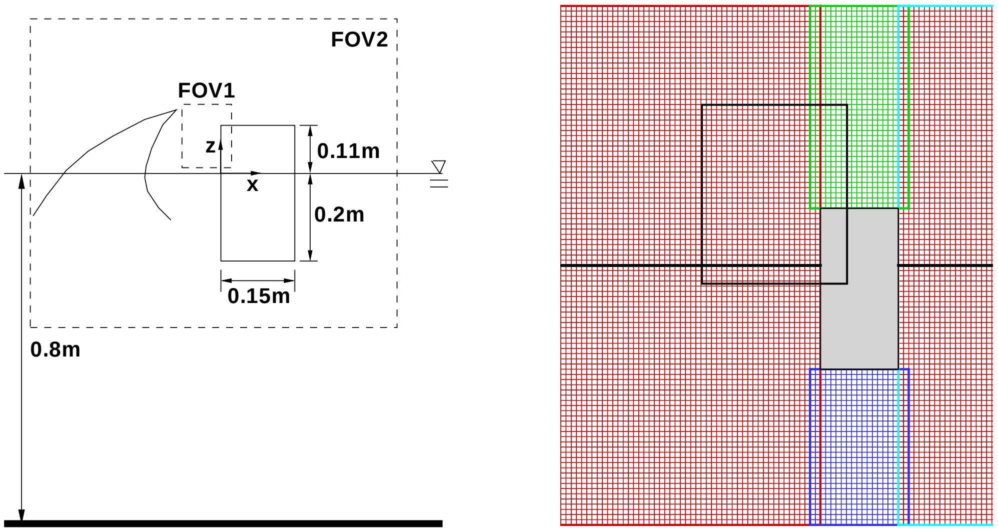

Figure 6.7. The model structure and numerical grids

in the numerical wave tank. Longuet-Higgins and Cokelet (1976) performed the first numerical simulation of breaking wave using the boundary integral method. Chen, Zaleski and Li (1999) described plunging breakers by solving the classical, incompressible, two-dimensional Navier-Stokes equation. They presented the plunging breaker which was developed from the initial condition based on the third order Stokes wave. The instability of this steep Stokes wave led to wave breaking. A similar initial wave is used in this study. The initial wave profile is as follows:

$$\eta(y, t = 0) = \frac{1}{2\pi}\left[\epsilon\cos(2\pi y) + \frac{1}{2}\,\epsilon^2\cos(4\pi y) + \frac{3}{8}\,\epsilon^3\cos(6\pi y)\right]$$

Here, η is the wave elevation. $\epsilon(= 2\pi a/\lambda)$ is the wave steepness. y denotes the horizontal coordinate.

Figure 6.8 shows the snapshots of a plunging breaker in a single numerical wave tank. The tank is 3m$\times$2m with a 301$\times$201 uniform grid. The characteristic length is set to 1 m and Froude number is set to 1. Reynolds number is 3.17×10^6. The simulation is performed with $\epsilon = 0.7, \lambda = 1.5, \Delta t = 0.006$. The wave steepness is much higher than $\pi/7$, the steepness value threshold by the nonlinear Stokes wave theory. Chen et al. (1999) used a lower wave steepness,$\epsilon = 0.55$, to generate plunging breakers. This steepness is too large to be generated in laboratory. We will reduce this value in the future by introducing the particle level set method, which is a hybrid method of MAC and level set. Enright et al. (2002) discussed this method in details. At t=0, the initial wave has its crest at y=1.5 and it moves from the left to the right. The solid wall boundary conditions are imposed on left and right sides of tank. The velocity extrapolation boundary condition is applied at the air-water interface, i.e. $\vec{V}\cdot\nabla\phi = 0$. As the wave propagates toward the right, the crest of wave becomes more and more asymmetric. The quick movement of the crest results in a jet curling over part of the wave trough. The jet becomes stronger along the

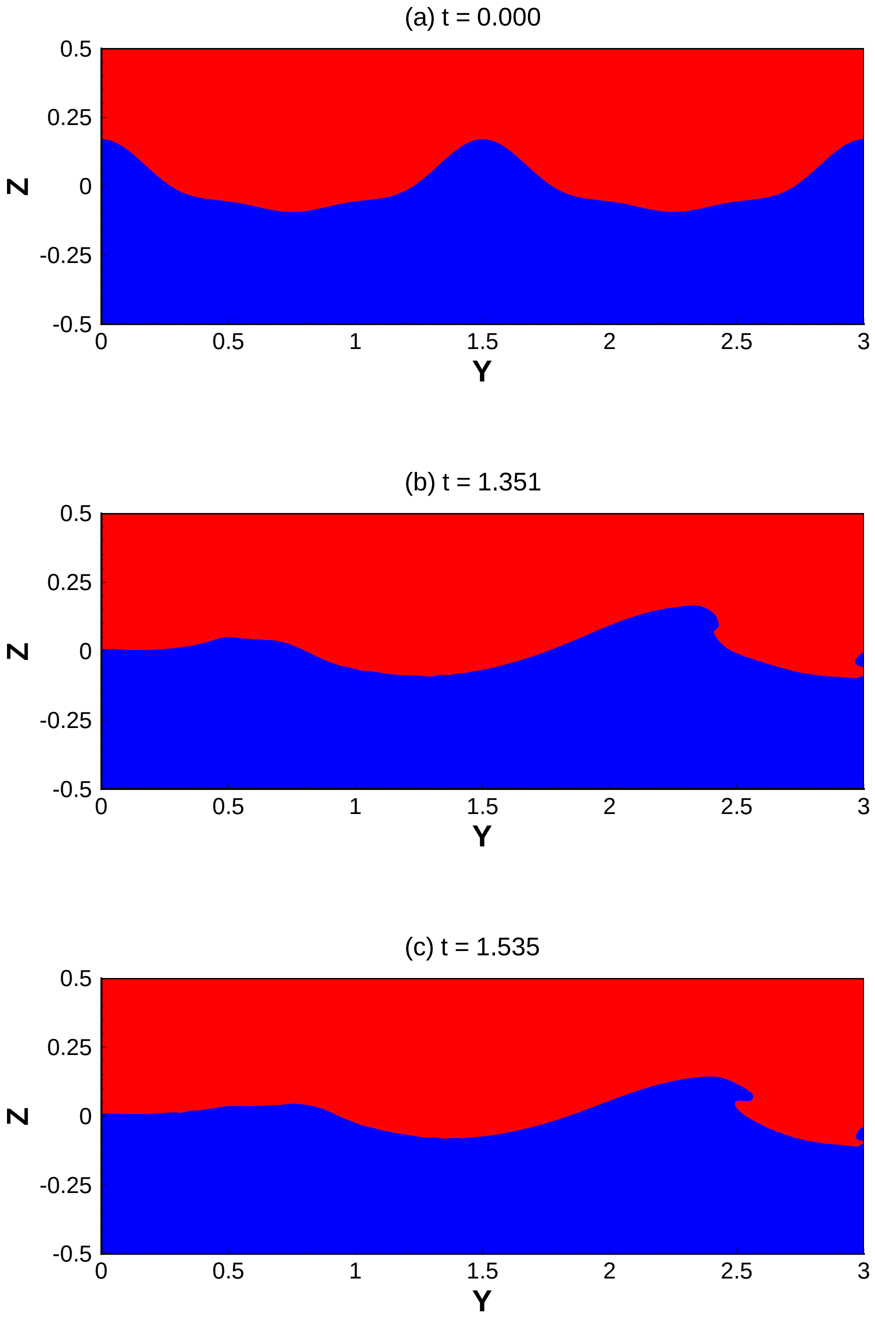

Figure 6.8. Snapshots of a plunging breaker

(d) t = 1.842

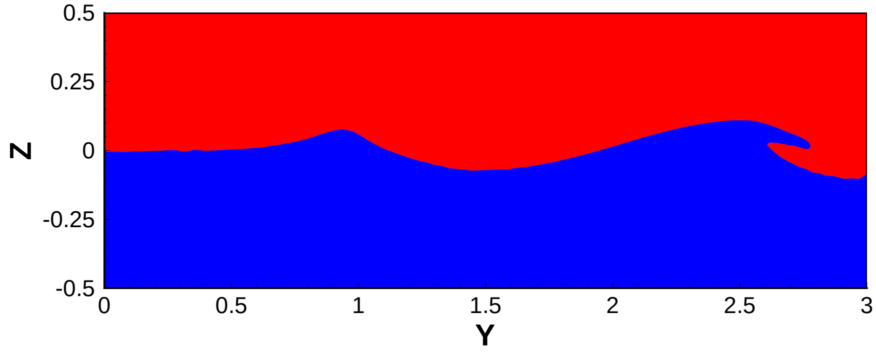

(e) t = 2.272

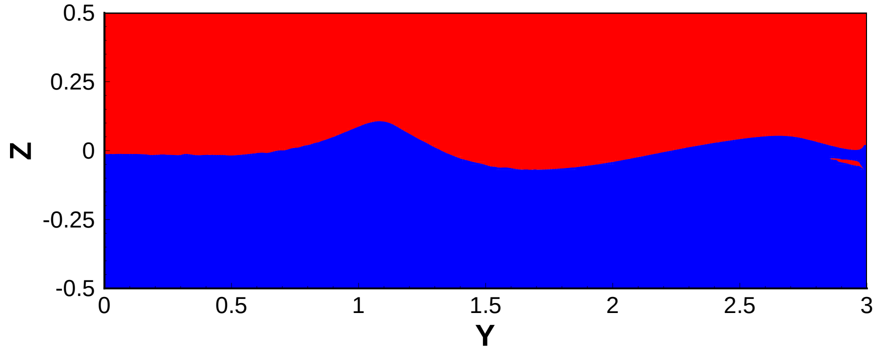

(f) t = 2.579

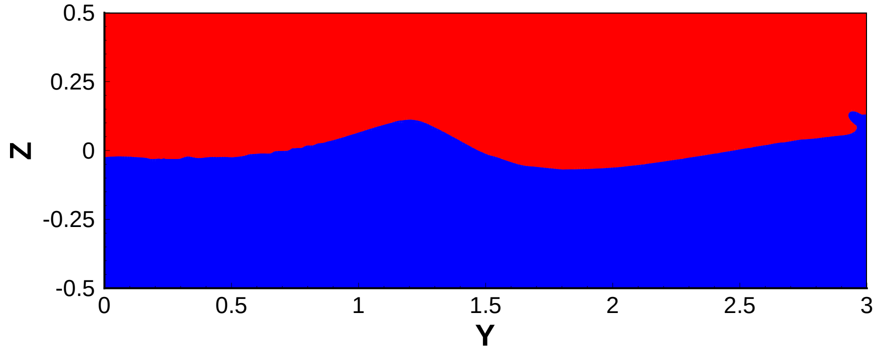

Figure 6.8. (Continued)

wave propagation and eventually impinges on the right side wall. Meanwhile, air is entrapped in a big pocket. After the impingement, the jet is split into two parts. One is splashing up and the other one is pushed to move downward. The downward flow produces a big vortex under the free surface near the wall. This vortex also appears in two-dimensional green water simulation.

After the plunging breaker is generated in the numerical wave tank, The green water simulation is performed under the same conditions by placing a platform in the middle of the wave tank. The platform is surrounded by four rectangular grids which is also shown in Figure 6.7. The horizontal black line is the initial still water level. The black frame is corresponding to FOV1 in the model test. The platform size used in the numerical simulation is identical to the model structure. The initial wave is generated with wavelength at 1.5 m and wave steepness at 0.7. This highly nonlinear wave breaks right in front of the structure. The structure position is adjusted to obtain good agreement with the measured results.

Figure 6.9 shows the comparison of the predicted and measured free surface patterns and velocity vectors at three different phases. The simulated wave breaks right in front of the structure. The first two pictures represent the moment when the jet front hits the leading edge of the structure. There is a big bubble entrapped by the plunging breaker which is shown in both numerical and experimental results. After the jet impinges on the platform, the wave momentum splits the water into two parts. Some water splashes upward with strong vertical velocity on the front face of the platform. There is also some water which moves downward along the structure edge. This creates a vortex at around $z = 0$. The second comparison indicates the vortex clearly. The vortex position is a little lower in numerical simulation than that in experimental measurement. After a certain duration, the wave front is pushed continuously upward onto the deck by the wave momentum. The overtopping wave

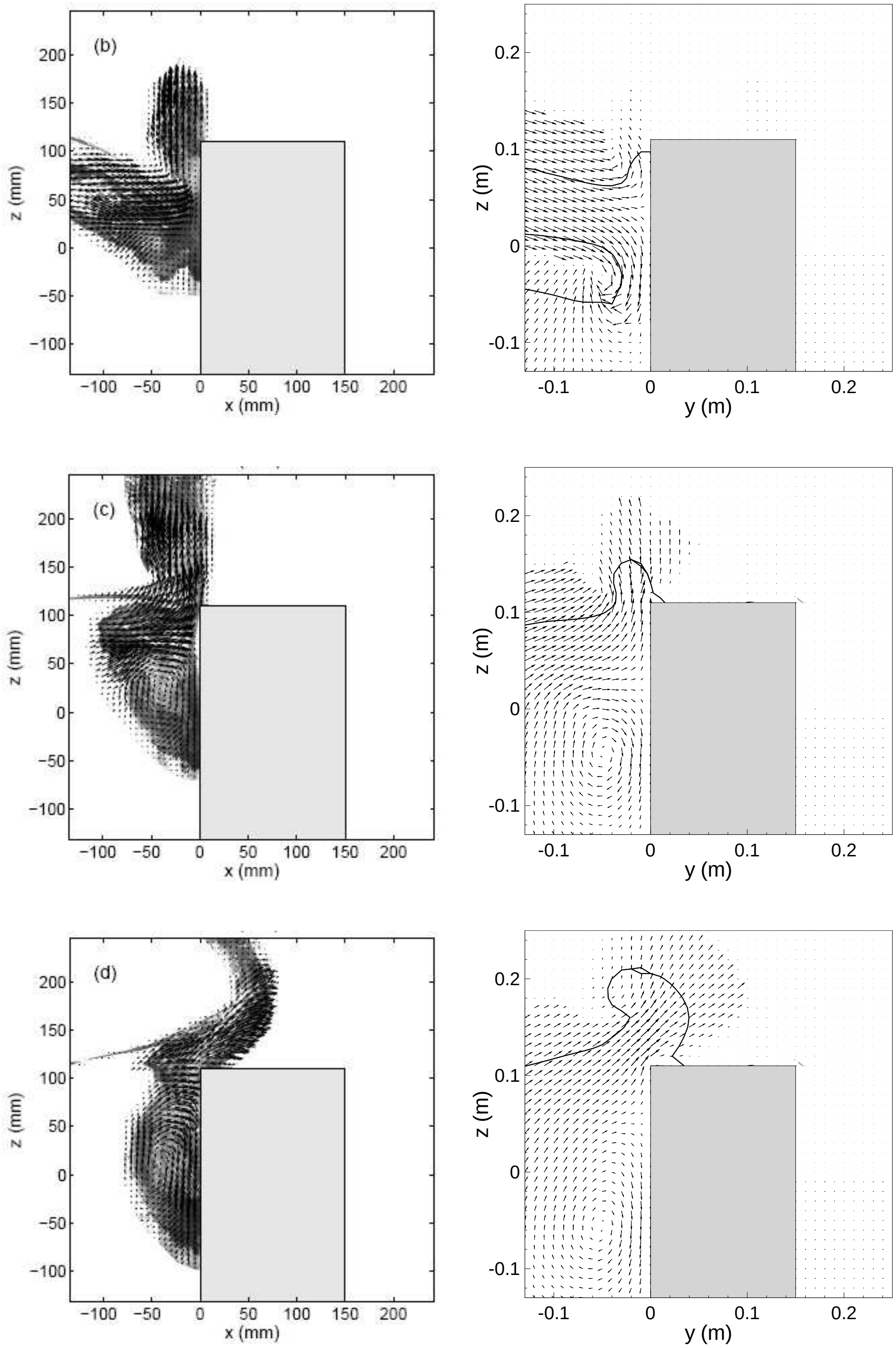

Figure 6.9. Comparison of green water effect on 2D platform

rushes across the platform deck and produces large green water load which may cause significant damages to offshore structures in areas that are not designed to withstand the impact load. The third comparison clearly shows that the predicted free surface patterns and flow directions are in close agreement with the corresponding measurements.

Another application of level-set RANS method is the simulation of wave impact on the deck of a large platform as shown in Figure 6.10. The center of the platform is located at (4, 0.08), and the dimension of the platform deck is 1.0 0.03. The incident wave height is 0.15 and the wave length is 2.0. It can be seen from Figure 6.10 that the wave was about to break before hitting the platform deck. In addition to the water overtopping on the platform deck, the wave crest was also found to slam on the bottom of the platform at certain time instants. The wave slamming is expected to produce large uplift force which may damage the platform deck structure. It is also clearly seen that the green water on top of the platform rushes through the deck and falls back into the ocean on the lee side of the platform. The present simulation results clearly demonstrated the capability of the level set method in dealing with violent free surface motions including both the green water and wave slamming effects. In the next phase of research, the level set method will be generalized to provide accurate resolution of air-water interface around three-dimensional offshore platforms. In addition, a more robust numerical wave maker will be implemented to enable the generation of highly nonlinear waves as observed in the present experimental investigations.

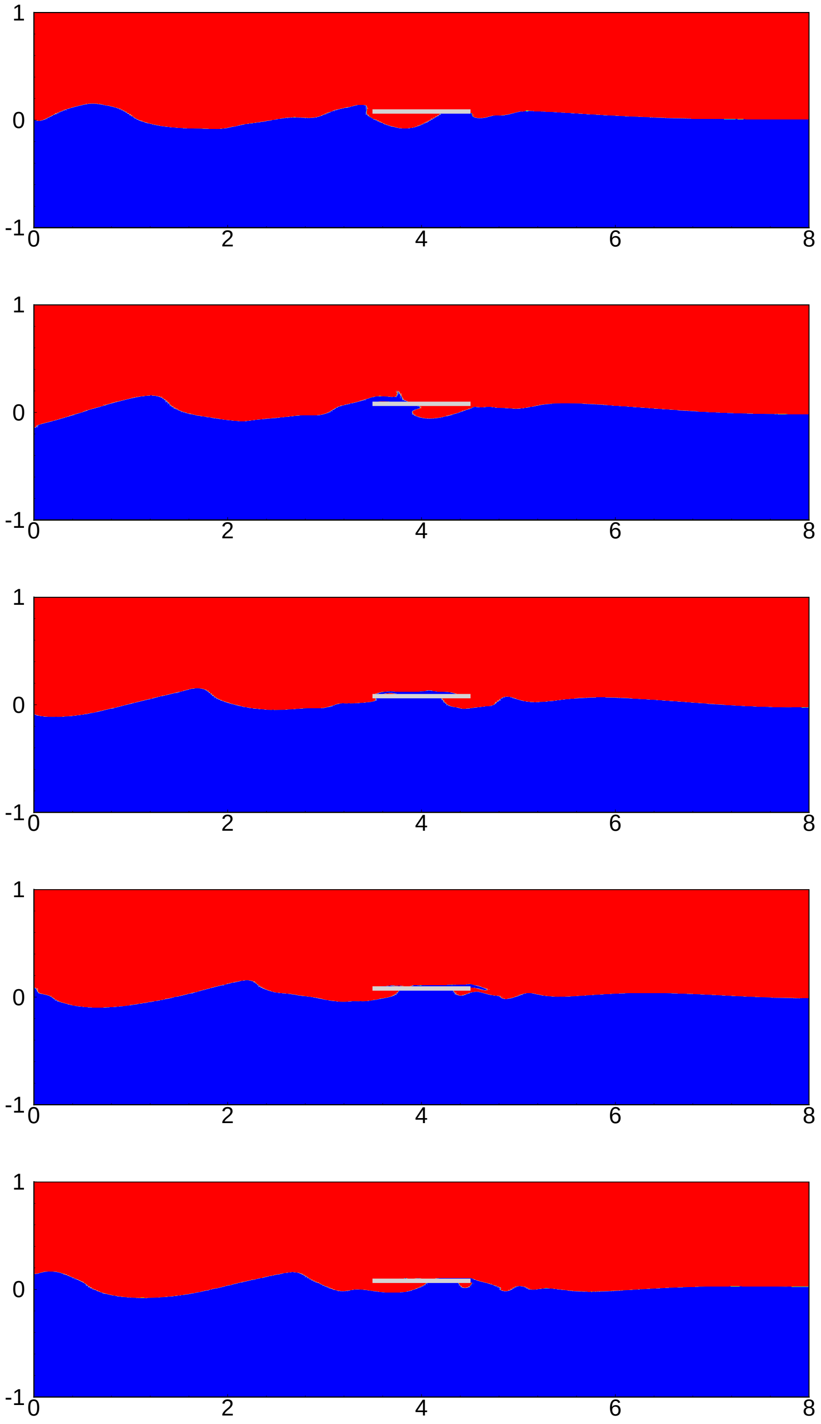

Figure 6.10. Green water around a platform deck

6.4. Green Water on 3D Platform

In addition to the two-dimensional green water simulation described above, numerical simulations were also performed for a rectangular platform to examine the edge effects around a 3D platform. The three-dimensional model test is scheduled for the future project. This three-dimensional result is a preliminary part of the project.

Figure 6.11 shows the three-dimensional numerical grids for 3D green water simulation. The grid consists of six computational blocks with a total of 916,057 grid points. Chimera domain decomposition technique is applied to generate appropriate grids. The structure is surrounded by five grids, two cubic grids on top and bottom and three cuboid grids with holes in middle. These near-field boundary-fitted grids are embedded in a Cartesian grid block representing the wave tank. The tank size is 0.8m × 4m × 2m. The size of the rectangular platform is 0.15m × 0.15m × 0.31m, and the platform deck is located at 0.105m above the still water level. The incident wave is generated by flap type wave maker again using the higher order nonlinear wave theory of Cokelet (1977). The wave length is set to 1.0 m and wave height is set to 0.2

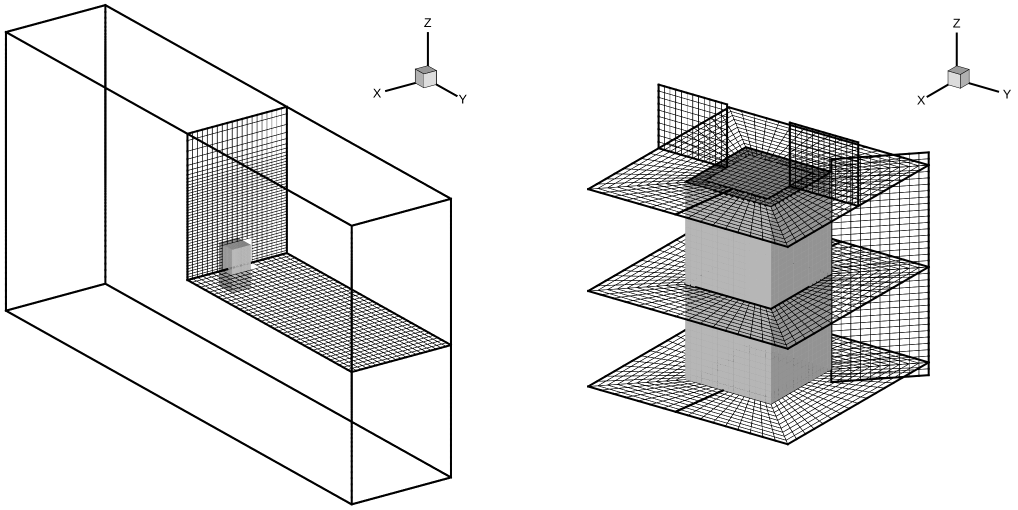

Figure 6.11. 3D grid for green water simulation

m, resulting in wave steepness $\epsilon = ka = \dfrac{2\pi a}{L} = 0.628$. This guarantees the incident wave breaking in front of the structure. The wave period is 0.8 sec and the corresponding non-dimensional period is about 2.5. Note that the characteristic length is 1m, and Froude number is 1. The characteristic time $T = \dfrac{L}{U} = \dfrac{L}{\sqrt{gL}} = \dfrac{1}{\sqrt{L}} \approx 0.32$. The non-dimensional time step is set to 0.01. An absorption condition (numerical damping beach) is imposed at the right side of tank to avoid wave reflections. This is implemented by a damping function as follows:

$$damp(y) = \left[\frac{1}{2}\left(1 - \cos\frac{\pi \cdot (y - s_1)}{s_2 - s_1}\right)\right]^3$$

Figure 6.4 shows snapshots of a time series of wave impingement on a three-dimensional rectangular structure. The series shows time steps from 600 to 975 for every 75 steps. Figure 6.4 also shows that the highly nonlinear incident wave evolves to break before it hits the structure. Surging breakers occur here instead of plunging breaks in two-dimensional simulations. The surge front impinges on the front face of platform and produces a strong upward splash. Some green water on the top is clearly shown in Figure 6.4(c) and (f). Near the platform edges, however, the incident wave is able to move around the platform with significantly less green water effect. After the front passes the structure, the wake flow is captured in Figure 6.4(d) and (e). An experimental investigation will be conducted in the near future at Texas A&M University to provide detailed velocity measurements for the same platform configuration. The simulation results will be compared to the experimental data to provide a detailed validation of the present numerical method for the simulation of green water effects on three-dimensional offshore structures.

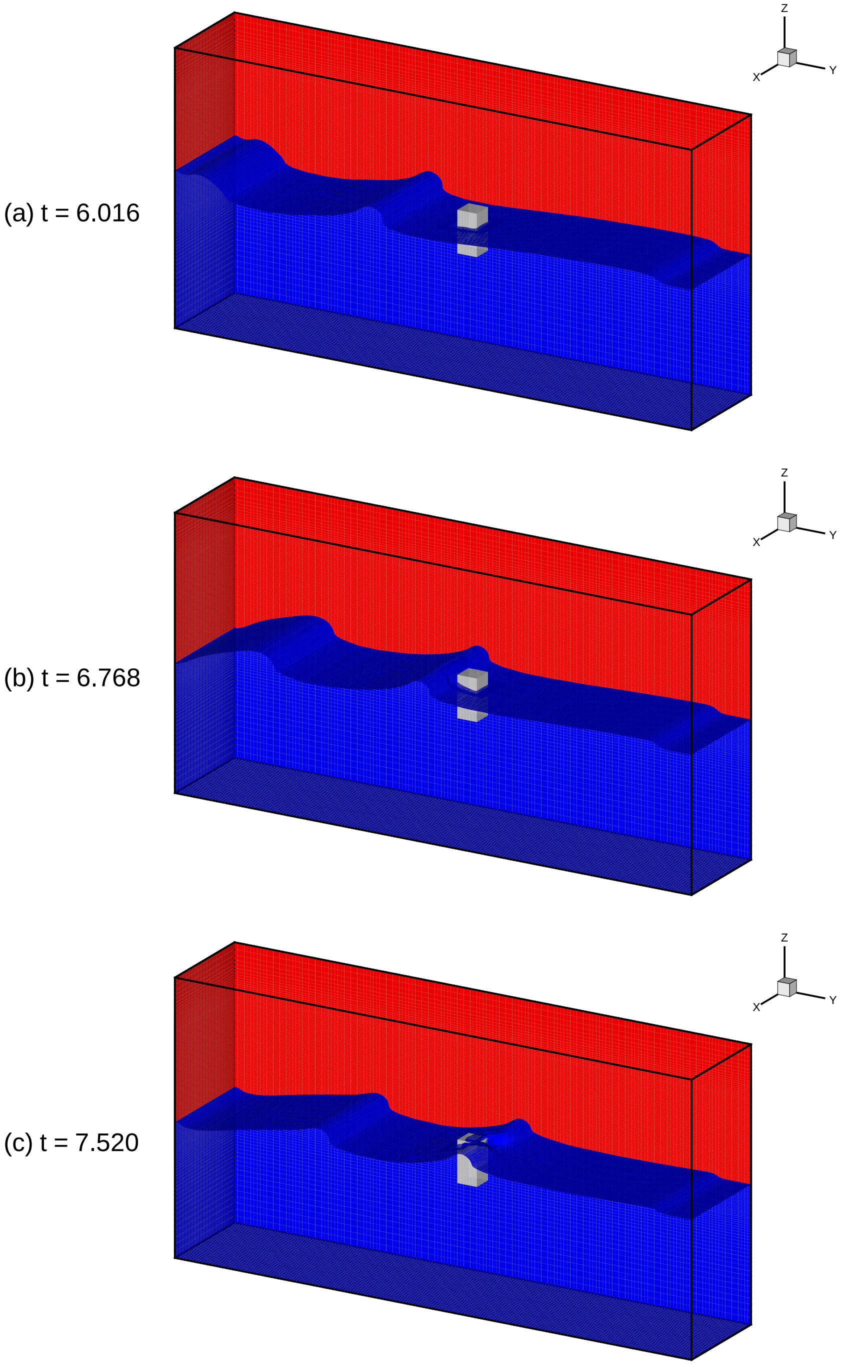

(a) t = 6.016

(b) t = 6.768

(c) t = 7.520

Figure 6.12. Green water on a 3D platform

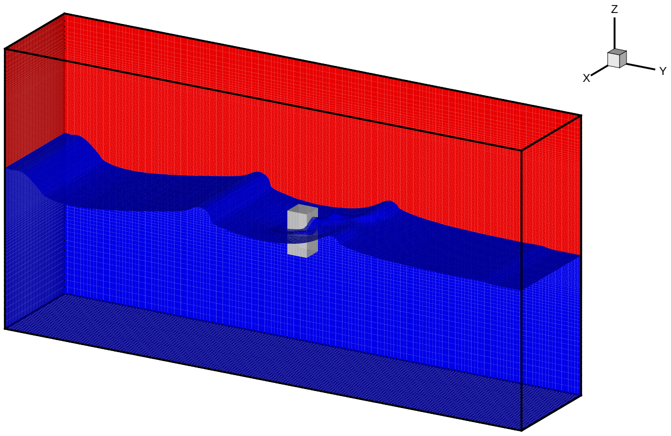

(d) t = 8.272

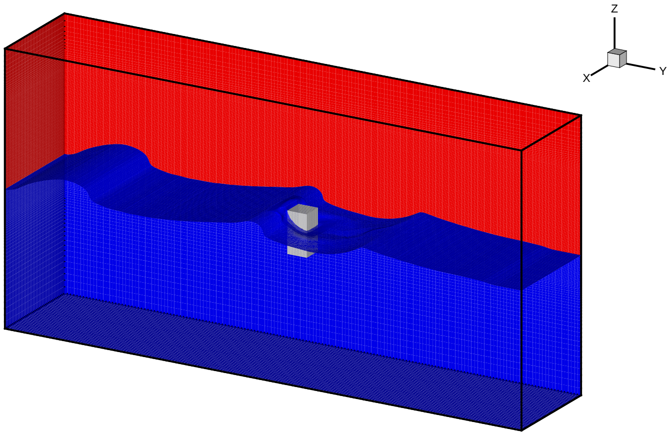

(e) t = 9.024

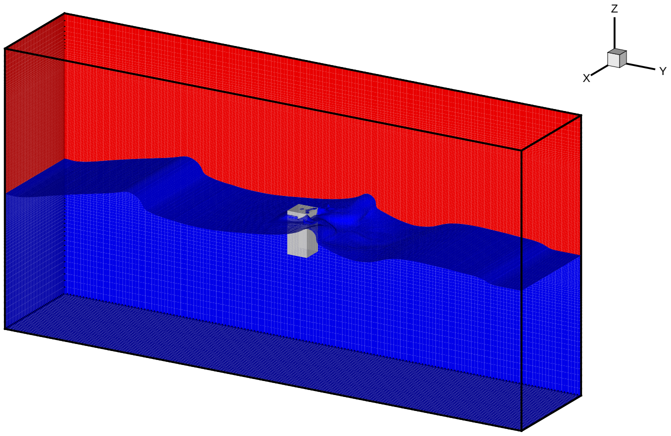

(f) t = 9.776

Figure 6.12. (Continued)

CHAPTER VII

CONCLUSIONS

7.1. Sloshing Simulations

In the present study, violent sloshing flows induced by the transverse and longitudinal motions of a membrane-type LNG tank were solved using the level-set Navier-Stokes method. The effects of turbulence were modeled using the Smagorinsky subgrid scale model in a Large Eddy Simulation (LES) approach. Both the water and air flows were solved simultaneously in the present two-phase flow approach to resolve the strong air-water interactions in the ullage space of the LNG tank. The predicted impact pressures for both the transverse and longitudinal motion cases are in reasonably good agreement with the corresponding experimental data although the peak pressures are somewhat underpredicted. For the 92.5% high filling level case, the free surface motion is less violent in the confined ullage space with lower impact pressures. Small negative pressures were observed for the 92.5% high filling case, which can be attributed to the air trapping and strong air-water interactions in the narrow ullage space. Three-dimensional instability of sloshing flow was observed for both the transverse and longitudinal motion cases and confirmed by the experiments even though the tank excitation forces are strictly two-dimensional.

7.2. Green Water over Offshore Structure

Time-domain simulations of wave runup and green water around offshore structures were performed using a Reynolds-Averaged Navier-Stokes (RANS) numerical method in conjunction with a chimera domain decomposition approach. The wave runup simulations were performed using the interface-tracking method, while the green water on offshore platforms were performed using the interface-capturing method based on level set formulation. The simulation results for wave runup on a two-dimensional TLP configuration are in close agreement with the corresponding PIV measurements. The interface-tracking method illustrates its capability for wave runup predictions including both the viscous and nonlinear wave effects.

In order to predict violent free surface flows, a Reynolds-Averaged Navier-Stoes (RANS) numerical method in conjuction with a level-set fuction is applied in time-domain simulations of green water around offshore structures. The new interface-capturing method is first employed to generate a plunging breaker in a single numerical wave tank. Then it is used for two-dimensional green water simulations on offshore platforms. The simulation results clearly demonstrate the flexibility and accuracy of the level set method for the prediction of complex free surface motions including wave breaking and green water effects.

REFERENCES

[1] Armenio, V., "An Improved MAC Method (SIMAC) for Unsteady High-reynolds Free Surface Flows," *International Journal for Numerical Methods in Fluids*, Vol.24, pp.185–214, 1997.

[2] Biausser, B., Fraunie, P., Grilli, S. and Marcer, R., "Numerical Analysis of the Internal Kinematics and Dynamics of Three-dimensional Breaking Waves on Slopes," *International Journal of Offshore and Polar Engineering*,Vol.14, No.4, 2004.

[3] Cariou, A. and Casella, G., "Liquid Sloshing in Ship Tanks: A Comparative Study of Numerical Simulation", *Marine Structures*,Vol.12, pp.183–198, 1999.

[4] Chan, R.K.C. and Street, R.L., "A Computer Study of Finite-Amplitude Water Waves," *Journal of Computational Physics*, Vol.6, pp.68–94, 1969.

[5] Chen, G., Karif, C., Zaleski, S. and Li, J., "Two-dimensional Navier-Stokes Simulation of Breaking Waves," *Physics of Fluids*, Vol.11, Number 1, pp. 121–133, 1999.

[6] Chen, H.C. and Chen, M., "Chimera RANS Simulation of A Berthing DDG-51 Ship in Translational and Rotational Motions," *Int. J. of Offshore and Polar Eng.*, Vol.8, No.3, pp. 182–191, 1998.

[7] Chen, H.C. and Huang, E.T., "Time-Domain Simulation of Floating Pier/Ship Interactions and Harbor Resonance," *in Proceedings of 14th International Offshore and Polar Engineering Conference*, Vol. III, pp. 772–779, 2004.

[8] Chen, H.C., Liu, T., Chang, K.A., and Huang, E.T., "Time-Domain Simulation of Barge Capsizing by A Chimera Domain Decomposition Approach," *in 12th International Offshore and PolarEngineering Conference*, Vol.III,pp. 494–501, 2002.

[9] Chen, H.C., Liu, T., and Huang, E.T., "Time-Domain Simulation of Large Amplitude Ship Roll Motions by A Chimera RANS Method," *in Proceedings, 11th International Offshore and Polar Engineering Conference*, Vol. III, pp. 299-306, 2001.

[10] Chen, H.C., Liu, T., Huang, E.T. and Davis, D.A., "Chimera RANS Simulation of Ship and Fender Coupling for Berthing Operations," *International Journal of Offshore and Polar Engineering*, Vol. 10, No. 2, pp. 112-122, 2000.

[11] Chen, H.C. and Patel, V.C., "The Flow around Wing-Body Junctions," *in Proceedings, 4th Symp. on Numerical & Physical Aspects of Aerodynamic Flows*, 1989.

[12] Chen, H.C. and Patel,V.C., "Near-Wall Turbulence Models for Complex Flows Including Separation," *AIAA Journal*, Vol.26, No. 6, pp.641–648, 1988.

[13] Chen, H.C., Patel, V.C. and Ju, S., "Solutions of Reynolds-averaged Navier-Stokes Equations for Three-Dimensional Incompressible Flows," *Journal of Computational Physics*, Vol. 88, pp. 305-335, 1990.

[14] Chen, H.C., Yu, Kai and Chen, S.Y., "Simulation of Wave Runup Around Offshore Structures by A Chimera Domain Decomposition Approach," *in Proceedings, Civil Engineering in the Oceans VI Conference*, October 20-22, 2004.

[15] Cokelet, E.D., "Steep Gravity Waves in Water of Arbitrary Uniform Depth," *Philosophical Transactions of Royal Society of London*, Vol, 286, pp. 183-230, 1977.

[16] Dean, R.G. and Dalrymple, R.A. (1994), "Water Wave Mechanics for Engineers and Scientists," World Scientific, Singapore, 1994.

[17] Dong, C.M. and Huang, C.J., "Vortex Generation in Water Waves Propagating Over A Submerged Rectangular Dike," *in Proceedings, 9th International Offshore and Polar Engineering Conference*, Vol. III, pp. 388-395, 1999.

[18] Duval, M., Astruc, D. and Legendre, D., "Two-phase Flow Modeling of Breaking Waves without Interface Reconstruction," *in Proceedings, 14th International Offshore and Polar Engineering Conference*, 2004.

[19] Enright, D., Fedkiw, R., Ferziger, J. and Mitchell, I., "A Hybrid Particle Level Set Method for Improved Interface Capturing," *Journal of Computaional Physics*, Vol.183, pp.83–116, 2002.

[20] Faltinsen, O.M., Rognebakke, O.F., Lukovski, I.A. and Timoka, A.N., "Multidimensional Modal Analysis of Nonlinear Sloshing in A Rectangular Tank with Finite Water Depth," *Journal of Fluid Mechanics*, Vol.407, pp.201–234, 2000.

[21] Ferziger, J.H. and Peric, M., "Computational Methods for Fluid Dynamics," 2nd Edition, Springer- Verlag, 1999.

[22] Frandsen, J.B., "Sloshing Motions in Excited Tanks," *Journal of Computational Physics*, Vol.196, pp.53–87, 2004.

[23] Gibou, F., Fedkiw, R. Caflisch, R. and Osher S., “A Level Set Approach for the Numerical Simulation of Dendritic Growth,” *Journal of Scientific Computing* Vol.19, pp.183–199, 2003.

[24] Harlow, F.H. and Welch, J.E., “Numerical Study of Large-Amplitude Free Surface Motions,” *Physics of Fluids*, Vol. 8, pp. 2182-2189, 1965.

[25] Hirt, C.W. and Hotchkiss, R.S., “SOLA-VOF: A Solution Algorithm for Transient Fluid Flow with Multiple Free Boundaries,” Technical Report LA-8355, Los Alamos National Laboratory, 1980.

[26] Hirt, C.W. and Nichols, B.D., “Volume of Fluid (VOF) Method for the Dynamics of Free Boundaries,” *Journal of Computational Physics*, Vol. 39, pp. 201-225, 1981.

[27] Huijsmans, R.H.M. and van Grosen, E., “Coupling Freak Wave Effects with Green Water Simulations,” *in Proceeding of the 14th ISOPE*, pp.366–373, 2004.

[28] Hwang, S.H., “Experimental and Numerical Investigation on Sloshing Impact Load,” *Ph.D. Dissertation*, Pusan Nation University, Korea, 2006.

[29] Iglesias, A.S., Rojas, L.P. and Rodriguez, R.Z., “Simulation of Anti-roll Tanks and Sloshing Type Problems with Smoothed Particle Hydrodynamics,” *Ocean Engineering*, Vol.31, pp.1169–1192, 2004.

[30] Kim, Y., “Numerical Simulation of Sloshing Flows with Impact Load,” *Applied Ocean Research*, Vol.23, pp.53–62, 2001.

[31] Kim, Y., “Numerical Study on Slosh-induced Impact Pressures on Three-dimensional Prismatic Tanks,” *Applied Ocean Research*, Vol.26, pp.213–216, 2004.

[32] Koshizuka, S., Tamako, H. and Oka, Y., "A Particle Method for Incompressible Viscous Flow with Fluid Fragmentation," *Computational Fluid Dynamics Journal*, Vol. 4, No. 1, pp. 29-46, 1995.

[33] Kothe, D.B. and Rider, W.J., "Comments on Modeling Interfacial Flows with Volume-of Fluid Methods," *Los Alamos National Laboratory Reports*, 1995.

[34] Lafaurie, B., Nardone, C., Scardovelli, R., Zalesaki, S. and Zanetti, G., "Modelling Merging and Fragmentation in Multiphase Flows with SURFER," *Journal of Computational Physics*, Vol.113, pp.134–147, 1994.

[35] Lee, D.H., Kim, M.H., Kwon, S.H., Kim, J.W. and Lee, Y.B., "A Parametric Sensitivity Study on LNG Tank Sloshing Loads by Numerical Simulations," *Ocean Engineering*,Vol.34, pp.3–9, 2007.

[36] Lee, Y.B., Lee, J.M., Kim, Y.S., Jung, J.H., Jung, D.W. and Kwon, S.H., "An Experimental Study of Impulsive Sloshing Load Acting on LNGC Tank," *in Proceedings of the 16th ISOPE*, 2006.

[37] Longuet-Higgins, M.S. and Cokelet, E.D., "The Deformation of Steep Surface Waves on Water. I. A Numerical Method for Computation," *Proceedings of the Royal Society of London*, Series A, Vol.350, No.1660, pp. 1–26, 1976.

[38] Loots, E., Pastoor, W., Buchner, B. and Tveitnes, T., "The Numerical Simulation of LNG Sloshing with An Improved Volume of Fluid Method," *in Proceedings, 23rd internaitonl conference on offshore mechanics and arctic engineering*, 2004.

[39] Mei, C.C., ""The Applied Dynamics of Ocean Surface Waves," World Scientific: Singapore. Nichols, B.D., 1989.

[40] Miyata, H., “Finite-Difference Simulation of Breaking Waves,” *Journal of Computational Physics*, Vol.65, pp.179–214, 1986.

[41] Nam, B.W. and Kim, Y., “Simulation of Two-Dimensional Sloshing Flows by SPH Method,” *in Proceedings of the 16th ISOPE*, pp.342–347, 2006.

[42] Osher, S. and Fedkiw, R., “Level Set Methods: An Overview and Some Recent Results,” *Journal of Computational Physics*, Vol.169, pp.463–502, 2001.

[43] Osher, S. and Fedkiw, R., “Level Set Methods and Dynamics Impicit Surfaces,” New York Springer-Verlag, 2003.

[44] Osher, S., and Sethian, J.A., “Fronts Propagating with Curvature-dependent Speed: Algorithms Based on Hamilton-Jacobi Formulations,” *Journal of Computational Physics*, Vol. 79, No. 1, pp. 12-49, 1988.

[45] Park, J.C., Uno, Y., Matsuo, H., Sato, T. and Miyata, H., “Reproduction of Fully-Nonlinear Multi-Directional Waves by a 3D Viscous Numerical Wave Tank,” *in Proceedings, 11th International Offshore and Polar Engineering Conference*, Vol. III, pp. 140-147, 2001.

[46] Pitsch, H. and Lageneste, L., “Large-eddy Simulation of Premixed Turbulent Combustion Using A Level-set Approach,” *Proceedings of the Combustion Institute*, Vol.29, pp.2001–2008, 2002.

[47] Rocca, M.L., Sciortino, G. and Boniforti, M.A., “A Fully Nonlinear Model for Sloshing in A Rotating Container,” *Fluid Dynamics Research*, Vol.27, pp.23–52, 2000.

[48] Scardovelli, R. and Zaleski, S., “Direct Numerical Simulation of Free-surface and Interfacial Flow,” *Annual Reviews of Fluid Mechanics*, Vol.31, pp.567–603, 1999.

[49] Sethian, J.A., "Level Set Methods," Cambridge Univ. Press, 1996.

[50] Sethian, J.A. and Adalsteinsson, D., "An Overview of Level Set Methods for Etching, Deposition, and Lithography Development," *IEEEE Transactions on Semiconductor Devices*, Vol.10, 167–184, 1996.

[51] Shu, C.W, "Essentially Non-Oscillatory and Weighted Essentially Non-Oscillatory Schemes for Hyperbolic Conservation Laws," ICASE Report No.97-65, NASA/CR-97-206253, 1997.

[52] Shu, C.W. and Osher, S., "Efficient Implementation of Essentially Nonoscillatory Shock Capturing Schemes II," *Journal of Computational Physics*, Vol. 83, pp. 32-78, 1989.

[53] Sussman, M., Smereka, P. and Osher, S., "A Level Set Approach for Computing Solutions to Incompressible Two-Phase Flow," *Journal of Computational Physics*, Vol. 114, pp. 146-159, 1994.

[54] Sussman, M. Fatemi, E., Smereka, P. and Osher, S., "An Improved Level Set Method for Imcompressible Two-phase Flows," *Computer & Fluids*, Vol. 27, pp. 663-680, 1998.

[55] Sussman, M. and Fatemi, E., "An Efficient, Interface-Preserving Level Set Redistancing Algorithm and Its Application to Interfacial Incompressible Fluid Flow," *SIAM J. of Scientific Comput.*, Vol. 20, pp. 1165-1191, 1999.

[56] Sussman, M. and Puckett, E.G., "A Coupled Level Set and Volume-of-fluid Method for Computing 3D and Axiymmetric Incompressible Two-phase Flows," *Journal of Computational Physics*, Vol.162, pp:301–337, 2000.

[57] Suhs, N.E. and Tramel, R.W., “PEGSUS 4.0 Users Manual,” Arnold Eng Dev Center Rep AEDC-TR-91-8, Arnold Air Force Station, TN, 1991.

[58] Takahira, H., Horiuchi, T. and Banerjee, S., “An Improved Three-Dimensional Level Set Method for Gas-Liquid Two-Phase Flows,” *Journal of Fluids Engineering*, Vol.126, pp.578–585, 2004.

[59] Wu, G.X., Ma, Q.W. and Taylor, R.E., “Numerical Simulation of Sloshing Waves in A 3D Tank Based on A Finite Element Method,” *Applied Ocean Research*, Vol.20, pp.337–355, 1998.

[60] Yang, Chi and Lohner, Rainald, “Computaion of 3D Flows with Violent Free Surface Motion,” *in Proceedings of the 15th ISOPE*, 2005.

[61] Valentine, D.T. and Frandsen, J.B., “Nonlinear Free-Sruface and Viscous-Internal Sloshing,” *Journal of Offshore Mechanics and Arctic Engineering*, Vol.127, pp. 141–149, 2005.

[62] Van der Pijl, S.P., Segal, A., Vuik, C. and Wesseling, P., “A Mass-conserving Level-Set Method for Modelling of Multi-phase Flows,” *International Journal for Numberical Methods in Fluids*, Vol.47, pp.339–361, 2005.

[63] Yue, W.S., Lin, C.L. and Patel, V.C., “Numerical Simulation of Unsteady Multidimensional Free Surface Motions by Level Set Method,” *Int. J. Numer. Meth. Fluids*, Vol. 42, pp. 853-884, 2003.

[64] Zalesak, S.T., “Fully Multidimensional Flux-Corrected Transport Algorithms for Fluids,” *Journal of Computational Physics*, Vol. 31, pp. 335-362, 1979.

VITA

Kai Yu was born in Quzhou, Zhejiang, China. He received his B.S. in Mechanical Engineering from University of Science and Technology of China in 1998 and his M.S. in Cryogenic Engineering from Shanghai Institute of Technical Physics, Chinese Academy of Sciences, in 2001. He entered the Ocean Engineering Program, Civil Engineering Department of Texas A&M University in September of 2003 and completed his Ph.D. in December of 2007.

He can be reached at: HydroLab 103, 3136 TAMU, College Station, TX 77843-3136, U.S.A.

The typist for this thesis was Kai Yu.